



Crystal Engineering in Nanoporous Matrices

Dissertation

zur Erlangung des akademischen Grades

doctor rerum naturalium

(Dr. rer. nat.)

genehmigt durch

Institut für Chemie neuer Materialien der Universität Osnabrück

vorgelegt von

Frau M. Sc. Gitte Graubner

Gutachter:

1. Prof. Dr. Martin Steinhart

2. Prof. Dr. Mario Beiner

Osnabrück, Oktober 2014

Was man nicht aufgibt, hat man nie verloren.

Friedrich Schiller

Abstract

The topic of this PhD thesis is the systematic investigation of crystallization parameters and their influence on nucleation and crystal growth of the two selected model compounds acetaminophen (ACE) and *n*-tetracosane inside porous hosts. The materials in the two model matrices AAO and CPG have been investigated with X-ray diffraction (WAXS) and DSC measurements. The pore morphology of the nanoporous matrices (interconnected-spongelike/aligned cylindrical) determines which ACE polymorphic form crystallizes and influences the kinetics of the solid/solid transition from form III to form II. Release of ACE having rough crystal faces oriented normal to the AAO pore axis is nearly as fast as release of amorphous ACE. Release kinetics can be reproduced with the Korsmeyer-Peppas model. *n*-Tetracosane under confinement shows a more complex phase behavior than the high-molecular weight analogue polyethylene. The presented work expands the available strategies for *mesoscopic crystal engineering*.

Kurzdarstellung des Inhalts

Thema dieser Dissertation ist die systematische Untersuchung von Kristallisationsparametern und deren Einfluss auf Keimbildung und Kristallwachstum in porösen Matrices von Acetaminophen (ACE) und *n*-Tetracosan. Die Materialien in den nanoporösen Wirtssystemen AAO und CPG wurden neben der Kalorimetrie (DSC) mit Streumethoden (WAXS) untersucht. So ist die Porenmorphologie der Wirtssysteme (kontinuierlich schwammartig/parallel zylindrisch) ein wichtiger Parameter der zum einen beeinflusst, welche polymorphe Form von ACE kristallisiert, zum anderen den Fest/Festphasenübergang von Form III zu Form II. Eine polymorph-spezifische Wirkstofffreisetzung von ACE aus AAO zeigt, dass die Freisetzung mit dem Korsmeyer-Peppas-Model beschrieben werden kann. Einkapselung von ACE in AAO verlangsamt die Wirkstofffreisetzung, beeinflusst aber nicht die Freisetzungskinetik. *n*-Tetracosan in nanoporösen Systemen besitzt ein weitaus komplexeres Kristallisationsverhalten als das vergleichbare Polymer Polyethylen. Die vorgeschlagenen Schritte zur Beeinflussung der Kristallisation werden in dieser Arbeit als *mesoscopic crystal engineering* zusammengefasst.

Contents

Motivation	i
1 State of the Art	1
1.1 Crystallization	1
1.1.1 Nucleation	1
1.1.2 Structural Description of Crystals	4
1.1.3 Crystal Growth and Growth Morphology	5
1.2 Polymorphism	9
1.3 Soft Material Confined to Nanoporous Matrices	11
2 Model Systems	14
2.1 Anodic Aluminum Oxide (AAO)	14
2.2 Controlled Porous Glasses (CPG)	16
2.3 Acetaminophen (ACE)	17
2.4 <i>n</i> -Alkanes: <i>n</i> -Tetracosane	19
3 Experimental Section	22
3.1 Sample Preparation	22
3.2 X-ray Diffraction	28
3.2.1 Principles	28
3.2.2 Set-up X-ray Diffractometer	32
3.2.3 Texture Analysis	34
3.2.4 Data Interpretation	35
3.3 Thermal Analysis	36
3.4 Scanning Electron Microscopy	40
3.5 Electron Paramagnetic Resonance	40
4 AAO Membrane Characterization	41
4.1 Influence of Thermal and Water Treatment on AAO Membranes	41
4.2 Influence of AAO Preparation on EPR signals	42
5 Acetaminophen Confined to Nanoporous Matrices	46
5.1 Influence of Crystallization Parameter on ACE in AAO Membranes	46
5.1.1 ACE in 60 nm AAO Quenched in the Presence of Bulk Material	47
5.1.2 ACE in 60 nm AAO Cooled at 0.5 K/min in the Presence of Bulk Material	49

5.1.3	Amorphous ACE in 60 nm AAO Membranes	53
5.2	Isothermal Crystallization of ACE in AAO 60 nm	54
5.3	ACE in Controlled Porous Glasses (CPG)	57
5.4	ACE in AAO with Pore Sizes Ranging from 25 to 400 nm	59
5.4.1	Non-Isothermal Crystallization	60
5.4.2	Cold Crystallization (Isothermal Crystallization)	64
5.5	Discussion of Acetaminophen in 2D-Confinement	68
5.5.1	Crystallite Orientation and Crystal Growth Kinetics in AAO Membranes	69
5.5.2	Influence of Pore Sizes and Volume on Crystallization in AAO Membranes	73
5.5.3	Influence of Pore Morphology on Crystallization in Nanoporous Matrices	75
6	Release Kinetics of Acetaminophen from AAO Membranes	77
6.1	Controlled Drug Release from 60 nm AAO Membranes	77
6.2	Controlled Drug Release from AAO with Pore Sizes Ranging from 25 to 400 nm	80
6.3	Kinetic Modeling of the Drug Release	82
6.4	Encapsulation of Acetaminophen in AAO Membrane using Polymer Films	84
6.5	Discussion	88
7	<i>n</i> -Tetracosane Confined to Nanoporous Matrices	92
7.1	Crystallization of Bulk <i>n</i> -Tetracosane	92
7.2	<i>n</i> -Tetracosane in AAO Cooled at 0.5 K/min in the Presence of Bulk Material	96
7.3	Lamellar Crystals of <i>n</i> -Tetracosane in AAO Membranes	102
7.4	<i>n</i> -Tetracosane in AAO Cooled at 0.5 K/min in Absence of Bulk Material	104
7.5	<i>n</i> -Tetracosane in CPG Cooled at 0.5 K/min	109
7.6	Thermal Analysis of <i>n</i> -Tetracosane in Nanoporous Matrices	112
7.7	Aging Behavior of <i>n</i> -Tetracosane in AAO Membranes	115
7.8	Discussion of <i>n</i> -Tetracosane in 2D-Confinement	117
7.8.1	Crystallite Orientation of Triclinic <i>n</i> -Tetracosane in AAO Membranes	117
7.8.2	Influence of Pore Size, Bulk Surface Material, and Pore Wall Modification	119
7.8.3	Lamellar Crystals	123
7.8.4	Rotator Phases of <i>n</i> -Tetracosane in AAO Membranes	126
7.8.5	Summary	128
8	Conclusions and Outlook	130
9	Bibliography	135
10	List of Figures and Tables	144

11 Abbreviations and Symbols	151
11.1 Abbreviations	151
11.2 Symbols	154
Acknowledgements / Danksagung	155
Appendix A	157
Appendix B.....	158

Motivation

During the last decade, crystallization behavior of confined material has attracted many researchers. Investigations reveal that characteristic properties of a substance, such as melting points, enthalpies of fusion¹, or crystal orientation are affected by nanoporous matrices. Moreover, the confinement has influence on polymorphic drug crystallization² which has a significant importance for possible solid/solid phase transitions. Additionally, the confinement has influence on polymorph dissolution, release kinetics, and bioavailability³. These properties are linked to the increase of the surface-to-volume ratio due to the decrease of pore size and hence, the resulting crystal size. Thermotropic properties which are influenced by the size of the material can be equated with the critical size concept described by the classical nucleation theory. This theory establishes a nucleation barrier. As a result, the critical size must have a size at which the unfavorable surface free energy is compensated by the volume free energy before crystal growth occurs. In general, nucleation and crystal growth are kinetic processes. On the other hand, the properties of confined materials are a consequence of their thermodynamics.⁴

For investigation of nanosized material two host-systems are mostly used: anodic aluminum oxide (AAO)⁵ with isolated, cylindrical (anisotropic) pores, and controlled porous glasses (CPG) with interconnected, curved (isotropic) pores.⁶ Systematic studies of polymorphic material in CPG matrices reveal that the stability of polymorphs depends on the crystals size, which is consistent with Ostwald's rule of stages.⁷ Additionally, isotropic nanopores can be used as matrices in order to gain knowledge about the early stages of crystallization⁷⁻⁹, or about the basic building principles of condensed matter¹⁰. Matrices with anisotropic pores provide good opportunity to investigate crystal orientation within the pores. For example, different kinds of materials¹¹⁻¹⁴ in isolated nanopores show a dominant growth direction parallel to the pore axis. Furthermore, unique features such as low cost fabrication, controllable pore structures, tailored surface chemistry, high surface area, chemical resistivity, mechanical rigidity and pore walls, which can be modified chemically allows crystal

growth manipulation, or control over crystal orientation. As a consequence, crystallization in nanoporous matrices provides new routes to functional materials such as ferroelectric polymers¹⁵, or liquid crystal-based devices with tunable optical, thermal, and dielectric properties.^{16, 17} Investigations on confined material also have an impact on food, pharmaceutical, explosive or dye industries.² The use of nanopores matrices for drug delivery applications¹⁸ is also important. Encapsulated drugs offer several advantages; e.g., protection from degradation, drug release only under specific conditions¹⁹, extended drug release time, or increased bioavailability of the drug²⁰. Nanoporous membranes with tailored properties can be used directly or can be placed in an implant device²⁰. In this PhD study comes together the ability to control polymorphism, the particle size and the crystal orientation with the use of the matrices as drug delivery carriers. Sufficient information about the crystallization conditions and their influence on phase behavior, crystal texture, and stability of polymorphs should be retrieved prior to drug delivery experiments. In previous studies, nanosized materials have been used for investigations of crystal orientations or thermotropic properties. However, little work has been done on the systematic study of the influence of crystallization parameters on crystallization kinetics. What are those crystallization parameters? Crystallization conditions are not only different pore morphologies (i.e., interconnected/isolated) but also parameters such as:

- ◆ pore sizes of matrices; ranging from 2 nm to 400 nm
- ◆ pore wall chemistry; hydrophilic or hydrophobic
- ◆ thermal history; isothermal, non-isothermal (cooling rates)
- ◆ bulk surface reservoir; present or absent

Crystallization conditions can be used as a basic for specific polymorph formation or to study crystallization of more complex materials. In this investigation, two model compounds have been selected.

- ◆ Acetaminophen, a low-molecular weight polymorphic drug, was chosen for investigation of crystallization kinetics and polymorphic transitions in interconnected and isolated nanopores.

- ◆ *n*-Tetracosane an *n*-alkane family member, which exhibits a series of rotator phase transitions between crystal and liquid phase. Further, *n*-alkanes form lamellar crystals. Such crystals can have anisotropic physical properties. *n*-Tetracosane may be used as model compound for the more complex crystallization behavior of polymer materials under confinement.

There is still an open question about the influence of crystallization parameters (e.g., cooling rates, in contact to bulk surface material, pore morphology) on crystallization kinetics of material in anisotropic AAO membranes. Therefore, acetaminophen is confined to AAO under variation of the crystallization parameters. The achieved results will be compared with acetaminophen in CPG membranes solidified under identical crystallization conditions and with already reported crystallization results^{7, 21, 22}. A nucleation and crystal growth model will be presented. Based on the results from part one acetaminophen is encapsulated in anodic aluminum oxide and controlled drug release experiments will be performed. Such experiments will reveal a relationship between acetaminophen modifications and their dissolution rates from AAO membranes. Additional studies with *n*-tetracosane will be done. The orientation of lamellar crystals is also an open question as well as the behavior of rotator phases under confinement.

Collectively, the study of the two compounds confined to nanoporous matrices will provide a systematic description of crystal orientation and crystal growth kinetics. In fact, the results desired from this research have an impact on the mesoscopic design of drug delivery systems, on nanowire-based organic electronics, or on the development of new types of phase change materials. In general, crystal engineering in nanoporous matrices combines two different branches of the knowledge of crystallography and chemistry. The combination of both is therefore the interplay between the structure and properties of molecules and the resulting crystals.²³

1 State of the Art

1.1 Crystallization

In general, the driving force of crystallization is to lower the Gibbs free energy of a given system. But, even today, the crystallization steps shown in Figure 1.1 are difficult to understand.

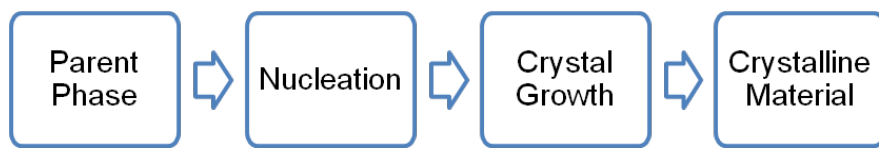


Figure 1.1: The crystallization pathway.

Nucleation and crystal growth are controlled by thermodynamic and kinetic factors. The thermodynamics dictate the lowest energy state and the kinetics gives the rate at which this is achieved.²⁴ But before a system can nucleate and grow it must overcome an energy barrier. Once a stable nucleus is formed, other molecules can flow and attach on its surface and the nucleus can grow into a crystal.

1.1.1 Nucleation

The nucleation or formation of a stable seed is the most critical step during the whole crystallization process. Nucleation can be divided into two main processes: primary and secondary. In the first one, no crystals are initially present in the solution. In the second one, nucleation occurs if seed crystals are present. The primary nucleation is further divided into two classes: homogeneous and heterogeneous (Figure 1.2). Homogeneous nucleation occurs spontaneously in bulk solutions and in the absence of impurities. On the other hand, heterogeneous nucleation takes place at interfaces, surfaces, or in the presence of impurities.²⁵⁻²⁷

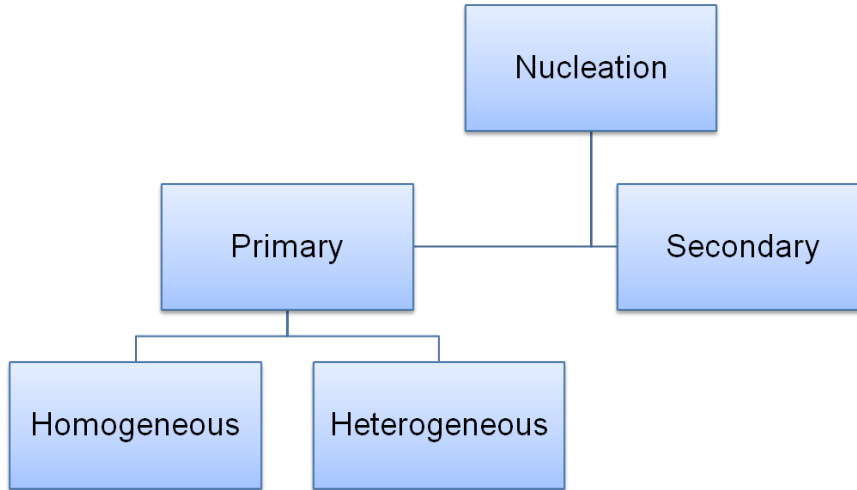


Figure 1.2: Chart showing nucleation steps.

Homogenous nucleation was first described in the work of *J. W. Gibbs*.²⁸ Later, the theory was developed into a classical nucleation theory (CNT). The driving force of nucleation is to minimize the total Gibbs free energy $\Delta G_{T(otal)}$ of a system. ΔG_T is described as the sum of the volume free energy term $\Delta G_{V(olume)}$ and the surface free energy term $\Delta G_{S(urface)}$. The volume term favors aggregation of many seeds whereas the surface term favors the dissolution of the nuclei. In the next step it is assumed that the nuclei or cluster are spherical with radius r . Further, a formed cluster must overcome a critical size r^* , then it is termed as nucleus which grows into a crystal. Small clusters with the radius below the critical size cannot overcome the increase of the surface energy when a next building unit attaches to it. Therefore, the surface term dominates and the cluster will dissolve. If the radii of the clusters are larger than r^* , the internal energy can exceed the increase of the surface energy and the seeds are able to grow. The total free energy can be expressed as:

$$\Delta G_T = A\gamma + V\Delta G_v \quad 1.1$$

where A is the surface area, γ is the interfacial tension between the nuclei and the surrounding solution, V is the volume, and ΔG_v is the free energy change per unit volume of the system. When the formed nucleus has a spherical geometry equation 1.1 can be written as:

$$\Delta G_T = \underbrace{4\pi r^2 \gamma}_{\text{surface term}} + \underbrace{\frac{4}{3}\pi r^3 \Delta G_v}_{\text{volume term}} \quad 1.2$$

Both terms are of opposite sign and depend differently on the size of the nucleus r . Furthermore, when the free energy G is plotted versus the nucleus size r the total free energy G_T reaches a maximum. At the maximum, the radius of the critical cluster size r^* can be calculated by differentiating ΔG and setting $\frac{d\Delta G}{dr} = 0$:

$$r^* = -\frac{2\gamma}{\Delta G_v} \quad 1.3$$

Substituting equation 1.2 into 1.3 gives for the critical energy ΔG^* :²⁷

$$\Delta G^* = \frac{16\pi\gamma^3}{3(\Delta G_v)^2} \quad 1.4$$

This energy needs a system to overcome the nucleation barrier which corresponds to the activation free energy of nucleation. For free energy change per volume can be written:

$$\Delta G_v = \Delta H_v - T_c \Delta S_v \quad 1.5$$

where ΔH_v and ΔS_v are the volume enthalpy and entropy of crystallization, respectively, and T_c is the equilibrium temperature.

The nucleation rate J can be expressed through an Arrhenius temperature dependence. The rate gives the number of nuclei formed per time and volume unit:

$$J = A \exp\left(-\frac{\Delta G^*}{k_B T}\right) \quad 1.6$$

where A is the pre-exponential factor and k_B is the Boltzmann constant. Combining equation 1.4 and the equation for the nucleation rate, the following expression is obtained:

$$J = A \exp\left(-\frac{16\pi\gamma^3}{3k_B T (\Delta G_v)^2}\right) \quad 1.7$$

The equation for the homogenous nucleation rate expresses the complexity of the nucleation process.²⁶ Different factors such as temperature, surface tension or the degree of supersaturation may influence the nucleation rate.

As previously mentioned, heterogeneous nucleation occurs in the presence of impurities, dust, nucleation agents, or other crystals. It is easier to form a stable nucleus in presence of surfaces with solid heterogeneities. Contacts to other surfaces reduce the overall surface energies of the seeds and hence, the critical radii. As a result, heterogeneous nucleation is easier to achieve and starts at lower supercooling than other nucleation mechanisms. Heterogeneous nucleation can occur, for example, in cavities under conditions in which the nucleus is normally unstable on a flat surface. In general, the diameter of the cylindrical cavity determines which seeds can act as nuclei.^{27, 29}

The term secondary nucleation is used when nucleation is induced by crystals. It is known that a supersaturated solution nucleates easier when crystals are present or added (i.e., crystal seeding).²⁷

1.1.2 Structural Description of Crystals

After nucleation, the nuclei grow into crystals. For a better understanding it is important to describe well the regular arrangement or symmetry of the atoms or molecules in the crystal and to use the right termini. The description starts with the smallest or minimal building units of a crystal which can be atoms, ions or molecules. Each of the unit contains the same structural features and symmetry elements and can be translated in three dimensions. The minimal block is called the unit cell of the crystal structure and contains at least one molecule. When the unit cell is translated in the three-dimensional space, a point lattice is formed. The size and shape of the unit cell can be defined with three vectors a , b and c . The three vectors are the crystallographic axes of the unit cell and have the same starting point. A vector is characterized by length and direction. Further, a unit cell can be described with six parameters; where a , b and c are the length of the three vectors, and α , β and γ are the angles between the vectors. The relationship among the six parameters results in various crystal systems. Seven crystal systems are

enough to describe all the possibilities of the 14 point lattices termed *Bravais* lattices.³⁰
³¹ There are 32 possible combinations referred to as point groups. In summary the 32 point groups with the 14 *Bravais* lattices give 230 unique arrangements of points in space, called *space groups*.

Other important concepts to keep in mind are lattice directions and crystal planes. The lattice direction is described by three integers $[uvw]$. In a crystal, all symmetry equivalent directions to $[uvw]$ are represented by the notation $\langle uvw \rangle$. The orientation of a lattice plane can be described in a similar way with three integers referred to as *Miller indices* (hkl) . These indices are the reciprocal intercepts of the plane with the unit cell axis. The notation (hkl) denotes a single plane. The symbol $\{hkl\}$ specifies a set of planes that are symmetry equivalent to (hkl) . When a lattice plane is parallel to one of the main axis, the intercept is ∞ and the Miller index is zero. For example, the (200) lattice plane is oriented parallel to axes b and c and intercepts axis a at half-length. The spacing between adjacent planes is described as lattice, interplanar or d -spacing d_{hkl} . More details can be found in references 30, 32, 33.

1.1.3 Crystal Growth and Growth Morphology

As previously mentioned, crystal growth starts when stable nuclei are larger than the critical size. However, after nucleation, some questions arise: how to attach a building block to a crystal surface, and then how does the crystal grow? In recent years different crystal growth theories have been developed in order to solve these questions. At first *J.W. Gibbs* suggested that the total free energy of a crystal in equilibrium would be a minimum for a given volume at constant pressure and temperature. Therefore, during growing, the crystal will reach a minimum of the total free surface energy. Assuming that the volume free energy per unit volume is constant throughout the crystal then:

$$\sum_i^n a_i \cdot G_i = \min \quad 1.8$$

where a_i is the area of the i^{th} face of a crystal bounded by n faces, and G_i is the surface free energy per unit area of the i^{th} face.²⁷

Later the Gibbs-Volmer theory based on thermodynamics explained that, when growth units attach on the crystal face, they are not immediately bound to it. They lose one degree of freedom but they can still move along the crystal face. This theory suggests that the units will change into a position where attractive forces are the highest. The Kossel model developed the Gibbs-Volmer theory and showed that growing crystal faces have flat surfaces, steps, kinks, or edge vacancies.²⁷ In fact, at $T = 0^\circ\text{C}$ all atoms are at the same energy level and hence, all crystal faces are energetically equal. At higher temperatures unit blocks can interchange to energetically more favorable sites, leaving behind vacancies or unsaturated lateral bonds with a higher energy level. When a building block attaches at those sites, some energy is released and the crystal face surface energy is reduced. Such sites are classified as kinked sites (K). On a kink site a molecule is bound by three sites. But on a step site (S), molecules are only bound by two sites, and they can move to find a lower energy kink site. In general, the crystal growth process involves several steps.^{26, 34} A good model to describe crystal growth is the picture of a crystal surface as a large terrace with ledges. The ledges are defined by a crystallographic direction along the crossing of the terrace and a specific step plane. Kink sites are built when a growth unit attaches to the ledge and forms a third crystallographic plane³⁴ (Figure 1.3).

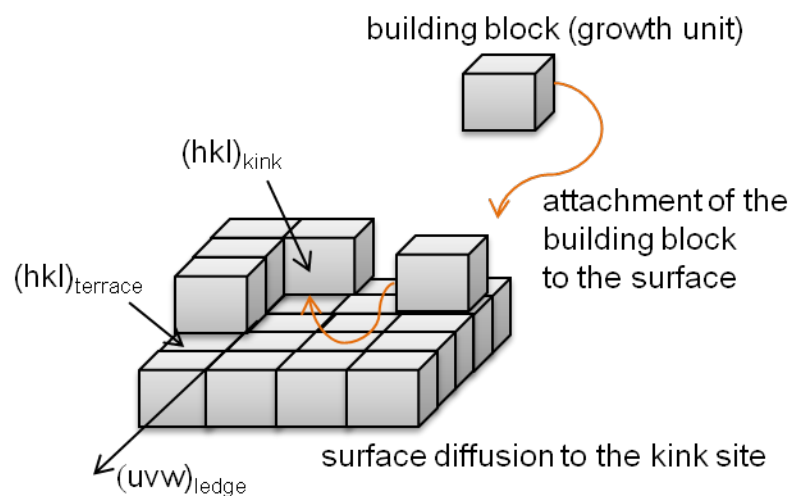


Figure 1.3: Schematic representation of the crystal growth via kink sites.

Growth entities from the bulk diffuse to the crystal surface and attach to the specific surface. The absorbed unit can either stay there or change to a more suitable low-energy site²⁶. On the atomic scale crystal faces can be smoother or rougher which has a significant influence on the crystal growth process. Rough surfaces have isotropic properties. On the other hand, smooth surfaces have anisotropic properties and form microscopic or macroscopic facets. The transition between the two modes is called surface-roughening transition and can be studied with the Ising model. Surface roughness or α -factor is an intrinsic property of the surface at equilibrium. The α -factor can be estimated and depends on the nature of the two phases separated by the interface and on the atomic structure of the surface.³⁵

In general, a crystal face grows by any process that provides the fastest growth rates. Step and kink faces grow through a rough growing, flat sites (F) via a layered growth mechanism.³⁶ Rough growth occurs at high supersaturation and with high growth rates. On K faces molecules incorporate into the crystal independently of their position on the crystal face. As a result of high growth rates, rough faces are short-living and grow into edges or vertices. On the other hand, layered growth takes place below the surface-roughening transition. On F faces, kink sites were only found along edges. Layered growth is a growing process slower than rough growth. Growth units grow layer-by-layer in a perpendicular direction to the crystal face.³⁶

The reduction of the surface free energy is the driving force for crystal growth. The evolution of the morphology is driven by a reduction in energy due to the minimization of the area of high surface energy resulting in faceted crystallites. Some crystal faces grow fast and have little or no effect on the growth shape. The crystal morphology is governed by the slow-growing faces.²⁷ The growth of each face is influenced by the density of growth sites, the defects and the environmental conditions. As mentioned before, the density of growing sites depends on the roughness of the crystal face. For further details regarding crystal growth models, see references 27, 36.

The knowledge of the growing rates and the resulting crystal structure is important for the pharmaceutical industry. Hence, prediction of the morphology generates remarkable interest. For this purpose different methodologies can be used. The basic model of prediction brings together the growth rate of a crystal face with the d -spacing d_{hkl} and is

called the Bravais, Friedel, Donnay and Harker law (BFDH). The law linked the thickness of a growth layer d_{hkl} to the chemical bond formation and therefore, to the growing rate. This assumption is only valid when the bonds are isotropic. In more complex organic crystals, van der Waals interactions or hydrogen bonding must be taken into account. Hartman and Perdok^{37, 38} developed a more sophisticated concept about growth units and bonds in addition to the crystal geometry which used only in the BFDH model. They considered the attachment energy instead of the surface energy. The attachment energy is defined as the bond energy released when a growth unit is attached to the surface of a crystal face.³⁹ This theory assumes that intermolecular forces determine the crystal morphology. Additionally, the existence of uninterrupted chains of molecules bonded with crystal faces is identified and the theory is called the periodic bond chain (PBC). Nowadays the Hartman-Perdok theory is known as the crystal graph. The crystal graph is a mathematical representation of the crystal structure as an infinite set of translationally vertices and edges.⁴⁰ With the PBC theory the crystal growth process is explained as a formation of uninterrupted bonds between growth units during crystallization. A crystal network is built with different PBCs which have different energies (weak or strong). The shapes of the crystals are determined by the weakest bond; therefore, important zone directions are parallel to PBCs and contain only strong bonds. Furthermore, two PBCs in different directions $[uvw]$ which span the d -spacing d_{hkl} create a connected net with the crystallographic orientation (hkl) ⁴⁰.

The crystal graph or PBCs theory divides the crystal faces also into three classes: K, F, or S faces. The F faces contain a connected net perpendicular to the reciprocal space vector H_{hkl} . Note the vector H_{hkl} is perpendicular to the corresponding crystal face (see Ch. 3.2.1). S faces have non-connected PBCs, and K faces have no PBCs perpendicular to H_{hkl} .⁴⁰ This theory is consistent with the idea that the energy of the crystal faces have influence on the growth direction and with the idea that the time needed for bond formation decreases as the bond energy increases. Consequently, perpendicular growth rates of a crystal face increase when the attachment energies increase. This gives the relationship between attachment energies E and the Gibbs free energies G , where i and j are indices for different faces:

$$E_i^{att} > E_j^{att} \Rightarrow G_i > G_j \quad 1.9$$

The attachment energy E^{att} can be determined as follows

$$E^{latt} = E_{hkl}^{slice} + E_{hkl}^{att} \quad 1.10$$

where E^{latt} is the total energy of intermolecular interactions per mole in a crystal. The slice energy E^{slice} is the energy released during formation of a growth layer of thickness d_{hkl} .^{26, 36} Relative growth rates of faces (hkl) are proportional to E_{hkl}^{att} which means that, knowing the attachment energies of all (hkl) faces, it is possible to predict the growth morphology.⁴⁰

1.2 Polymorphism

Controlling polymorphism is an important factor in crystal engineering. Polymorphism influences the solid state properties which depend on crystal structures, and it is common in the pharmaceutical sector, for instance in active pharmaceutical ingredients (APIs).⁴¹ Polymorphic materials are organic or inorganic compounds and have more than one crystal form. The crystal forms can differ in their physical and/or chemical properties. A very good example is the polymorphism of carbon i.e., the hexagonal graphite and the cubic diamond form. Graphite is the thermodynamically stable form at room temperature, but the high activation barrier makes the transition rate from diamond to graphite very slow.⁴² This is a well-known example showing that thermodynamic and kinetic factors influence the stability of polymorphs. The solid/solid transition occurs on a very slow time scale.

Polymorphic materials are classified into three types: conformational, packing, and pseudo polymorphism. Conformational polymorphism describes the existence of different conformers of the same molecules in different polymorphic forms. Packing polymorphism regards how flexible molecules can fold into different three-dimensional structures (i.e., unit cells). The crystal packing influences the crystal energy termed as the lattice energy. The lattice energy is influenced by non-covalent interactions, such as hydrogen bonds, van der Waals forces, π - π stacking or ionic and electrostatic

interactions. Hydrogen bonds and van der Waals forces (both attractive interactions) are the major intermolecular forces in pharmaceuticals^{25, 43}. The term pseudo polymorph is used for a new structure, either hydrated or solvated.

The thermodynamic theory includes that crystallization is a process where the Gibbs free energy of a system is reduced. Polymorphs can crystallize in structures with similar lattice energy. The stability of polymorphs under the given conditions depends on its free energies. The structure with the lowest energy is more stable for a given system. For this reason energy-temperature phase diagrams are used in this context. These diagrams show the relationship between the stability of polymorph forms versus the thermodynamic variables. Further details can be found in the basic study of *Burger et al.*⁴⁴. Transitions from one polymorphic form to another can be classified as enantiotropic or monotropic depending on whether one form can transform reversibly to another or not. Enantiotropism occurs if there is a transition point e.g., two polymorphic forms below their melting points and both forms undergo a reversible solid/solid transition. Monotropism occurs if one of the polymorphs is always stable below the melting points of both polymorphs.³

As previously described, the most stable polymorph will have the lowest free energy for a given system expressed as Gibbs free energy G :

$$\left(\frac{\partial}{\partial T} \frac{\Delta G}{T} \right)_p = - \frac{\Delta H}{T^2} \quad 1.11$$

where H is the enthalpy, S is the entropy, T is the temperature and p stands for pressure. The equation 1.11 is useful for example when a system is changing the physical state at constant pressure. It shows that, if the change in enthalpy of a system is known, then it is also possible to know the change in the Gibbs free energy with temperature.³³

1.3 Soft Material Confined to Nanoporous Matrices

The idea to use acetaminophen as a model compound for investigation of material under confinement has been based on the research done by *Rangarajan et al.*^{7, 21, 22} and *Beiner et al.*⁹. In those works, acetaminophen is embedded in CPG membranes and research conducted with differential scanning calorimetry (DSC) and X-ray diffraction. Acetaminophen, a polymorphic drug, exhibits melting point depression in CPG consistent with the Gibbs-Thompson equation.⁹ Furthermore, all acetaminophen forms (see Ch. 2.3) are achieved in CPG matrices. The commercial form I is obtained by rapid cooling of the melt in the presence of a bulk surface film. Form III, unstable in bulk material, is obtained in pores smaller than ~100 nm by isothermal crystallization without a bulk surface reservoir. The metastable form II cannot be achieved in pores smaller than 100 nm except by transformation of form III crystals via thermal cycling procedures. In small CPG (4.6 nm pore diameter) crystallization can be suppressed in favor of the amorphous phase.²¹ Systematic studies show that the transition between the polymorphs in CPG depends on the crystal size. A thermodynamic model of polymorph behavior under confinement is presented.

Researchers focused on anthranilic acid⁴⁵ in CPG membranes ranging from 7.5 nm to 55 nm find similar results. The preference for the metastable form in smaller pore sizes is explained with a smaller critical nucleus size as compared to the other thermodynamic stable polymorphic forms. The same is reported when ROY⁴⁵ is crystallized in cylindrical pores of nanoporous polymer monoliths. Additionally to the selective polymorph formation the material shows pronounced oriented crystallization in the polymer monoliths.

Crystallization studies of organic compounds^{46, 47, 8} in CPG membranes or porous diblock copolymer monoliths reveal a melting point decreasing with decreasing pore sizes, consistent with the increasing surface-to-volume ratio of the crystals.

Apart from the investigation of thermotropic properties, the uniaxial crystal growth in straight cylindrical pores has also attracted many researchers in the last few years. Mostly polymorphic organic and polymeric materials display highly oriented crystal

growth. For example, linear polyethylene in straight alumina nanopores¹³, or linear 1-alcohols⁴⁸ in mesoporous silicon show, that the molecular long axes are oriented normal to the pore axis. The material tends to grow with their fast-growth direction(s) parallel to the nanopores axis.

Cylindrical alumina nanopores have been used for investigation of the ferroelectric properties of PVDF-TrFE¹⁵. After crystallization, highly oriented crystals in the high temperature paraelectric phase are observed; the subsequent transition to the ferroelectric phases goes along with the loss of orientation. Isotactic poly(propylene)⁴⁹ in alumina nanopores reveals a transition from heterogeneous to homogeneous nucleation in dependence to pore size decrease. Crystallization is suppressed in pores below 20 nm.

Rodlike liquid crystals¹⁷ in anodic aluminum oxide membranes (AAO) show phase transition suppression. The nematic-to-isotropic and the crystal-to-nematic transition temperatures reduce linearly with the inverse of the pore diameter. The crystalline phase is suppressed in smaller pores which gives access to the critical nucleus size. Discotic liquid crystals¹⁶ in AAO membranes show a uniform alignment of the columnar axis. An optimal stacking of the aromatic cores allows the charge carrier mobility along such columnar axis. For applications as active semiconductors knowledge about the exact phase form and about the uniform columnar arrangement is essential. This is why the study of the material orientation in nanoporous matrices is so relevant.

Linear hydrocarbons named *n*-alkanes⁵⁰ in mesoporous silicon with straight aligned pores form lamellar crystals. In the lamellar structure the molecular long axes of the *n*-alkanes are oriented normal to the pore axis. *n*-Alkanes⁵¹ are also infiltrated in matrices with changed pore chemistry. Polytetrafluoroethylene (PTFE) has hydrophobic interconnected nanopores; in contrast Anopore has separated hydrophilic pores. For example, the phase transitions $R_{II} \rightarrow R_I$ and $R_I \rightarrow R_V$ of *n*-tetracosane change to a second order mechanism in such pores. Crystallization behavior of hentetracontane⁵² in nanoporous alumina membranes with different surface energies has also been investigated. This study reports that the crystallization and the crystal orientation are influenced by the degree of confinement and the nature of the membrane surface. *n*-Alkanes in porous SBA-15 and in CPG membranes show differences in phase behavior

and an influence of the CPG pore size of the molecule arrangement.⁵³ Recently, a published article⁵⁴ summarizes the crystallization features of *n*-alkanes under confinement. The authors underline that the studies of *n*-alkanes can help to understand the more complex work with polymers.

2 Model Systems

2.1 Anodic Aluminum Oxide (AAO)

Anodic aluminum oxide (AAO) is widely used as an inorganic model matrix. The matrix contains isolated, straight cylindrical nanopores. The nanopores are uniform in length and have a narrow size distribution. Such highly ordered aluminum oxide or alumina structures are achieved by a two-step mild anodization (MA) process. The procedure was first reported in the work of *Masuda et al.*^{5, 55}. In the first anodization step a disordered porous alumina layer grows on the aluminum surface and self-assembles into a hexagonal lattice. The alumina layer is subsequently etched away by a wet-chemical step. The remaining aluminum layer is patterned with hexagonal arrays of alumina. In the second step well-ordered nanopores grow on these arrays.⁵⁶⁻⁵⁸ The interpore distance D_{int} , the pore diameter/size D_p , and the pore depth T_p are controlled by the choice of electrolyte such as oxalic, sulfuric or phosphoric acid and the anodization parameter (i.e., voltage, or time) (Figure 2.1 and inset).

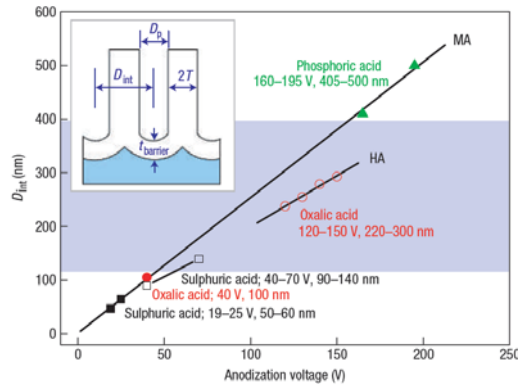


Figure 2.1: Summary of relationship between interpore distance D_{int} , voltage and electrolyte. Reproduced from ref 59.

Interpore distance and pore size are proportional to the voltage. The pore depth depends on the time in the second anodization step. Additional pore diameters are achieved by

an isotropic pore widening process after the second anodization step. The resulting pores are arranged on hexagonal domains which extend over 10–20 lattice constants. In this work AAO membranes with pore sizes ranging from 25 nm to 400 nm and pore depths of $\sim 100\ \mu\text{m}$ were referred to as AAO 20/25, 35, 60, 100, 180, or 400 nm. Preparation details are listed in Table 2.1 and Table 2.2.

Table 2.1: Anodization and widened parameters for AAO 20/25, 35 and 60 nm.

AAO membrane	[nm]	20/25 +		20/25 +		35 + widened	
		20/25	widened to 35	widened to 35		35	to 60
acid		H_2SO_4	$\text{C}_2\text{H}_2\text{O}_4$	H_3PO_4		$\text{C}_2\text{H}_2\text{O}_4$	$\text{C}_2\text{H}_2\text{O}_4$
voltage	[V]	25	/	/		40	/
temperature	[°C]	1–2	30	30		3–5	30
1 st anodization	[min]	1440	60	6		2100	120
2 nd anodization	[min]	1440	/	/		2400	/

Table 2.2: Anodization and widened parameters for AAO 100, 180 and 400 nm.

AAO membrane	[nm]	100		180		180 + widened to	
						400	
1 st anodization							
acid		$\text{C}_2\text{H}_2\text{O}_4$	H_3PO_4			H_3PO_4	
voltage	[V]	40	22			/	
temperature	[°C]	3–5	0–1			30	
time	[min]	30	360			120	
acid		$\text{C}_3\text{H}_4\text{O}_4$	H_3PO_4				
voltage	[V]	125	195				
temperature	[°C]	3–5	0–1				
time	[min]	1320	1080				
2 nd anodization							
acid		$\text{C}_3\text{H}_4\text{O}_4$	H_3PO_4				
voltage	[V]	125	195				
temperature	[°C]	3–5	0–1				
time	[min]	1320	1080				

2.2 Controlled Porous Glasses (CPG)

The second used model matrices are controlled porous glasses (CPG). They have a bicontinuous morphology and contain interconnected, curved nanopores with narrow pore size distribution. Porous glasses are leaching products of phase-separated alkali borosilicate glasses. The textural properties such as surface area, pore volume, and porosity are well investigated. The parameters are estimated based on mercury intrusion and nitrogen absorption and are listed in Table 2.3. Further details can be found in the study of *Enke et al.*⁶. Used CPG membranes had pore diameters ranging from 2 nm to 60 nm. The samples were hereinafter referred to as CPG 2, 25, or 60 nm, respectively.

Table 2.3: Textural properties of CPG membranes.

pore diameter [nm]	internal surface area [m ² g ⁻¹]	specific pore volume [cm ³ g ⁻¹]	porosity [%]
60	25.9	0.364	41
25	102	0.366	42
2	271	0.113	

The SEM image of a 60 nm AAO membrane (Figure 2.2a) shows ordered ‘honeycomb’ structures. Material confined to such structures reveals anisotropic behavior. In contrast, the SEM image of a 60 nm CPG (Figure 2.2b) shows a ‘spongelike’ pore system and infiltrated material exhibits isotropic properties. Both matrices have hydroxyl-terminated, oxidic pore walls.

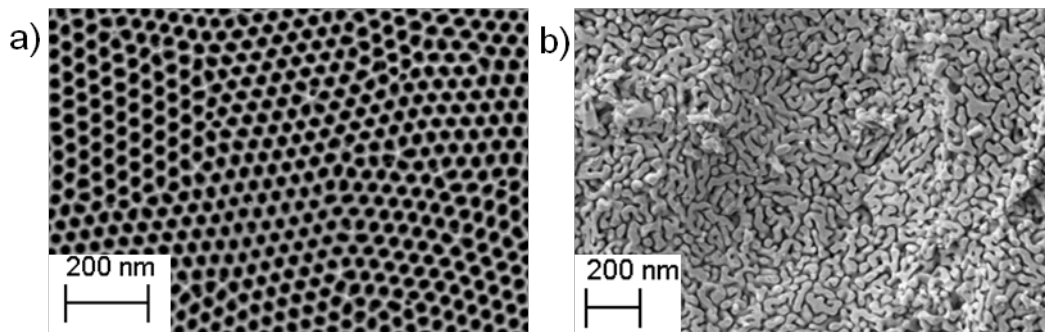


Figure 2.2: SEM images of the two nanoporous matrices; (a) anodic aluminum oxide (AAO), (b) controlled porous glasses (CPG).

2.3 Acetaminophen (ACE)

N-(4-hydroxyphenyl)acetamide (acetaminophen or paracetamol) $C_8H_9NO_2$ (Figure 2.3) has been selected as a low-molecular weight polymorphic model compound. Acetaminophen is a widely known analgesic and antipyretic drug and is used for the relief of fever, headaches and other minor aches and pains. Further, acetaminophen is a main ingredient in numerous cold and flu medications as well as in many prescription analgesics.⁶⁰

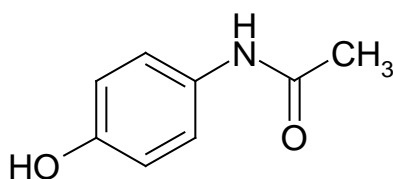


Figure 2.3: Structure of acetaminophen $C_8H_9NO_2$.

Acetaminophen occurs in three polymorphic forms mostly named as form I, form II and form III. At room temperature, the thermodynamically stable polymorph is form I and crystallizes in the monoclinic space group $P2_1/n$ with four molecules in the unit cell ($Z = 4$). The cell parameters are $a = 11.73 \text{ \AA}$, $b = 9.38 \text{ \AA}$, $c = 7.11 \text{ \AA}$, $\beta = 97.47^\circ$ based on reference CSD deposition number HXACAN03⁶¹. Note Figure 2.4 shows the unit cell of acetaminophen form I based on CSD-HXACAN04.

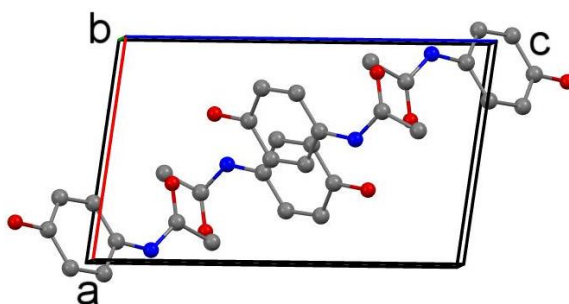


Figure 2.4: Unit cell of monoclinic acetaminophen form I, visualized with Mercury 3.1 based on CSD deposition number HXACAN04⁶². Oxygen atoms are red, nitrogen atoms are blue, carbon atoms are gray, and hydrogen atoms are not shown.

Polymorphic form II crystallizes in the orthorhombic space group $Pbca$ with $Z = 8$. The cell parameters are $a = 7.41 \text{ \AA}$, $b = 11.84 \text{ \AA}$, $c = 11.16 \text{ \AA}$ based on CSD deposition number HXACAN23⁶³ (Figure 2.5).

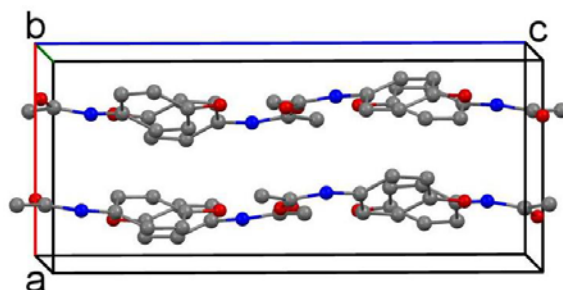


Figure 2.5: Unit cell of orthorhombic acetaminophen form II, visualized with Mercury 3.1 based on CSD deposition number HXACAN23⁶³. Oxygen atoms are red, nitrogen atoms are blue, carbon atoms are gray, and hydrogen atoms are not shown.

Polymorph form III is inaccessible in bulk material⁶⁴ and is only obtained under special crystallization conditions. A crystal structure very close to form II is reported for form III. Acetaminophen form III⁶⁵ crystallizes in the orthorhombic space group $Pca2_1$, $Z = 8$, with unit cell parameters $a = 11.84 \text{ \AA}$, $b = 8.56 \text{ \AA}$, $c = 14.82 \text{ \AA}$. A second crystal structure⁶⁶ suggests that form III crystallizes in the monoclinic space group $P2_1/c$ with unit cell parameters $a = 16.05 \text{ \AA}$, $b = 5.07 \text{ \AA}$, $c = 9.65 \text{ \AA}$, $\beta = 79.1^\circ$.

Nevertheless, despite other properties, the three polymorphs differ in their melting points. Form I has a bulk melting temperature at $T_m = 167\text{--}169^\circ\text{C}$, form II melts at $156\text{--}158^\circ\text{C}$ and form III shows a bulk melting temperature around 143°C .^{7, 67}

Beside crystalline formulations drugs exist in an amorphous form. Amorphous forms tend to convert into crystalline structures due to higher Gibbs energies. The lifetime of such amorphous drugs may be an important issue in pharmaceutical investigations. Amorphous forms often have physical instability and show higher dissolution rates²⁴ than their crystalline counterparts. As a consequence, amorphous forms could have a better bioavailability.

2.4 *n*-Alkanes: *n*-Tetracosane

n-Tetracosane, chosen as the second model compound, is a member of the normal alkanes family. Normal alkanes or short *n*-alkanes are some of the simplest organic molecules, but the main building blocks of lipids, surfactants, liquid crystals or polymers. *n*-Alkanes are also common materials in applied science. They are the basic constituents of crude petroleum or pharmaceuticals.⁶⁸ Crystallization of *n*-alkanes have been studied for important industrial applications. *n*-Tetracosane ($C_{24}H_{50}$) has a linear hydrocarbon chain where for energetic reasons all carbon atoms are in the *trans* position. The length of the carbon-carbon (C–C) bonds is 1.54 Å and the angle between the bonds is 112° ⁶⁸ (Figure 2.6).

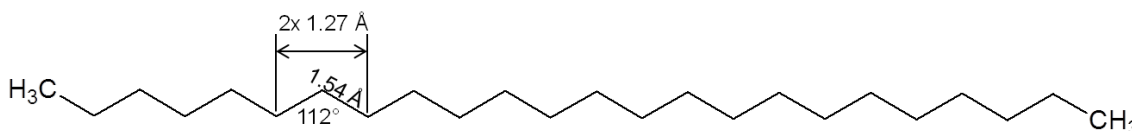


Figure 2.6: Structure of *n*-tetracosane ($C_{24}H_{50}$) with C–C bond length and bond angle.

n-Tetracosane, an even medium length *n*-alkane, shows a series of rotator phases between the crystalline and the isotropic liquid phase. Rotator phases are characterized by changes in the structure constants as a function of temperature.^{68, 69} Five rotator phases henceforth referred to as R_I to R_V have been identified for *n*-alkanes. They are characterized in terms of side packing, molecular tilt, layer stacking and azimuthal ordering.⁷⁰ Rotator phases referred for *n*-tetracosane, ordered for increasing temperature, are R_V , R_I and R_{II} . The rotator phases can differ in symmetry, in-plane molecular packing, layering sequences and molecular tilt. For example, the rotator phase R_I is orthorhombic and contains a rectangular distorted hexagonal lattice with non-tilted molecules. R_I has an AB layer stacking sequence. The R_{II} or high temperature phase is also non-tilted and the molecules are packed in a hexagonal lattice with an ABC layer sequence. The R_{II} phase has the highest symmetry. The rotator phase R_V is

like R_I but the molecules are tilted.^{51, 68, 69} The rotator phase sequence with corresponding temperatures is shown in Figure 2.7.

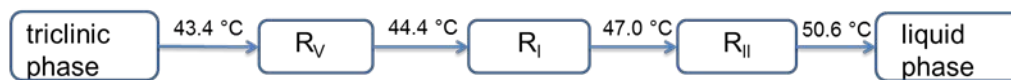


Figure 2.7: Phase transitions temperatures of *n*-tetracosane: triclinic to rotator phase (triclinic→ R_V), rotator to rotator phase (R_V → R_I , R_I → R_{II}), and rotator to liquid phase (R_{II} →melt). Reproduced from ref 69.

The second phenomenon is that *n*-tetracosane or in general *n*-alkanes form lamellar crystals. In lamellar crystals the molecule chains are aligned normal to the layers and closely packed, side by side (Figure 2.8). The layers have a stacking sequence which can change during phase transition as previously mentioned. In X-ray experiments the layer structures show typical reflections in the lower 2θ range. The layer reflections display a temperature-dependent behavior⁷¹.

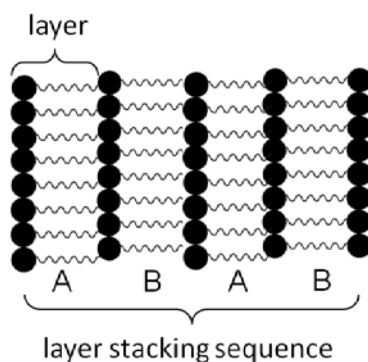


Figure 2.8: Schematic view of the lamellar arrangement. The molecule long chains are oriented normal to the layers which have an AB layer stacking sequence.

Layer spacing or layer thickness can be estimated with the Bragg equation (see Eq. 3.1). Different factors can have an influence on the layer thickness. For example, a tilting of the molecules or ‘gauche’ defects will reduce the thickness. On the other hand, a change in the layer sequence can result in higher layer spacings.⁶⁹

n-Tetracosane crystallizes at room temperature in the triclinic space group P-1, $Z = 1$ and with the unit cell parameters $a = 4.29 \text{ \AA}$, $b = 4.82 \text{ \AA}$, $c = 32.54 \text{ \AA}$, $\alpha = 86.19^\circ$, $\beta = 68.55^\circ$, $\gamma = 72.20^\circ$ based on CSD deposition number ZZOF04⁷² (Figure 2.9). The molecule long chains are stacked together and oriented aligned to the unit cell long axis *c*.

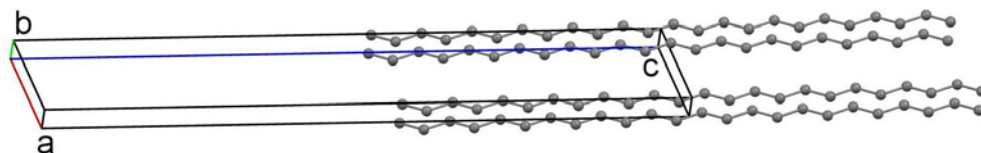


Figure 2.9: Unit cell of triclinic *n*-tetracosane, visualized with Mercury 3.1 based on CSD deposition number ZZOF04⁷². Carbon atoms are gray and hydrogen atoms are not shown.

For *n*-tetracosane more crystallographic parameters are stored in the Cambridge Structural Database (CSD)⁷³. Table 2.4 lists the CSD deposition number, unit cell parameters and the polymorph description based on reference 74. It should be kept in mind that rotator phases differ in their molecular arrangement resulting in different WAXS patterns and hence, in different unit cells. The reported data are not referred to the possible rotator phases R_V , R_I , or R_{II} , respectively.

Table 2.4: Unit cell parameter of *n*-tetracosane.

CSD deposition number	cell length [\AA]			cell angles [$^\circ$]			polymorph name ⁷⁴
	a	b	c	α	β	γ	
ZZZOF04	32.7	4.99	7.50	90	94	90	II
ZZOF01	33.2	4.95	7.94	90	94	90	I
ZZZOF02	7.42	31.2	5.35	94.7	99	87.8	low temperature
ZZZOF03	4.77	4.77	33.3	90	90	120	high temperature

3 Experimental Section

3.1 Sample Preparation

(1) AAO Pore Wall Modification with ODPA

Surface modification of AAO nanopores is possible by employing certain coupling agents which can covalently bind to the AAO surface. A coupling agent comprises of three parts: an anchor, a spacer and a terminal functional group. For surface modification of the AAO membranes octadecylphosphonic acid (ODPA) $C_{18}H_{39}PO_3$ was chosen. Extended ODPA is a nearly 25 Å long linear molecule, with a lengthy alkyl chain of approximately 22 Å and a polar head group. The $PO(OH)_2$ functional group interact with the alumina hydroxyl groups on the surface. The head group binds via acid–base condensation reaction mechanism. The end group of the molecule determines the properties of the AAO membrane. Nonpolar groups, like methyl ($-CH_3$), render the surface hydrophobicity.⁷⁵⁻⁷⁸ As a result, the surface chemistry changes to a hydrophobic low-energy surface.⁷⁹⁻⁸¹ The modification of AAO membranes were done simply by solution deposition.⁸² The AAO membranes were activated in 30% aqueous H_2O_2 solution at 45 °C for 2 h, dried at 120 °C for 15 min, and immersed in ODPA solution (4.2 mM ODPA *n*-heptane/2-propanol a 5:1 (v/v) mixture) at 25 °C for 48 h. After immersion the AAO membranes were rinsed, and dried at 50 °C under vacuum.^{17, 83, 84} After modification (Figure 3.1) the AAO nanopores remain open.

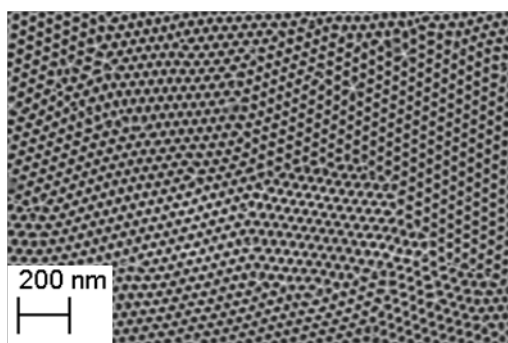


Figure 3.1: SEM image of AAO 60 nm ODPA-modified.

Prior to infiltration of AAO membranes with guest material, each membrane was annealed at 180°C for 2 h under vacuum to remove traces of water. The membranes were weighed before and after infiltration.

*(2) Infiltration of the AAO Membranes with ACE and *n*-Tetracosane*

In general, infiltration and crystallization took place in a temperature program controlled furnace. The unit involves a furnace connected to argon or vacuum supply, the cooling system, and the temperature controller (Eurotherm 2416). For infiltration, the furnace was fast heated up to the wetting temperature and the AAO membranes were placed in the furnace (Figure 3.2). After few minutes, acetaminophen or *n*-tetracosane were put on the surface and spread by a spatula. The furnace was closed, and connected to the argon supply. AAO membrane was allowed to wet by acetaminophen at 175 °C for 30 minutes, *n*-tetracosane at 80 °C for 12 h, respectively.

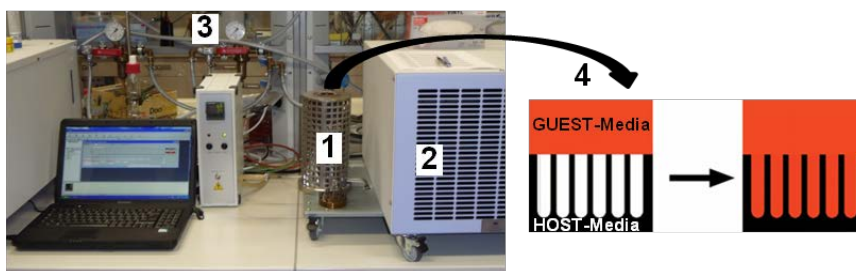


Figure 3.2: Temperature controlled furnaces (1) with cooling system (2) and Argon or Vacuum supply (3), infiltration of the AAO membranes inside the furnace (4).

(3) Etching of the AAO Membranes Aluminum Substrate and AAO Pore Bottom Opening

Controlled porous glasses (CPG) could be directly subjected to DSC and TGA measurements (see Ch. 3.3). On the contrary, the aluminum substrate of AAO membranes must be etched away before the measurements. The aluminum was removed using copper chloride solution. The solution contained 1.7 mg of $\text{CuCl}_2 \cdot 2\text{H}_2\text{O}$, 50 mL deionized water and 50 mL concentrated HCl. In order to prevent contact of etching reagent with the AAO pore openings, the membrane was mounted on a specifically designed sample holder (Figure 3.3) placed in an ice bath. Aluminum was slowly etched

away. Afterwards, the membrane was dried under vacuum, thereby leaving the alumina (Al_2O_3) matrix with the infiltrated/crystallized guest material. For pore bottom opening, the dried membrane was placed carefully on the surface of 10% H_3PO_4 solution at 30 °C followed by thorough washing with deionized water and subsequent drying under vacuum.

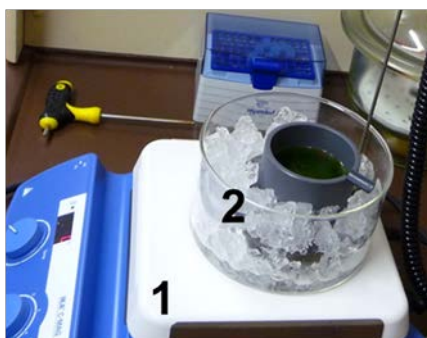


Figure 3.3: Etching of the aluminum substrate with stirrer (1) and sample holder in an ice bath (2).

(4) Infiltration of CPG Membranes with ACE

CPG membranes were infiltrated on a hot-stage heated to 180 °C. Bulk acetaminophen was melt in a small beaker and the CPG were placed in the molten material for 2 min. With the density of acetaminophen (form I: 1.293 g cm^{-3} , form II: 1.336 g cm^{-3})⁴⁴, the specific pore volume, and the infiltrated amount of acetaminophen the pore filling can be calculated. For 60 nm CPG 85–95% filling of the pore volume was achievable.

(5) Non-isothermal Crystallization of AAO and CPG Membranes Infiltrated with ACE

In general, melt-infiltrated acetaminophen inside the nanopores was cooled with a fast (quenched) or slow (-0.5 K/min) cooling rate (Figure 3.4). During fast cooling process, hot AAO membranes were removed from the furnace, the CPG from the beaker, and then quenched below 0 °C by placing the membranes on a cooled copper-plate under ambient conditions. During slow cooling process the AAO membranes were left in the furnace and cooled at a rate of -0.5 K/min to room temperature under argon. During the cooling processes acetaminophen inside the pores has contact to (a) a bulk surface reservoir or (b) surface material was removed before cooling. For latter purpose, the

infiltrated AAO or CPG membranes were placed on a hot-stage heated to 180 °C and excess surface material was removed with a tissue paper. Then, the samples were placed back into the furnace, after 5 min slowly cooled down under argon or quenched below 0 °C on a cooled copper-plate.

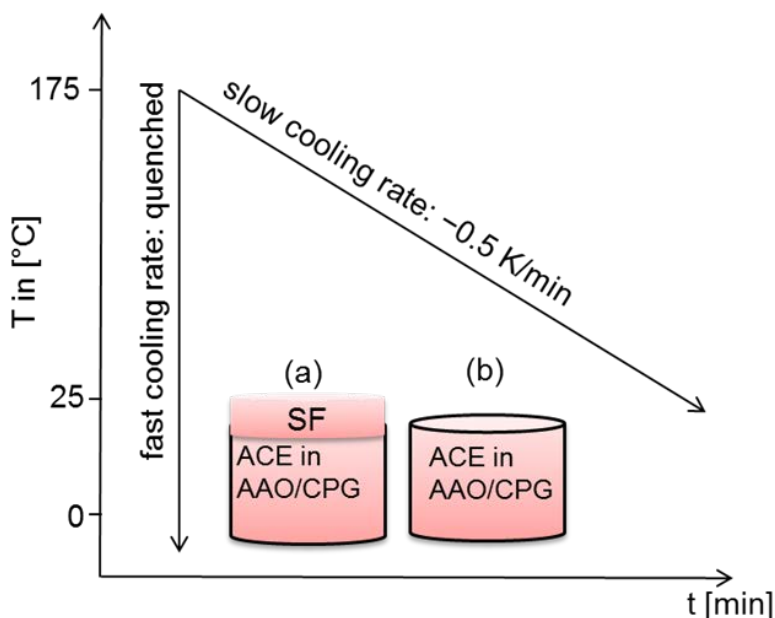


Figure 3.4: Temperature program of the cooling rates; (a) The infiltrated acetaminophen was cooled (a) in the presence or (b) in the absence of a bulk surface reservoir. SF stands for bulk surface material.

(6) Cold Crystallization (Isothermal Crystallization) of AAO Membranes with ACE

Infiltrated AAO membranes were placed on a hot-stage heated to 180 °C for approximately 2 min. The hot membranes were quenched below 0 °C on a pre-cooled copperplate, stored below -10 °C for 10 min. The process was repeated. During reheating one sample set has contact to the bulk surface reservoir while the other has no contact. Isothermal or cold crystallization (CC) takes place inside the furnace at a temperature between 80–90 °C for a certain time period (from 2 h to 4 days) under argon. The samples in nanopores were cold crystallized with and without access to bulk acetaminophen surface material.

(7) Infiltration of CPG Membranes with n-Tetracosane

As a second model compound, *n*-tetracosane was infiltrated in CPG membranes on a hot-stage heated to 80 °C. The CPG were placed in bulk material (contained in a beaker) for 10 min, quickly transferred to the furnace and subjected to cooling.

(8) Non-isothermal Crystallization of AAO and CPG Membranes Infiltrated with n-Tetracosane

After infiltration *n*-Tetracosane was cooled to 25 °C at a cooling rate of –0.5 K/min in the presence or in the absence of bulk surface reservoir, respectively. For latter purpose the infiltrated samples were put on a hot-stage heated to 80 °C and excess bulk surface material was removed with a tissue-paper before cooling. Then, the samples were placed back into the furnace, re-infiltrated for 5 min, and crystallized at a cooling rate of –0.5 K/min under argon. Before WAXS measurements the bulk surface film was carefully removed. Membranes were weighed before and after infiltration. With the known density of *n*-tetracosane (0.773 g cm^{–3} at 333 K)⁸⁵ and the specific pore volume (Table 2.3), the total amount of filled material inside 100 nm and 25 nm CPG membranes was calculated to be around 100%, and almost 60% for 2 nm CPG.

(9) Summary of Prepared Samples

Table 3.1: Acetaminophen solidified in AAO and CPG membranes, infiltration parameter, cooling rates, connection to a bulk surface film and chapter number.

Crystallizable material	Membrane [nm]	Infiltration Parameter	Non-isothermal Cooling rate	Surface film	Chapter
acetaminophen	AAO 60	175 °C, 30 min	quenched	yes	5.1.1
acetaminophen	AAO 60	175 °C, 30 min	0.5 K/min	yes	5.1.2
acetaminophen	AAO 60	175 °C, 30 min	quenched	no	5.1.3
acetaminophen	AAO 60	175 °C, 30 min	0.5 K/min	no	5.1.3
acetaminophen	AAO 25	175 °C, 30 min	0.5 K/min	yes	5.4.1
acetaminophen	AAO 100	175 °C, 30 min	0.5 K/min	yes	5.4.1
acetaminophen	AAO 180	175 °C, 30 min	0.5 K/min	yes	5.4.1
acetaminophen	AAO 400	175 °C, 30 min	0.5 K/min	yes	5.4.1
acetaminophen	CPG 60	180 °C, 2 min	quenched	yes	5.3
acetaminophen	CPG 60	180 °C, 2 min	quenched	no	5.3
acetaminophen	CPG 60	180 °C, 2 min	0.5 K/min	yes	5.3

acetaminophen	CPG 60	180 °C, 2 min	0.5 K/min	no	5.3
cold					
crystallization					
(isothermal)					
acetaminophen	AAO 60	175 °C, 30 min	90°C, 4 days	no	5.2
acetaminophen	AAO 60	175 °C, 30 min	80°C, 2 h	yes	5.2
acetaminophen	AAO 25	175 °C, 30 min	80°C, 2 h	yes	5.4.2
acetaminophen	AAO 100	175 °C, 30 min	80°C, 2 h	yes	5.4.2
acetaminophen	AAO 180	175 °C, 30 min	80°C, 2 h	yes	5.4.2
acetaminophen	AAO 400	175 °C, 30 min	80°C, 2 h	yes	5.4.2
acetaminophen	AAO 25	175 °C, 30 min	80°C, 2 h	no	5.4.2
acetaminophen	AAO 100	175 °C, 30 min	80°C, 2 h	no	5.4.2
acetaminophen	AAO 180	175 °C, 30 min	80°C, 2 h	no	5.4.2
acetaminophen	AAO 400	175 °C, 30 min	80°C, 2 h	no	5.4.2

Table 3.2: *n*-Tetracosane solidified in AAO and CPG membranes, infiltration parameter, cooling rates, connection to a bulk surface film and samples names.

Crystallizable material	Membrane [nm]	Infiltration Parameter	Non-isothermal Cooling rate	Surface film	Sample names
<i>n</i> -Tetracosane	AAO 60	80 °C, 12 h	0.5 K/min	yes	case A
<i>n</i> -Tetracosane	AAO 25	80 °C, 12 h	0.5 K/min	yes	case B
<i>n</i> -Tetracosane	AAO 60 ODPA-mod	80 °C, 12 h	0.5 K/min	yes	case C
<i>n</i> -Tetracosane	AAO 60	80 °C, 12 h	0.5 K/min	no	case D
<i>n</i> -Tetracosane	AAO 25	80 °C, 12 h	0.5 K/min	no	case E
<i>n</i> -Tetracosane	AAO 60 ODPA-mod	80 °C, 12 h	0.5 K/min	no	case F
<i>n</i> -Tetracosane	CPG 60	80 °C, 12 h	0.5 K/min	yes	case G
<i>n</i> -Tetracosane	CPG 25	80 °C, 12 h	0.5 K/min	yes	case H
<i>n</i> -Tetracosane	CPG 25	80 °C, 12 h	0.5 K/min	yes	case I
<i>n</i> -Tetracosane	CPG 60	80 °C, 12 h	0.5 K/min	no	case J
<i>n</i> -Tetracosane	CPG 25	80 °C, 12 h	0.5 K/min	no	case K
<i>n</i> -Tetracosane	CPG 25	80 °C, 12 h	0.5 K/min	no	case L

3.2 X-ray Diffraction

3.2.1 Principles

X-ray diffraction is an important tool to investigate crystal structures. X-rays are electromagnetic radiations with wavelengths of the order 10^{-10} m. There are two waves in the same region of space they can interfere: constructively to have enhanced or destructively to have smaller amplitudes. X-rays are generated by directing an electron beam onto a cooled metal target. The electrons decelerate when they hit the metal and generate radiation with a continuous range of wavelengths (Bremsstrahlung). Sharp peaks arise from the collision of the incoming electrons with inner shell electrons. The electron from the inner shell emits and into the vacant site can drop an electron from a higher energy state, emitting the excess energy as an X-ray photon. If an electron falls into a K shell the X-rays are categorized as K-radiation (e.g., K_{α} , K_{β} lines).³³ In crystalline samples, for certain sharply define wavelengths, incident and diffraction directions, intense peaks of scattered radiation can be observed. The simplest way to describe such diffracted X-rays is given by the *Bragg Law*:

$$n\lambda = 2d \sin \Theta \quad 3.1$$

where λ is the wavelength, θ is the scattering angle, d is the lattice spacing and n is an integer number. Constructive interference results in reflections. At this time the incident X-rays are elastically scattered by the atoms or molecule in any lattice plane^{30, 33} (Figure 3.5).

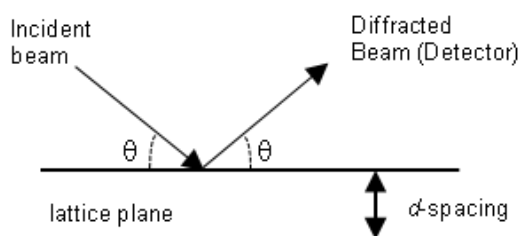


Figure 3.5: Bragg reflections from particular family of lattice planes where incident beam and diffracted beam enclose an angle of θ .

The observed diffraction peaks are displayed as diffracted intensities at a range of 2θ angles. Ideal conditions (i.e., perfect crystal and instrumentation) should give peaks with the shape of a delta function. In reality, the peaks broaden because of imperfect crystal structure, atomic thermal vibration or instrumental settings, etc. The X-ray diffraction (XRD) pattern gives a peak profile line which places the diffracted intensity distribution I over the selected Bragg angle θ . The highest point in the profile corresponds to the maximum intensity I_{max} . The width of the peak is characterized with the *full width at half-maximum* (FWHM) value.³⁰ The scattered X-rays form a specific diffraction pattern which depends on the atomic arrangement. When the materials have long- or short-range order the diffraction pattern of a specific material has more or less sharp peaks. The peaks correspond to various lattice planes based on the Bragg law, whereby peaks at lower 2θ angles come from planes of large d -spacing and vice versa. A diffraction pattern can be collected from a single crystal or from polycrystalline materials. Crystallographic parameters for many compounds are collected in the Cambridge Structural Database (CSD)⁷³ and can be used for comparison and structure drawing, for example. Materials with no long-range order like liquids or amorphous solids have only a narrow atomic distance distribution. The intensity of the scattered X-rays forms a very broad distribution in the 2θ range referred to as amorphous halo.

For X-ray studies the scattering data are analyzed in terms of the reciprocal lattice. The reciprocal lattice is a transformation of the crystal lattice in real space to reciprocal space. The reciprocal lattice is then defined by three vectors a , b , c of the unit cell and all start from a single lattice point. The unit cell of the corresponding reciprocal lattice is given by:

$$a^* = \frac{1}{V}(b \times c), b^* = \frac{1}{V}(c \times a), c^* = \frac{1}{V}(a \times b), V = a \cdot b \times c \quad 3.2$$

where V is the volume of the crystal unit cell in real space.

As can be seen each reciprocal lattice axis is a vector product of two lattice axis in real space, the reciprocal lattice axis is perpendicular to the planes which are defined by two lattice axis. For example, the reciprocal lattice vector a^* is perpendicular to the planes

defined by the lattice axis bc . The unit cell and the reciprocal lattice axes have the following relations:

$$a \cdot a^* = b \cdot b^* = c \cdot c^* = 1 \quad 3.3$$

$$b \cdot a^* = c \cdot a^* = a \cdot b^* = c \cdot b^* = b \cdot c^* = a \cdot c^* = 0 \quad 3.4$$

The origin of the reciprocal lattice axes, denoted by O , is also the origin of the reciprocal lattice³⁰ (see also point O in Figure 3.6). In reciprocal space each lattice point is denoted by three integers (hkl) which are the numbers of translation of the three reciprocal axes. The integers are equal to a point H_{hkl} in the reciprocal space and the vector drawn from the origin to the lattice point (hkl) is given by:

$$H_{hkl} = ha^* + kb^* + lc^* \quad 3.5$$

The direction of the vector H_{hkl} is normal to the lattice planes (hkl) in real space and the magnitude of the vector is given by the d -spacing d_{hkl} :

$$|H_{hkl}| = \frac{1}{d_{hkl}} \quad 3.6$$

Each point (hkl) in the reciprocal lattice corresponds to a set of crystal faces in the real lattice. The position of the point indicates the orientation and d -spacing of the lattice planes in real space. As a result, the farther away a reciprocal lattice point is from the origin, the smaller is the d -spacing of the corresponding lattice planes.³⁰

A relationship between the Bragg conditions and the reciprocal lattice is given by the Ewald sphere. In Figure 3.6 the sample is located in the center of the Ewald sphere, C . The radius is defined by $1/\lambda$ with λ as the wavelength.

The incident beam s_o/λ is the vector from C to O and hence, the diffracted beam s/λ is the vector from C to P , where s_o is the unit vector representing the incident beam, and s is the unit vector representing the diffracted beam. The vector from O to P is the reciprocal lattice vector H_{hkl} . As previously mentioned, point O is the origin of the reciprocal lattice and P is the reciprocal point (hkl) . The distance between O and P is

reciprocal to the d -spacing. The Bragg law can now be expressed in vector form and equation 3.6 can be written as:

$$|H_{hkl}| = \frac{1}{d_{hkl}} = \left| \frac{s - s_0}{\lambda} \right| = \frac{2 \sin \theta}{\lambda} = S \quad 3.7$$

where S is the scattering vector.

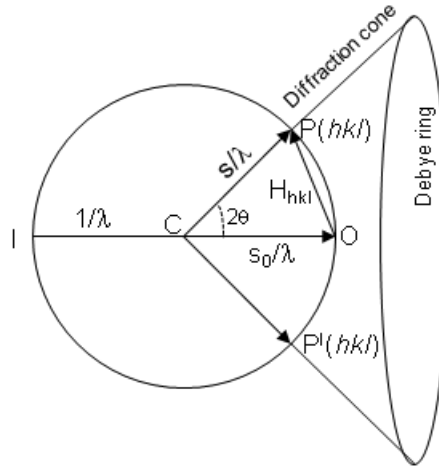


Figure 3.6: The Ewald sphere in reciprocal space with diffraction vector cone and one Debye ring belonging to a fixed θ angle.

Reciprocal lattice vectors with a given length (reciprocal d -spacing) point to the surface of a sphere around the origin of the reciprocal space O . The intersection of this sphere with the Ewald sphere is the Debye ring⁸⁶ belonging to the corresponding reflection (Figure 3.6). Powder or polycrystalline samples are completely random. Crystallites can have all possible orientations. Therefore, diffracted intensities which belong to a fixed θ angle corresponding to reciprocal lattice vectors will form Debye rings with different lengths.

Translated to the used X-ray geometry a sample is positioned in the $X_L Y_L$ plane at position C , incident and diffracted beams are located in the $Y_L Z_L$ plane in real space (Figure 3.7a). For theta/2theta measurements the incident beam is fixed and the detector

moves in the $Y_L Z_L$ plane. Transformed into the reciprocal space the scattering vector S is directed along the Z axis (Figure 3.7b).

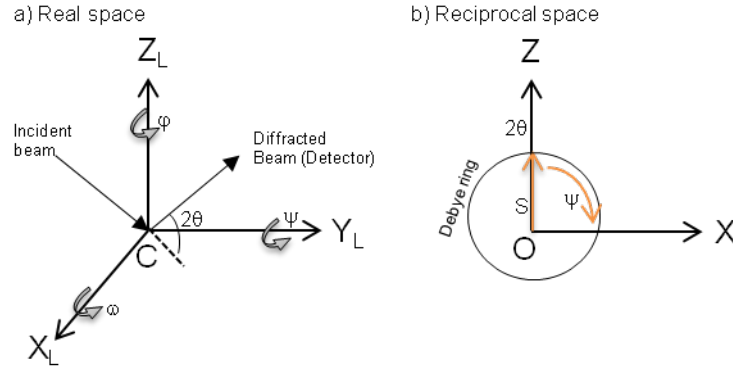


Figure 3.7: X-ray diffraction geometry in real space and transfer into the reciprocal space.

During theta/2theta scan the length of the scattering vector is varied along this Z direction. For texture measurement (see Ch. 3.2.3), the scattering vector rotates in the XZ plane along the Debye ring in the reciprocal space. Translated back to real space, the sample is rotated around the Y axis in the $X_L Z_L$ plane (Figure 3.7a).

3.2.2 Set-up X-ray Diffractometer

XRD patterns were obtained using a PANalytical X'Pert Pro MRD diffractometer with $\text{CuK}\alpha$ radiation (40 kV, 40 mA) and a wavelength of 0.15406 nm. The samples are mounted on an Eulerian cradle that can be rotated about three axes (ω , ψ , ϕ) (Figure 3.7a). Theta/2theta scans and Schulz scans can be measured in reflection mode. The scattered radiation is collected by a linear detector in point focus. For theta/2theta scans a PIXcel detector with anti-scatter slit 7.5 mm on the diffracted beam site is used (Figure 3.8 number 3). Furthermore, the configuration includes a crossed slit collimator (settings: mask 3.00 mm, divergence slit 0.25 mm) and a prefix module (poly-capillary

lens 8 mm) for the incident beam (Figure 3.8 number 1). Measurement conditions were as follow: 0.03° step size, 500 s time per step, scan range $5\text{--}40^\circ$ 2θ .

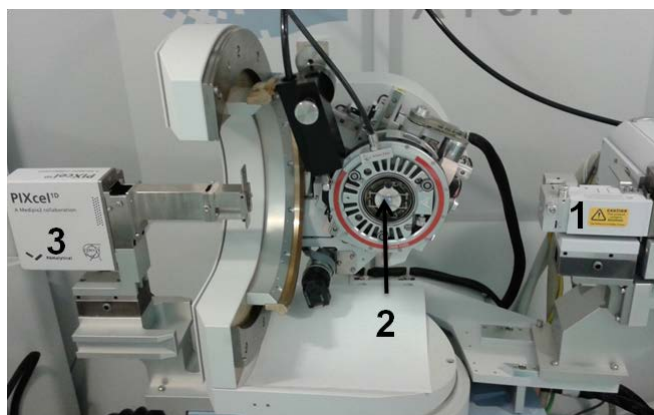


Figure 3.8: PANalytical X'Pert Pro MRD with incident beam optics (1), Anton Paar hot-stage DHS 1100 (2) and diffracted beam optics (3).

The Eulerian cradle can be equipped with an Anton Paar hot stage *DHS 1100* that allows performing temperature-dependent measurements (Figure 3.8 number 2). During $\theta/2\theta$ scans the samples are tilted around the θ axis which lies in the plane of the sample surface and is oriented perpendicularly to the scattering plane. Figure 3.9 displays the geometry used to investigate AAO membranes.

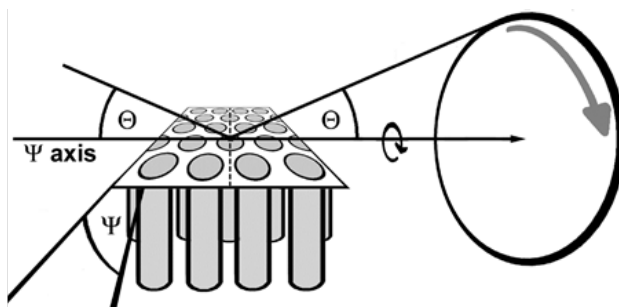


Figure 3.9: Geometry used for X-ray diffraction studies in real space. The sample is placed in such a way that the surface is oriented normal to the plane corresponding to the incident X-ray beam and the diffracted beam. The dotted line is the tilt axis (θ axis) in $\theta/2\theta$ scans. For Schulz scans the sample is rotated around the ψ axis (solid line). On the right, a Debye ring belonging to a fixed θ angle is indicated. Reproduced from ref 87.

During theta/2theta scans scattering intensity originating from sets of lattice planes oriented parallel to the AAO membrane surface were measured. The collected patterns were background-corrected and analyzed using the program PANalytical X'Pert HighScore.

3.2.3 Texture Analysis

Material confined to anisotropic pores such as anodic aluminum oxide (AAO) membranes can have anisotropic orientation properties referred to as preferred orientations or textures. Such samples have crystallites or grains with a preferred orientation at the macroscopic scale. Consequently, the crystal planes corresponding to such crystallite diffraction peaks also show a preferred orientation in response to the used scattering geometry. As a result, the diffraction intensity varies along Debye rings due to an anisotropic orientation distribution. Such orientation distribution can be measured with Schulz scans⁸⁸ at fixed θ and 2θ angles. During Schulz scans the sample is rotated along the ψ axis by the angle ψ (Figure 3.9). The ψ axis lies in plane of the sample surface and the scattering plane but is oriented perpendicular to the θ axis.

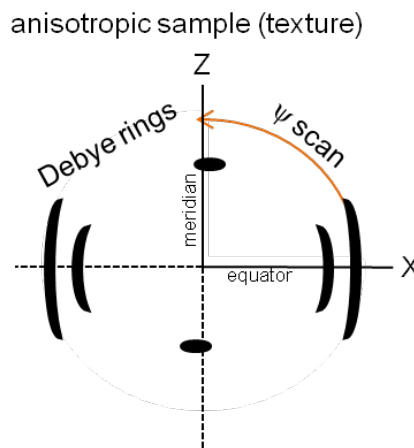


Figure 3.10: Schulz scan of a textured sample in the reciprocal space; Debye rings with anisotropic density distributions. For Schulz scans the sample is rotated around the ψ axis which is oriented normal to the equator and meridian. Theta and 2theta angles are fixed.

Schulz scans yield scattering intensity profiles $I(\psi)$. The profiles represent orientation distributions of sets of lattice plans belonging to the selected 2θ angles relative to the sample surface. Due to the symmetry of the orientation distribution of the crystallites, it is sufficed to measure the density distribution along the Debye ring only between the angles $0-90^\circ$ i.e., between equator and meridian as shown in Figure 3.10.

For Schulz scans the system was equipped with a PW3011/20 proportional point detector with parallel plate collimator 0.27° on the diffracted beam site. The incident beam path has a prefix module (poly-capillary lens 8 mm) and the crossed slit collimator was adjusted at 0.50 mm in width (mask) and at 0.50 mm at height (divergence slit). Measurement conditions were as follow: 0.5° step size, 20 s time per step, scan range $0-90^\circ$ psi or for non-ambient program scan range $0-70^\circ$ psi. Note $I(\psi)$ profiles are only accessible up to $\psi \sim 70^\circ$ due to defocusing effects^{89, 90}.

3.2.4 Data Interpretation

The degree of orientation distributions can be calculated with the Hermans' order parameter f ⁹¹. The parameter is defined as follow:

$$f = \frac{3}{2} \langle \cos^2 \psi \rangle - \frac{1}{2} \quad 3.8$$

$$\langle \cos^2 \psi \rangle = \frac{\sum_{i=1}^k [I(\psi)_i \cdot \cos^2 \psi_i]}{\sum_{i=1}^k I(\psi)_i}$$

where I is the intensity and k is the number of data points of the collected ψ scan. The f value gives the degree of orientation relative to a reference direction in uniaxial systems; i.e., lattice planes oriented parallel to the sample surface or normal to the AAO pore axis. An f value of 1 indicates perfect uniaxial orientation, and zero value, on the other hand, depicts absence of nonrandom orientations. The orientation distribution of

crystal planes relative to the AAO surface were calculated from baseline-corrected $I(\psi)$ profiles.

Furthermore, crystalline coherence lengths can be calculated. Coherence lengths are length of crystals when they have single crystal properties. As previously mentioned, due to the finite size of the crystals, diffraction beams are broadened. The broadening is expressed by the half peak width of half-maximum. The FWHM values increase as the coherence lengths decrease. Coherence lengths can be estimated by the Scherrer method⁹² according to:

$$D_{hkl} = \frac{K \cdot \lambda}{2(\Delta\Theta) \cdot \cos \Theta} \quad 3.9$$

where $2(\Delta\theta)$ is the full width of half-maximum (FWHM) of the evaluated reflections in radians, λ is the wavelength of the X-rays (0.15406 nm), θ is the scattering angle and K is the dimensionless shape factor (0.89 for spheres). The Scherrer equation gives the coherence length along $[hkl]$ directions that are perpendicular to the (hkl) planes.

Additionally, when the unit cell is known, theoretical angles between crystal faces can also be calculated and compared with measured texture orientations. Crystal structure programs like Diamond 3.0d or Mercury 3.1 were used for visualizing unit cells and for calculation of theoretical angles.

3.3 Thermal Analysis

Differential scanning calorimetry is a thermal method which guides the heat capacity C of a material over a temperature range. A material sample with known mass is subjected to a particular temperature profile, and the change of the heat capacity is tracked as a function of heat flow. During the DSC measurements transitions in materials are recorded such as melting, glass transition, phase change or curing. The molar heat capacity C_m is an important thermodynamic property and defined as an amount of heat required to heat up material of 1 gram or mole by 1 Kelvin. The heat capacity can be

measured calorimetrically under constant pressure C_p or under constant volume C_v . The properties are defined as,

$$C_p = \frac{dH}{dT} \quad 3.10$$

$$C_v = \frac{dU}{dT} \quad 3.11$$

where H is the enthalpy, T is the absolute temperature and U is the internal energy.

Commercially, there are two types of DSCs available: heat flux or power-compensated. Figure 3.11 shows the latter with double-furnace DSC 8500 calorimeter from Perkin Elmer. The device is connected with the cooling system Intracooler 3 unit. The double-furnace design measures the heat flow or energy directly without any conversion which delivers more accurate heat-flow results. Both microfurnaces are equipped with temperature sensors and heaters supplied with electrical power. The identical microfurnaces operate independently. Interferences from outside i.e., fluctuation in temperature and pressure will affect both furnaces equally. One furnace contains a reference pan, while the other contains the sample pan. Since furnaces and pans are identical, their heat capacities can be considered as being equal.⁹³



Figure 3.11: Power Compensated DSC 8500 Perkin Elmer (1) with cooling device (2) and universal crimper press (3).

The signal from the sample is measured as the change in heat flow depicted as heating power (ΔP). At constant pressure, ΔP can be written as:

$$\Delta P = \frac{dQ_p}{dt} = \frac{dH_p}{dt} = C_p \cdot \frac{dT}{dt} \quad 3.12$$

where dQ_p is the heat transferred from or to the sample material, dH_p is the enthalpy change, t is the time, T is the temperature and C_p is the heat capacity. During a heating scan ΔP is positive since additional power is required to heat the sample. When the material undergoes transition, endothermic (melting) or exothermic (crystallization) reactions occur. The melting or crystallization temperatures can be determined from the heat flow or C_p curves. The area of the melting and crystallization peaks give melting (ΔH_m) and crystallization enthalpies, respectively. Some typical features are sketched in Figure 3.12. The DSC heating scan of the model material acetaminophen shows a huge melting peak during an exothermic reaction. The peak itself can be affected by several factors like heating rate, thermal conductivity, mass of the sample, and the sample position in the furnace, etc. The peak maximum temperature ($T_{m,peak}$) is the maximum value between the baseline and the measured curve values. The onset temperature ($T_{m,onset}$) is the point where the tangent or fitted line of the ascending peak intersects the baseline. Detailed readings are given in references 93, 94.

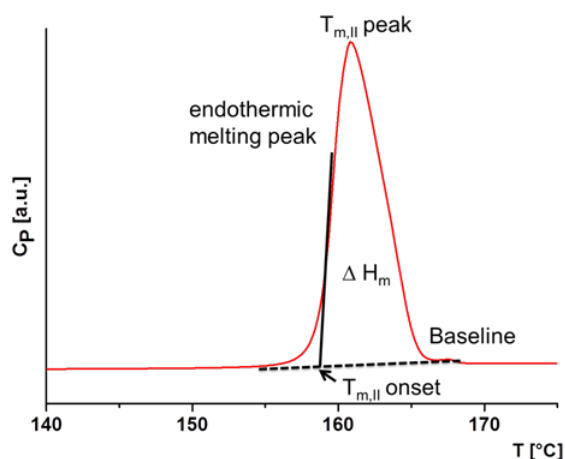


Figure 3.12: DSC heating curve (10 K/min) of bulk acetaminophen form II.

In Figure 3.12 acetaminophen form II shows the melting peak at $T_{m,II}$ onset ~ 159 °C. The glass transition temperature ($T_g \sim 24$ °C amorphous bulk acetaminophen) is not depictable at the temperature profile used. During heating of an amorphous material, the heat capacity increases and at some point the material has enough energy to relax into a

more ordered crystalline form. This requires a fair amount of energy which appears as a step in the DSC heat flow⁹⁵ referred to as glass transition temperature.

Melting points of bulk material or material embedded in nanopores matrices were measured using a power-compensated double-furnace DSC 8500 as mentioned earlier. CPG membranes could be used directly. The aluminum substrate of AAO membranes was removed before DSC and TGA (see Ch. 3.1). Then, 5–10 mg of the membranes were put in aluminum DSC pans, hermetically closed and placed in the DSC device.

As described above, when material is embedded in nanoporous hosts their properties may differ from the bulk material. Material under confinement exhibits a melting point depression. The depression results from the finite size of the crystallites inside the pores.^{21, 96} The melting point depression $T_{m(\text{confinement})}$ can be described with the Gibbs-Thomson equation⁹:

$$T_{m(\text{confinement})} = T_{m(\infty)} \cdot \left[1 - 4 \cdot \frac{\gamma_{CL}}{(d \cdot \Delta H_m \cdot \rho_C)} \right] \quad 3.13$$

where $T_{m(\infty)}$ is the melting temperature of the infinitely large crystal, γ_{CL} is the interfacial tension between crystal and liquid, ΔH_m is the heat of melting and ρ_C is the crystal density. The equation gives a relationship between the measured melting temperature $T_{m(\text{confinement})}$ and the crystal thickness d . Crystallization curves can be drawn which represent the association between the crystallization temperature and the inverse crystal thickness $1/d$ ⁹⁶ assuming that other parameters are independent of size. The same goes with melting curves, the melting point also shows a relationship to the inverse crystal thickness. The Gibbs-Thomson equation predicts a linear relationship between the melting point and the inverse particle size or pore size.

The thermo gravimetric analysis (TGA) is a technique where the mass loss of a material is monitored as a function of temperature or time. The measurements take place with a controlled temperature program and under controlled atmosphere. TGA measurements were carried out with a Netzsch STA 449 C^a. The samples were heated from 25 to 500 °C with a heating rate of 10 K/min.

^a Universität Osnabrück, Inst. für Chemie neuer Materialien, AK Haase

3.4 Scanning Electron Microscopy

Before scanning electron microscopy (SEM) AAO membranes were coated with a thin Pt/Ir layer. For high magnification images, a Zeiss Auriga CrossBeam Workstation EVO MA10 equipped with a Gemini FE-SEM column was used. Acceleration voltage between 1–3 kV was used to investigate the samples.

3.5 Electron Paramagnetic Resonance

Electron paramagnetic resonance (EPR) spectroscopy is a universal, sensitive and quantitative method to detect possible formation of radical species in solid materials.⁹⁷ EPR is a study of molecules and ions having unpaired electrons by observing the magnetic fields at which they come into resonance with monochromatic radiation.³³ Electrons have a spin with $s = 1/2$ and magnetic moment with $m_s = \pm 1/2$. If electrons extended to a magnetic field B_0 the electron spin is separated between $m_s = -1/2$ and $m_s = +1/2$ levels. The energy separations come into resonance with the radiation ν when the frequency satisfies the resonance condition:

$$h\nu = g_e\mu_B B_0 \quad 3.14$$

where h is the Planck' constant, μ_B is the Bohr magneton, and g_e is the g -value ($g_e \sim 2.0023$ for a 'free' electron). The magnetic moment of an unpaired electron interacts with an external field. But the g -value differs from that for a free electron because of local fields induced by the molecular framework of the radical.³³ Therefore the g -value gives information about the electronic structure.

4 AAO Membrane Characterization

4.1 Influence of Thermal and Water Treatment on AAO Membranes

In general, AAO membranes have hydroxyl-terminated pore walls. Further, the AAO nanopores contain physisorbed and chemisorbed water. Storage time and/or storage conditions (i.e., storage on air, in a desiccator under vacuum) may influence the amount of physisorbed water. Assuming that during heating only water evaporates thermo gravimetric analysis (TGA) is one option to measure the physisorbed and chemisorbed water. Thermo gravimetric analysis offers an opportunity to investigate the mass loss depending on the temperature and hence, depending on the membrane treatments.

AAO membranes with pore sizes of 25 nm (preparation step see Ch. 2.1 Table 2.1) were annealed at 180 °C or 400 °C for 2 h under vacuum. Before annealing the aluminum substrate of the AAO membranes was removed by an etching step (see Ch. 3.1). After annealing, some AAO membranes were placed in a beaker filled with water for 1 h.

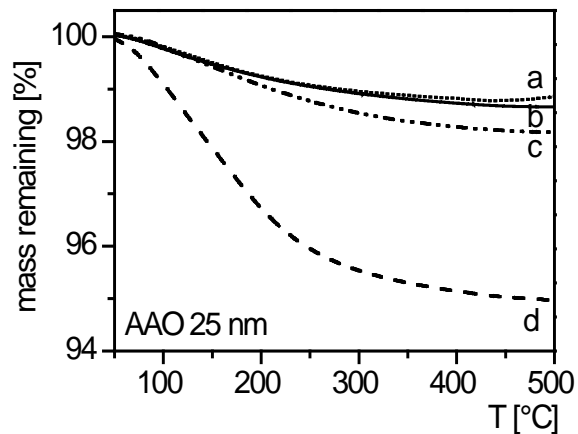


Figure 4.1: Thermo gravimetric analysis of AAO 25 nm, aluminum substrate is removed; (a) annealed at 400 °C for 2 h under vacuum, (b) annealed at 400 °C for 2 h under vacuum and water storage for 1 h, (c) annealed at 180 °C for 2 h under vacuum, (d) annealed at 180 °C for 2 h under vacuum and water storage for 1 h.

As can be seen in Figure 4.1, TG analysis of first sample annealed at 400 °C for 2 h (Figure 4.1 dotted line a) revealed a mass loss of around 1%. A second sample annealed at 400 °C for 2 h, and then placed in water for 1 h showed also a mass loss near 1% (Figure 4.1 solid line b). Last, an AAO membrane annealed at 180 °C for 2 h under vacuum (Figure 4.1 dashed-dotted line c) displayed a mass loss of ~2%. The same sample placed in water for 1 h after the annealing step at 180°C for 2 h, showed a mass loss of approximately 5% (Figure 4.1 dashed line d).

The results revealed that annealing at 180°C for 2 h under vacuum are sufficient parameters to remove physisorbed water from AAO membranes. The mass loss difference between 400 °C and 180 °C annealed samples is only 1%. The annealing temperature has an impact of the mass loss after water storage. AAO membranes which were annealed at 180 °C and afterwards placed in water showed a greater mass loss as AAO membranes annealed at 400 °C and also stored in water. The mass loss difference amounted to 4%. It can be supposed that the annealing temperature affected the possibility of AAO pore wall hydroxylation.

However, questions about the AAO pore wall chemistry (e.g., hydroxyl groups per area depending on the annealing temperatures) have not been studied. Actually, it is not clear which effect have higher temperatures (i.e., annealing at 400 °C) on the AAO pore wall chemistry. For example, during heating Brønsted acid centers might be reduced due to water loss, and Lewis acid or Lewis base centers are formed. These results might be an interesting starting point for deeper investigations.

4.2 Influence of AAO Preparation on EPR signals

AAO membranes (Table 4.1) for EPR^b measurements had pore diameters ranging from 20/25 nm to 180 nm. For AAO preparation procedures see Chapter 2.1. The aluminum substrate was etched away and some samples were chemically modified with ODPa. Such samples are referred to as sf-mod ODPa. The etching process and AAO surface

^b Universität Osnabrück, Fachbereich Physik, AK Steinhoff

modification are described in Chapter 3.1. Note samples, referred to as sf-mod without ODPA, were also treated like modified samples, but to the *n*-heptane/2-propanol mixture ODPA was not added.

Table 4.1: AAO membranes for EPR measurements

Sample number	AAO Membrane [nm]	Electrolyte (acid)	Comments
sample 1	25 + widened to 35	H ₂ SO ₄ + H ₃ PO ₄	/
sample 2	25 + widened to 35	H ₂ SO ₄ + H ₃ PO ₄	sf-mod without ODPA
sample 3	25 + widened to 35	H ₂ SO ₄ + H ₃ PO ₄	sf-mod ODPA
--			
sample 4	25 + widened to 35	H ₂ SO ₄ + C ₂ H ₂ O ₄	/
sample 5	25 + widened to 35	H ₂ SO ₄ + C ₂ H ₂ O ₄	sf-mod without ODPA
sample 6	25 + widened to 35	H ₂ SO ₄ + C ₂ H ₂ O ₄	sf-mod ODPA
--			
sample 7	25	H ₂ SO ₄	/
sample 8	25	H ₂ SO ₄	sf-mod without ODPA
sample 9	25	H ₂ SO ₄	sf-mod ODPA
--			
sample 10	35	C ₂ H ₂ O ₄	/
sample 11	35	C ₂ H ₂ O ₄	sf-mod without ODPA
sample 12	35	C ₂ H ₂ O ₄	sf-mod ODPA
--			
sample 13	60	C ₂ H ₂ O ₄	/
sample 14	60	C ₂ H ₂ O ₄	sf-mod without ODPA
sample 15	60	C ₂ H ₂ O ₄	sf-mod ODPA
--			
sample 16	180	H ₃ PO ₄	/
sample 17	180	H ₃ PO ₄	sf-mod without ODPA
sample 18	180	H ₃ PO ₄	sf-mod ODPA

As can be seen in Figure 4.2, AAO membranes prepared with oxalic acid showed a pronounced EPR signal. For example, AAO membranes with sample numbers 10 to 15 were in contact with oxalic acid approximately 3 days and clearly displayed the highest values. Lower EPR signals are detected for 25 nm AAO membranes (sample number 4 to 6) which were anodized with sulfuric acid and subsequently widened to ~35 nm with oxalic acid. The samples were in contact with oxalic acid only 1 h which may explain the lower EPR signals in Figure 4.2b.

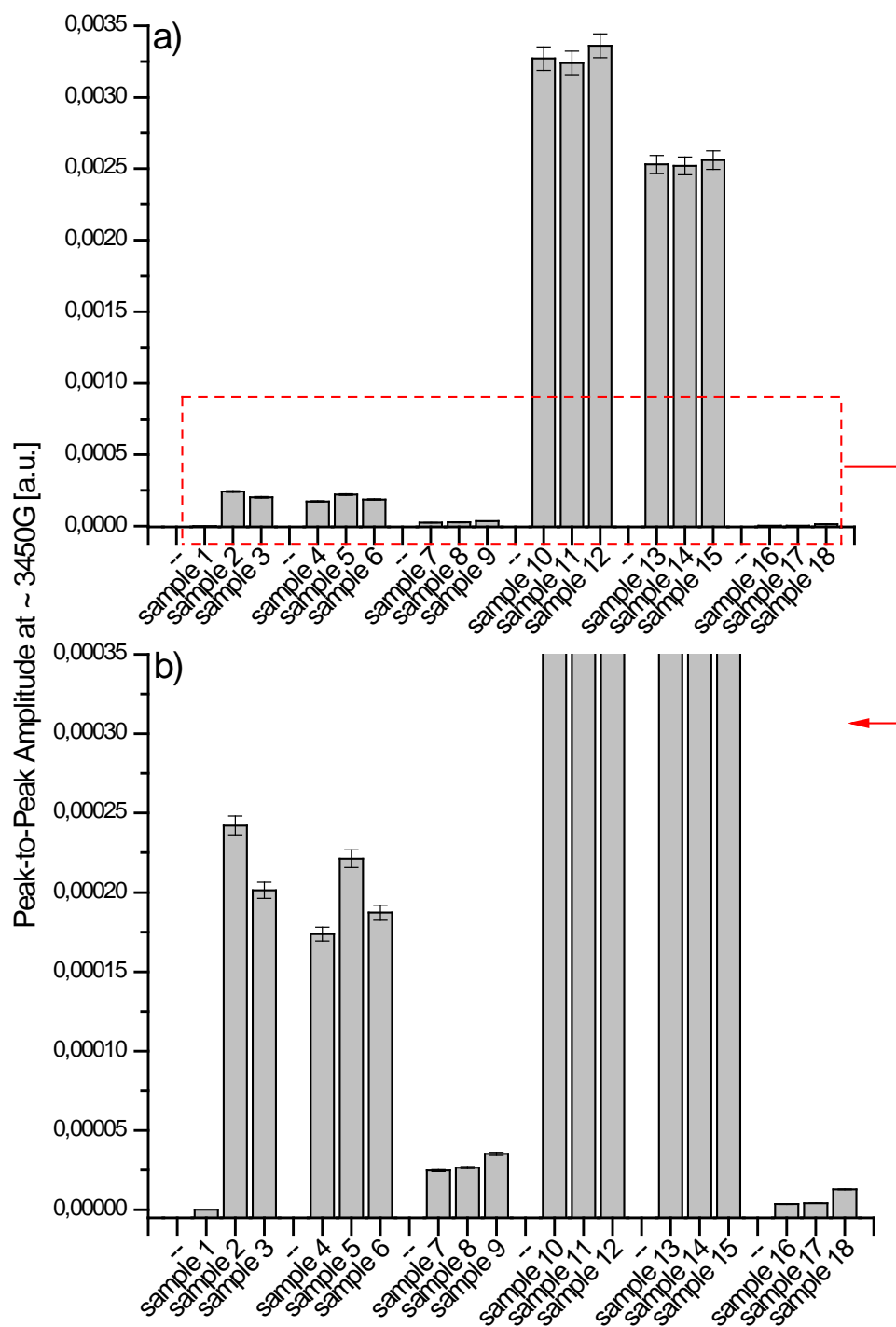


Figure 4.2: Peak-to-Peak amplitudes of EPR line at ~ 3450G (corrected for sample masses, amplitude/mg, error $\pm 2.5\%$); (a) AAO membranes pore sizes ranging from 20–180 nm, removal of the AAO aluminum substrate, (b) showed a zoomed range.

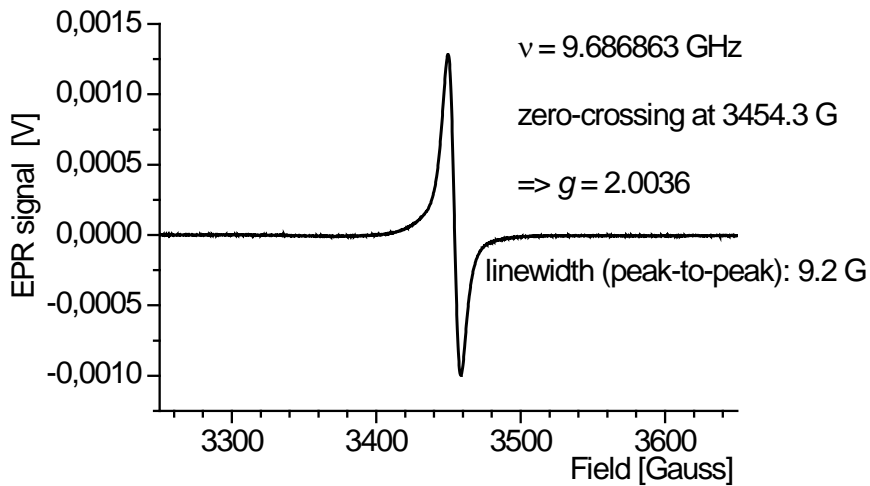


Figure 4.3: EPR spectra of 35 nm AAO surface-modified with ODPA (sample 12).

The recent investigation also revealed lower EPR signals for AAO membranes which had contact to inorganic acids like phosphoric or sulfuric acid. Further, EPR signals were not influenced by ODPA modification. The samples named as sf-mod with ODPA and sf-mod without ODPA showed no differences in their EPR signals.

In summary it could be said that AAO membranes which were in contact with oxalic acid presented a sharp signal in their EPR-spectra with a g -value of 2.0036 (Figure 4.3). The signal may be due to organic radicals present at the AAO pore wall surface.

5 Acetaminophen Confined to Nanoporous Matrices

Acetaminophen (ACE), a low-molecular model weight drug, was solidified in isolated, anisotropic AAO and in connected, isotropic CPG membranes. The influence of crystallization conditions on nucleation and crystal growth was investigated. A basic crystallization model is presented. Additionally, the AAO membranes were used as drug delivery carriers. In the second part acetaminophen was encapsulated in AAO membranes and drug release studies were performed. Resulting dissolution profiles were fitted to basic kinetic laws and to a mathematical model.

5.1 Influence of Crystallization Parameter on ACE in AAO Membranes

Acetaminophen confined in anisotropic AAO membranes was used to study the influence of crystallization parameters such as cooling rates, the presence or the absence of a bulk surface reservoir on nucleation and crystal growth kinetics. The compound was melt infiltrated and (i) quenched, or (ii) slowly cooled at a rate of -0.5 K/min. Additionally, the infiltrated acetaminophen was cooled (iii) in the presence or (iv) in the absence of a bulk surface reservoir. Preparation details can be found in Chapter 3.1. The used AAO membranes had (v) pore sizes of 60 nm and pore depths of ~ 100 μm . These five variations of the crystallization parameters will have an impact on the crystallization behavior of acetaminophen under confinement compared to its bulk counterpart. The material embedded in AAO was investigated with X-ray diffraction and DSC measurements.

5.1.1 ACE in 60 nm AAO Quenched in the Presence of Bulk Material

Quenched samples were prepared by rapid cooling from melt in the presence of a bulk acetaminophen surface reservoir. Before characterization the bulk surface film was carefully removed with a blade. The collected $\theta/2\theta$ pattern (Figure 5.1a) showed five significant peaks. The peaks were indexed according to reference found in the CSD deposition number CSD-HXACAN03⁶¹. Characteristic reflections of acetaminophen form I in AAO are the (-110) at $2\theta = 12.0^\circ$, the (200) at $2\theta = 15.2^\circ$, the (101) at $2\theta = 15.6^\circ$, the (-210) at $2\theta = 17.8^\circ$, and the (-220) at $2\theta = 24.4^\circ$. Literature and collected $\theta/2\theta$ data are listed in Table 5.1.

To measure orientation distributions of a set of lattice planes with respect to the AAO pore axis Schulz scans were performed. More details about Schulz scans can be found in Chapter 3.2.2. As can be seen in Figure 5.1, the scattering intensity profiles $I(\psi)$ yielded different maxima at certain ψ values. The Schulz scan corresponding to the (200) plane ($2\theta = 15.2^\circ$) showed a maximum at $\psi = 0^\circ$. The occurrence of $I(\psi)$ maximum at $\psi \sim 50^\circ$ for the (-220) reflection of acetaminophen form I ($2\theta \sim 24.4^\circ$) is in line with the theoretical angle of 51.1° between (200) and (-220). The same can be observed with the $I(\psi)$ maximum at $\psi \sim 53^\circ$ for the (101) reflection ($2\theta \sim 15.6^\circ$) of form I. The calculated angle between (200) and (101) is 53.4° . On the other hand, the angle between (200) and (111) ($2\theta \sim 18.1^\circ$) lattice planes of form I is 59.4° . The Schulz scan corresponding to the (111) plane revealed a maximum at $\psi \sim 45^\circ$. Further, the theoretical angle between the (-220) and (101) lattice planes is 68.0° . As can be seen, the difference between the maxima at $\psi \sim 20^\circ$ for (-220) and $\psi \sim 53^\circ$ for (101) is only 35° . Apparently, acetaminophen in 60 nm AAO membranes fast cooled from melt in the presence of a bulk surface reservoir showed several discrete populations of form I crystals with specific orientations.

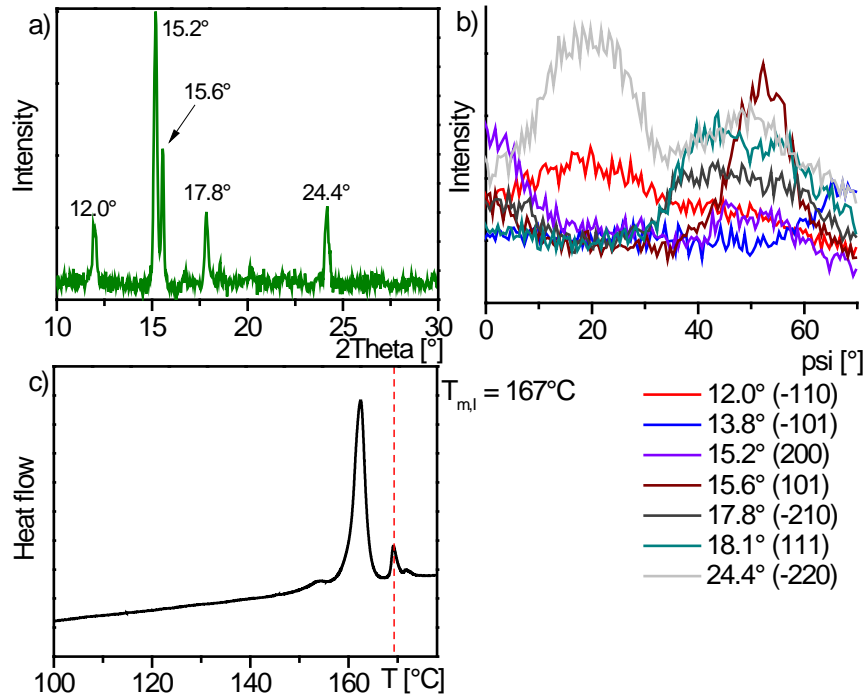


Figure 5.1: Acetaminophen in 60 nm AAO prepared at wetting temperature of 175 °C for 30 min, quenched in the presence of a bulk surface film and removal of the bulk surface reservoir. (a) $\theta/2\theta$ scan, (b) Schulz scan, (c) first DSC heating scan (10 K/min). The dotted red line corresponds to the bulk melting point of acetaminophen form I.

Table 5.1: $\theta/2\theta$ peaks of acetaminophen form I with the corresponding (*hkl*)-values taken from ref 61.

h	k	l	2Theta [°]	I [%] ⁶¹	2Theta [°]	I [%]
-1	1	0	12.114	29	12.0	21
-1	0	1	13.808	37	/	
2	0	0	15.227	47	15.2	100
1	0	1	15.517	71	15.6	50
-2	1	0	17.938	34	17.8	23
1	1	1	18.194	56	/	
-1	2	0	20.414	21	/	
-2	1	1	20.766	15	/	
2	1	1	23.071	16	/	

-1	2	1	23.491	59	/	
-2	2	0	24.374	100	24.4	29
-2/-3	2/1	1	26.531	77	/	

Occasionally, reflections emerged which do not belong to form I. Compared with literature data (more details in Chapter 5.1.2) the peaks were indexed according to acetaminophen form II and III. If such additional reflections are visible, the AAO membranes were re-heated to 148 °C for 2 h without bulk surface film under argon. This temperature is above the melting temperature of form II and III in AAO membranes with pore sizes of 60 nm.⁹ After the reheating process, the AAO membrane surface was cleaned and collected WAXS patterns showed the form I reflections as shown in Figure 5.1. DSC measurements supported the diffraction experiments. Acetaminophen in 60 nm AAO membranes quenched in the presence of bulk surface material melted near 159 °C (Figure 5.1c). The melting point was slightly below the bulk melting temperature of form I showed in Figure 5.1c with a dotted line. The small melting peak around 167 °C indicated an amount of bulk material on the AAO surface. The melting peak of form I was in line with results reported for acetaminophen in 60 nm AAO membranes⁹. The melting peaks of material under confinement show a melting point depression known as Gibbs–Thomson effect.^{21, 96} Hence, the melting points decrease when the pore size also decrease.

5.1.2 ACE in 60 nm AAO Cooled at 0.5 K/min in the Presence of Bulk Material

Infiltrated acetaminophen in 60 nm AAO membranes was allowed to cool down to 25 °C at a cooling rate of −0.5 K/min under argon in the presence of a bulk surface reservoir. The detailed descriptions are found in Section 3.1. Theta/2theta measurements of the bulk surface reservoir in Figure 5.2a displayed differently oriented form II crystallite populations. Directly after non-isothermal crystallization the samples were placed in the XRD device and the theta/2theta scan was taken in presence of the bulk

acetaminophen surface reservoir (Figure 5.2a). The bulk surface film was carefully removed and the samples were measured again. As seen in Figure 5.2b, the $\theta/2\theta$ pattern had different reflections compared with the form I sample shown in Figure 5.1. The peaks were indexed based on the CSD deposition number HXACAN23⁶³ and described as reflections belonging to acetaminophen form II. Approximately 40% of the collected $\theta/2\theta$ patterns had the two dominant peaks at $2\theta = 14.9^\circ$ and 30.1° with an intensity ratio of 1:0.4–0.3 listed in Table 5.2.

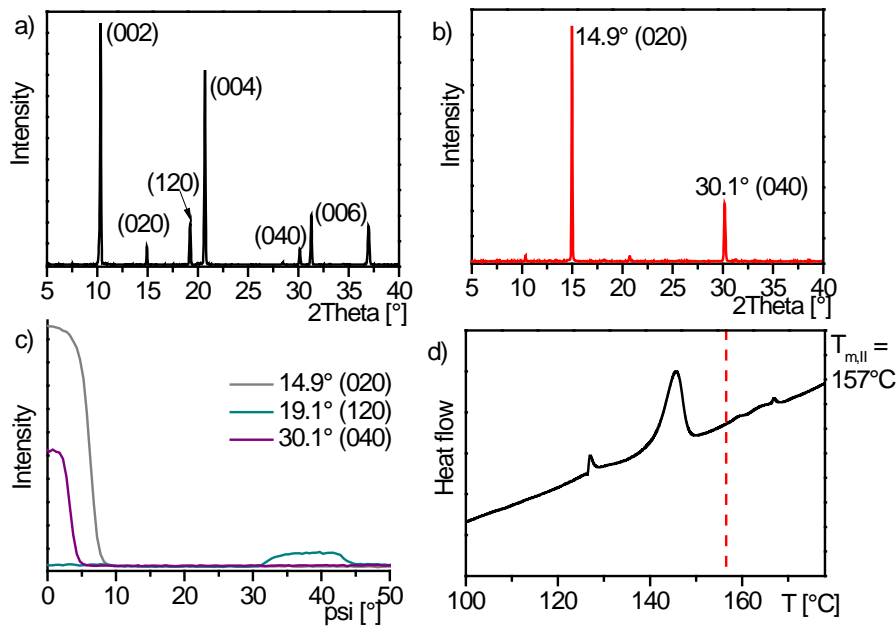


Figure 5.2: Acetaminophen in 60 nm AAO prepared at wetting temperature of 175°C for 30 min, cooled at -0.5 K/min in the presence of a bulk surface film; (a) $\theta/2\theta$ scan taken in the presence of a bulk surface film directly after non-isothermal crystallization, (b) $\theta/2\theta$ scan after removal of the bulk surface film (c) Schulz scan, (d) first DSC heating scan (10 K/min). The dotted line corresponds to the bulk melting point of acetaminophen form II.

Table 5.2: $\theta/2\theta$ peaks of acetaminophen form II with the corresponding (hkl) -values taken from ref 63.

h	k	l	2Theta [°]	I [%] ⁶³	2Theta [°]	I [%]
0	0	2	10.301	3.4	10.3	2
0	1	2	12.731	4.1	/	

0	2	0	14.957	12.2	14.9	100
1	1	1	15.014	0.3	/	
1	1	2	17.489	18.0	/	
0	2	2	18.194	13.7	/	
1	2	0	19.181	28.1	/	
0	0	4	20.685	3.9	20.6	1
...						
2	0	0	24.014	100	/	
...						
1	3	3	30.018	0.8	/	
0	4	0	30.176	1.3	30.1	38
2	2	2	30.294	20.2	/	
0	0	6	31.246	1.1	31.2	0.5

The $I(\psi)$ profiles in Figure 5.2c corresponded to the (020) reflection at $2\theta = 14.9^\circ$ and to the (040) reflection at $2\theta = 30.1^\circ$, respectively. The $I(\psi)$ profiles of both reflections showed pronounced maxima at $\psi = 0^\circ$. The narrow maxima around $\psi \sim 0^\circ$ indicated that the (020)/(040) lattice planes are oriented parallel to the AAO surface. The Hermans' order parameter f^{91} of the (020) and (040) lattice planes amounted to ~ 0.97 . The $I(\psi)$ profile maximum at $\psi \sim 39^\circ$ for the (120) reflection corresponded to the theoretical angle of 38.6° between the (0k0) and (120) lattice planes. It can be concluded that all reflections belong to one crystal population.

As seen in the DSC heating scan in Figure 5.2d, acetaminophen in AAO membranes with pore sizes of 60 nm and cooled at a rate of -0.5 K/min in the presence of a bulk surface film showed two melting peaks. The first appeared at $T_{\text{onset}} = 133^\circ\text{C}$ and may belong to the melting point of form III (bulk $\sim 143^\circ\text{C}$). Form III is a metastable crystal form only produced under confinement.^{7, 64, 98} A second peak appeared at 144°C (T_{onset}) clearly near the bulk melting point of form II. The same sample annealed at 135°C for 2 h revealed a small melting point at 127°C and a melting peak at 141°C of form II. For clearness the bulk melting point of acetaminophen form II ($T_{\text{m,II}} \sim 157^\circ\text{C}$) is shown in Figure 5.2d.

Directly after non-isothermal crystallization of acetaminophen in 60 nm AAO membranes cooled at -0.5 K/min in the presence of a bulk surface reservoir the samples

showed intense form II (020) and (040) reflections. Sometimes, the form III reflections dominated inside the AAO nanopores. Such samples had a main reflection at $2\theta = 30.1^\circ$ with smaller peaks at 10.3° , 12.7° or 18.1° , respectively. The collected pattern showed a good agreement with acetaminophen form III. Form III data are stored in the CSD with deposition number HXACAN29 based on reference 65. Note powder patterns of form I do not show significant reflections at $2\theta \sim 30^\circ$, and powder pattern of form III do not have significant reflections at $2\theta \sim 15^\circ$. To remove traces of form III, the samples were heated at 135°C for 2 h under argon.

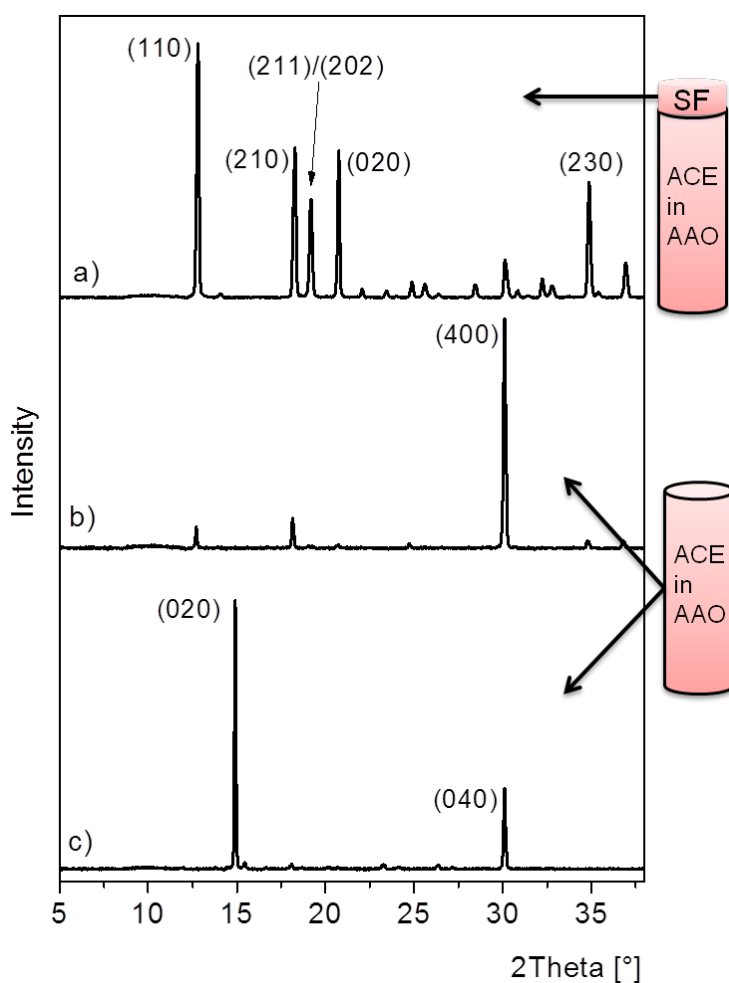


Figure 5.3: Acetaminophen in 60 nm AAO cooled at a rate of -0.5 K/min in the presence of a bulk surface film (SF). (a) $\theta/2\theta$ scan taken in the presence of a bulk surface film directly after non-isothermal crystallization, (b) $\theta/2\theta$ scans after removal of the bulk surface film, (c) $\theta/2\theta$ scan after removal of the bulk surface film and annealing at 135°C for 2 h.

Several form III reflections originating from crystals in the bulk surface film can be seen in Figure 5.3a. After removal of the bulk surface material, the pattern is dominated by a strong reflection at $2\theta = 30.1^\circ$ (Figure 5.3b). Annealing at 135°C for 2 h without bulk surface film converted form III crystals into form II crystals indicated by the appearance of strong reflections at $2\theta = 14.9^\circ$ and 30.1° , respectively (Figure 5.3c). At this temperature form III melts in 60 nm AAO membranes according to the estimated melting point in reference 9.

In general, acetaminophen in AAO membranes with pore sizes of 60 nm and cooled at -0.5 K/min in the presence of a bulk surface reservoir yielded highly oriented form II and/or form III crystals. These results will be discussed in Chapter 5.5.1.

5.1.3 Amorphous ACE in 60 nm AAO Membranes

A former study²² shows that crystallization of acetaminophen is completely suppressed in CPG membranes with pore sizes of 4.6 nm. Based on these reports, acetaminophen in 60 nm AAO membranes was quenched or cooled at a rate of -0.5 K/min in the absence of a bulk surface reservoir. Independently from the cooling rates the confined material displayed no reflection during the $\theta/2\theta$ scan (Figure 5.4).

First DSC heating scans in Figure 5.4b showed a small melting peak at $T_{\text{onset}} = 152^\circ\text{C}$. It might be assumed that the material inside AAO pores is not fully amorphous and small volume fractions could be crystalline. DSC measurements involved the removal of the aluminum substrate. During the etching process the AAO membrane was slightly heated up which may influence the possibility for crystallization.

Amorphous samples stored for a certain time period under ambient conditions revealed crystalline structures. For example, an amorphous AAO sample showed reflection of acetaminophen form I after 9 month storage (Figure 5.4c). Schulz scans (Figure 5.4d) revealed the coexistence of several populations of form I crystals with different orientations. This result is in line with acetaminophen form I in 60 nm AAO membranes as shown in Chapter 5.1.1.

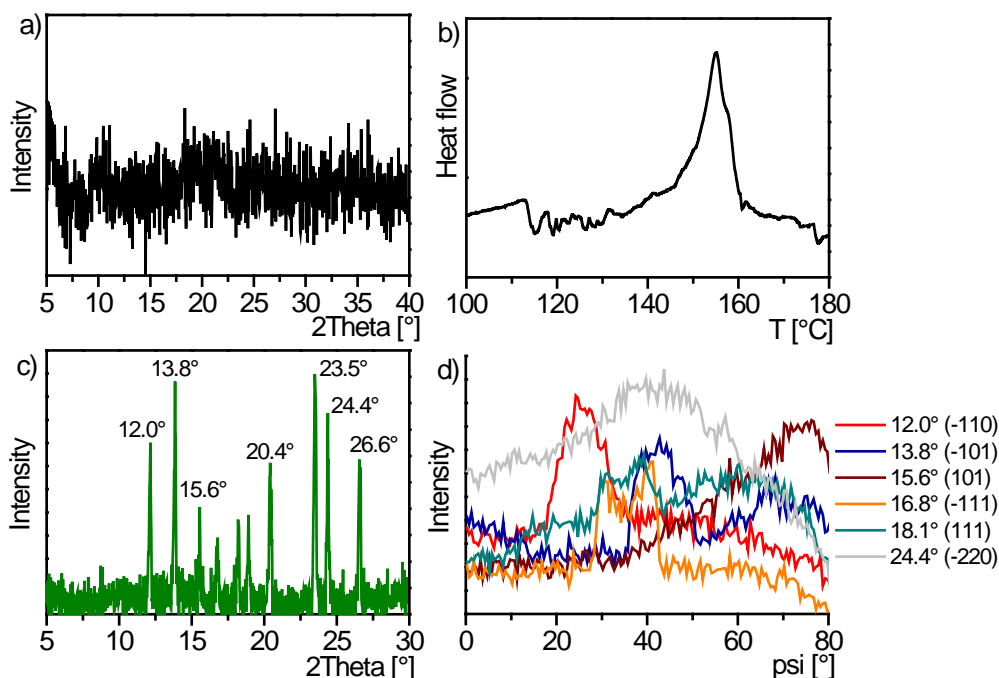


Figure 5.4: Acetaminophen in 60 nm AAO prepared at wetting temperature of 175 °C for 30 min, quenched without contact to bulk surface reservoir (a) $\theta/2\theta$ scan, (b) first DSC heating scan (10 K/min). (c) $\theta/2\theta$ scan and (d) Schulz scan of the sample stored 9 month under ambient conditions.

5.2 Isothermal Crystallization of ACE in AAO 60 nm

Isothermal or cold crystallization (CC) were performed based on the research done by Rangarajan and co-workers with acetaminophen^{7, 21, 22} confined in CPG membranes. Acetaminophen shows a glass transition step at $T_g \sim 24$ °C and cold crystallized around 60–90 °C⁹⁹. In this study amorphous acetaminophen in anisotropic AAO membranes was heated up at a temperature between 80–90 °C and stored there for a certain time period. During the cold crystallization the samples had contact or had no contact to a bulk acetaminophen surface reservoir. The investigation will give an answer how affect the thermal history (i.e., isothermal or non-isothermal crystallization) the nucleation and crystal growth process.

Firstly, an amorphous sample, preparation details are given in Section 5.1.3, was mounted in the XRD device. The first theta/2theta scan was collected at 25 °C, then the XRD device stepped up to the next temperature, held constantly for 1 h before a new theta/2theta scan started. As can be seen in Figure 5.5, no reflections were visible below 70 °C. The first crystalline 2 θ peak occurred at 75 °C. Apparently, with temperature increasing acetaminophen became crystalline. At 115 °C, the reflections at 2 θ = 14.9° and 30.1° indicated acetaminophen form II⁶³.

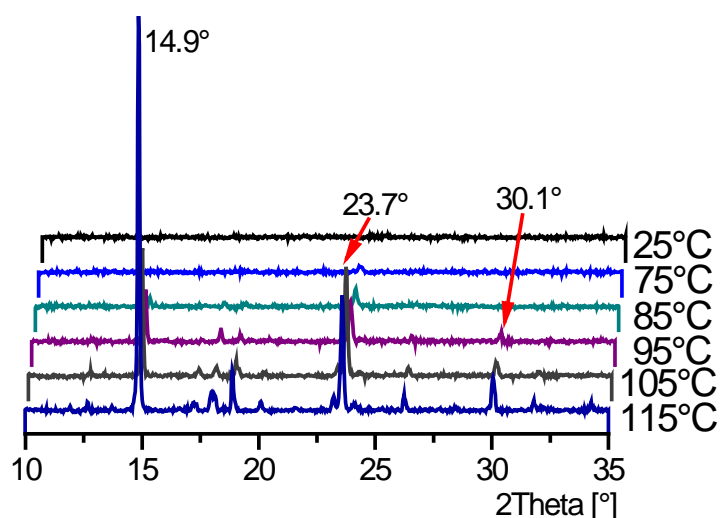


Figure 5.5: $\theta/2\theta$ temperature-dependent scans of amorphous acetaminophen in 60 nm AAO, mounted in the XRD device.

In a second step, acetaminophen infiltrated in AAO was cold crystallized in the absence of a bulk surface reservoir. During cold crystallization the amorphous samples were placed in the furnace under argon. After cold crystallization such samples showed only weak theta/2theta reflections. For example, acetaminophen cold crystallized at 90 °C for 4 days without bulk surface material revealed a weak 2 θ peak at 14.9° (Figure 5.6). Further, the sample showed a wide halo around 2 θ = 22° indicating amorphous volume fractions inside the pores. It might be suggested that crystallization occurs inside the AAO nanopores, but on a very slow time scale.

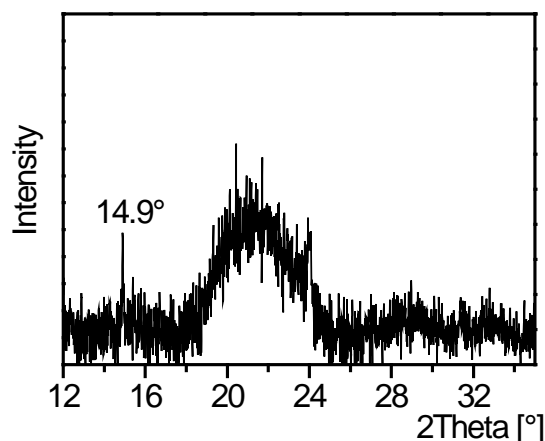


Figure 5.6: Acetaminophen in 60 nm AAO cold crystallized at 90 °C for 4 days in the absence of a bulk surface reservoir. Note the y-axis is logarithmic.

Finally, to study the effects of bulk surface material on the possibility of crystallization, amorphous samples were cold crystallized in the presence of a bulk acetaminophen surface film. Re-heated samples were fast transferred in the furnace and stored there at 80 °C for 2 h under argon. Previous to WAXS measurements the bulk surface film was carefully removed with a blade, and then the aluminum substrate was etched away. More detailed preparation steps are described in Chapter 3.1. Collected theta/2theta patterns showed a dominant reflection at $2\theta = 30.1^\circ$ and a weaker at 14.9° , respectively (WAXS not shown). Based on results from Chapter 5.1.2, a sample was re-heated at 135 °C for 2 h under argon without bulk surface film to remove any traces of acetaminophen form III. After annealing, the theta/2theta pattern in Figure 5.7 revealed two peaks at $2\theta = 14.9^\circ(020)$ and $2\theta = 30.1^\circ(040)$ belonging to acetaminophen form II. The relative peak intensity ratio amounted to 1:0.3. Schulz scans of both reflections in Figure 5.7b showed pronounced maxima at $\psi = 0^\circ$ indicating lattice planes orientation normal to the AAO pore axis. Further, the $I(\psi)$ profile for the $2\theta = 19.1^\circ(120)$ reflection displayed a maximum around 39° . This corresponds with the theoretical angle of 38.6° between the form II (020) and (120) lattice planes. First DSC heating scans (Figure 5.7c) revealed a small endothermic peak at $T_{\text{lonset}} = 144^\circ\text{C}$ belonging to form II and a larger peak at 160°C (T_{2onset}) belonging to form I, respectively. The results correspond

to the expected melting temperatures for acetaminophen form I and form II in AAO membranes with pore sizes of 60 nm⁹.

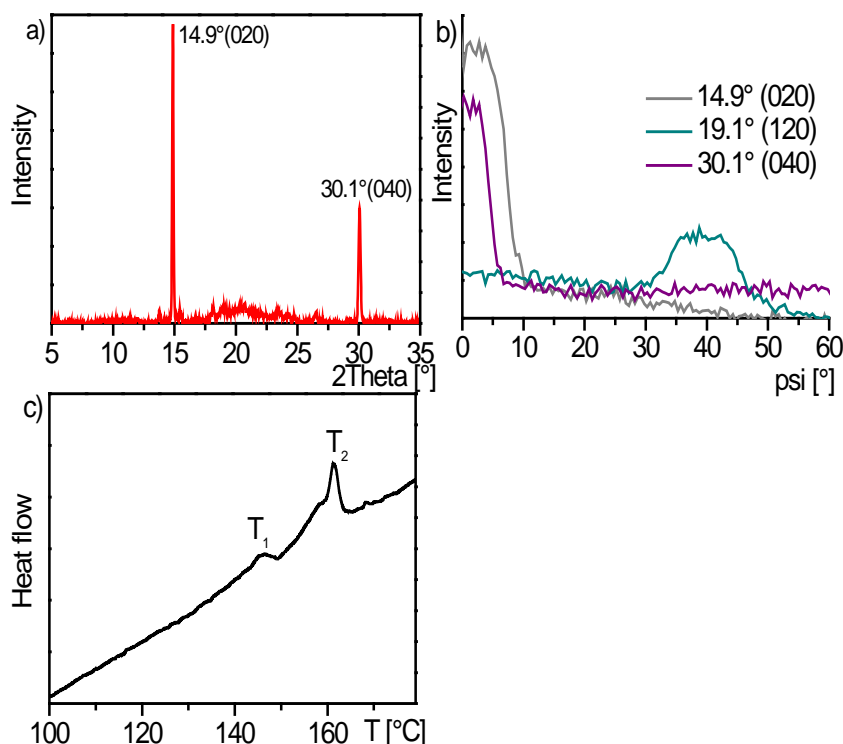


Figure 5.7: Acetaminophen in 60 nm AAO cold crystallized at 80 °C for 2 h in the presence of a bulk surface film, removal of the bulk surface material, and annealing at 135 °C for 2 h; (a) $\theta/2\theta$ scan, (b) Schulz scan, (c) first DSC heating scan (10 K/min).

5.3 ACE in Controlled Porous Glasses (CPG)

Confined acetaminophen in AAO membranes revealed that the crystallization system is sensitive to changes in the crystallization conditions. Moreover, different crystallization conditions offer new ways to stabilize crystal forms which are inaccessible in bulk material. However, the crystallization experiments were done in cylindrical, isolated pores. To change the pore morphology a second host matrix with connected nanopores has been selected. Acetaminophen was infiltrated in 60 nm CPG membranes on a hot-stage at 180 °C for 2 min, the samples details are given in Chapter 3.1. The hot CPG membranes were placed in the furnace, and (i) quenched, or (ii) cooled at a rate of

–0.5 K/min, (iii) in the presence or (iv) in absence of a bulk surface reservoir. WAXS and DSC results are shown in Figure 5.8.

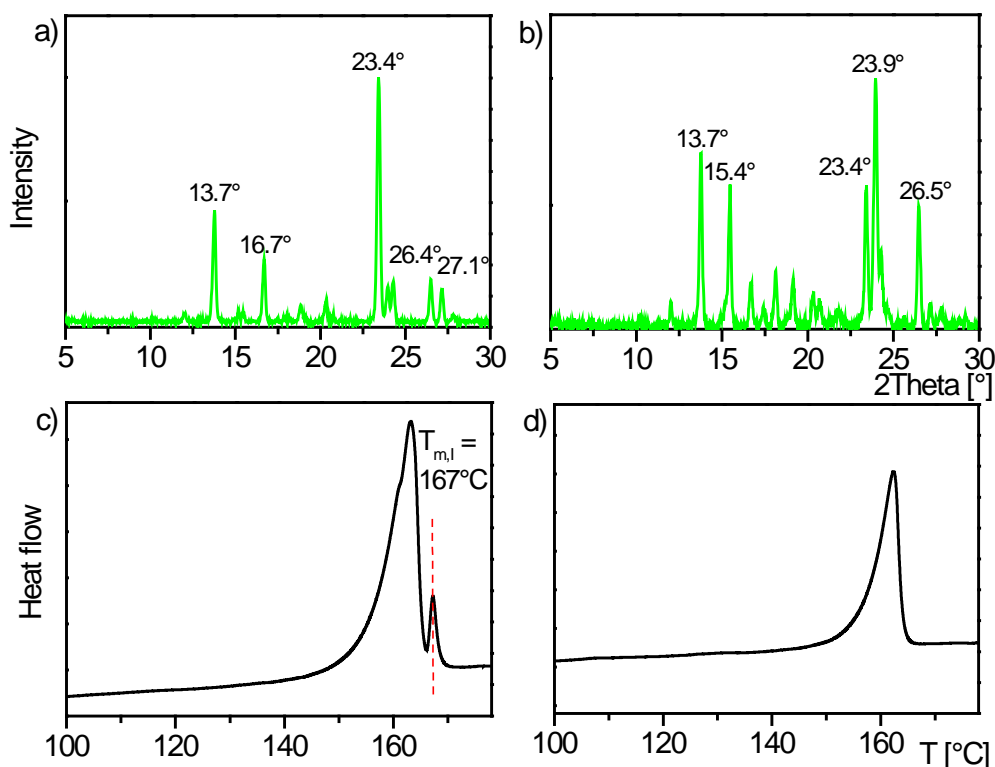


Figure 5.8: Acetaminophen in 60 nm CPG prepared at wetting temperature of 180 °C for 2 min; (a) quenched in the presence of a bulk surface film, removal of the latter, (b) quenched in the absence of a bulk surface film, (c) DSC first heating scan (10 K/min) of sample a, (d) DSC first heating scan (10 K/min) of sample b. Note the broad halo originated by the porous glass matrix is subtracted.

Acetaminophen in CPG quenched in the presence of a bulk surface reservoir (Figure 5.8a,c) showed a good agreement with the polymorphic form I⁶¹ in both; theta/2theta pattern and in the melting point at ~156°C. Samples quenched from melt without contact to a bulk surface reservoir yielded the same results (Figure 5.8b,d). The second peak at 167 °C in Figure 5.8c indicated small bulk material on the CPG surface.

An open question is, regarding the access to a bulk surface reservoir in combination with a slow cooling rate the crystallization kinetics in the CPG membranes. Acetaminophen in anisotropic AAO membranes crystallized at a cooling rate of

–0.5 K/min in presence of bulk surface reservoir showed uniaxial oriented form II/III crystals. Under identical crystallization conditions acetaminophen in CPG displayed different relative peak intensity profiles (Figure 5.9). The results revealed that in CPG membranes a network of larger crystals grew with random orientation. Further, the WAXS data showed the best agreement with acetaminophen form I. Occasionally, reflections of form II and/or form III occurred inside the CPG membranes.

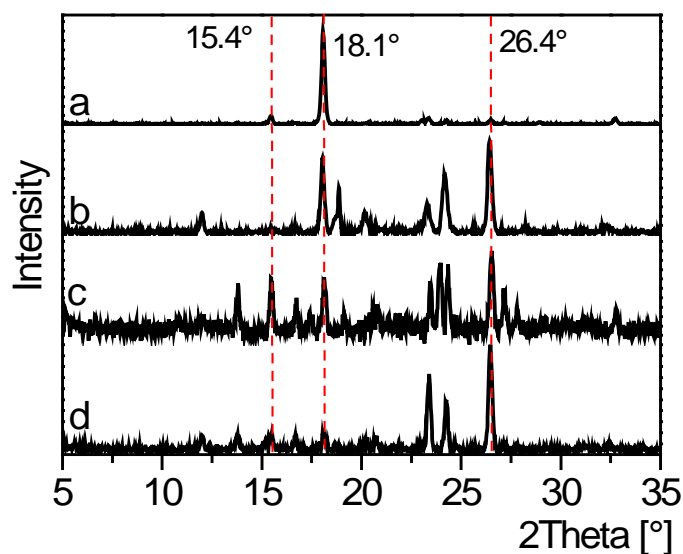


Figure 5.9: $\theta/2\theta$ scans of acetaminophen in 60 nm CPG prepared at wetting temperature of 180 °C for 2 min; (a) and (b) cooled at –0.5 K/min in the presence of a bulk surface film, (c) and (d) cooled at –0.5 K/min in the absence of a bulk surface film.

5.4 ACE in AAO with Pore Sizes Ranging from 25 to 400 nm

Acetaminophen in 60 nm AAO membranes cooled at a rate of –0.5 K/min or cold crystallized in the presence of a bulk surface reservoir yielded form III crystals. The crystals undergo a solid/solid transition to acetaminophen form II crystals. In the forthcoming chapter infiltrated acetaminophen was crystallized under the same crystallization conditions in AAO membranes with pore sizes ranging from 25 nm to

400 nm. The increase of surface-to-volume ratio due to the decrease of pore size may affect the crystallization kinetics

5.4.1 Non-Isothermal Crystallization

Infiltrated acetaminophen AAO samples were cooled at a rate of -0.5 K/min in the presence of a bulk surface reservoir. Previous to WAXS measurements the bulk surface material was scrapped off. The following theta/2theta patterns show one sample set of acetaminophen in AAO membranes with pore sizes of 25, 60, 100, 180 and 400 nm, respectively.

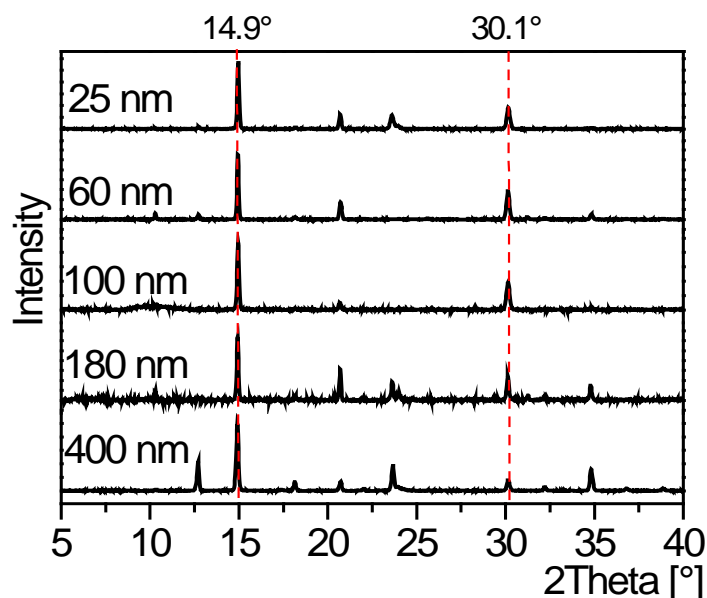


Figure 5.10: $\theta/2\theta$ scans of acetaminophen form II in AAO 25–400 nm prepared at wetting temperature of 175°C for 30 min, cooled at -0.5 K/min in the presence of a bulk surface film. Before WAXS measurements the bulk surface film was removed.

As can be seen in Figure 5.10, all WAXS patterns are dominated by two reflections at $2\theta = 14.9^\circ(020)$ and $30.1^\circ(040)$ indicating acetaminophen form II. A more interesting fact offers a second sample set. The WAXS patterns showed only one intense reflection

at $2\theta = 30.1^\circ$. The 2θ peak at 14.9° was not observed. Instead, the samples revealed weaker reflections at $2\theta = 12.7^\circ$, 18.1° or 20.6° , respectively (Figure 5.11). It can be assumed that the main peak at $2\theta = 30.1^\circ$ corresponded to the (400) lattice planes of form III.⁶⁵ As previously mentioned, form III shows no significant reflection at $2\theta \sim 15^\circ$. The appearance of the 14.9° reflection and the estimation of the relative intensities ratio of the (020) and (040) peaks provide the opportunity to distinguish between acetaminophen form II and form III in AAO membranes.

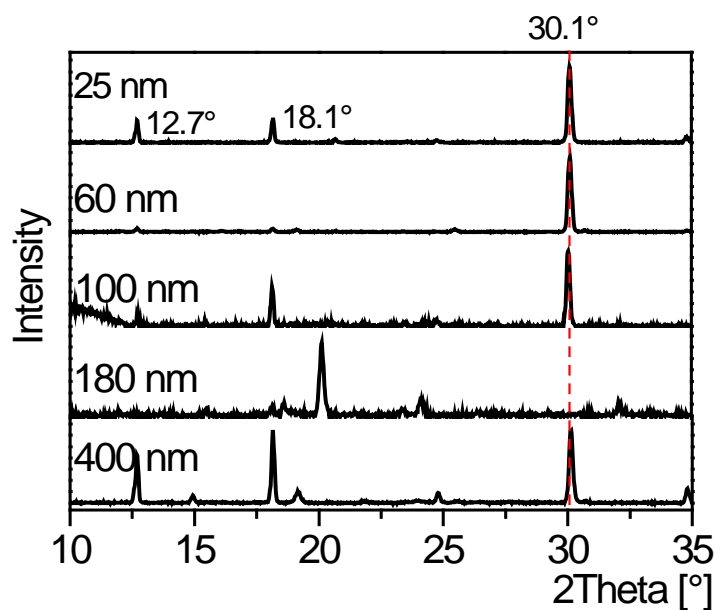


Figure 5.11: $\theta/2\theta$ scans of acetaminophen form III in AAO 25–400 nm prepared at wetting temperature 175°C for 30 min, cooled at -0.5 K/min in the presence of a bulk surface film. Before WAXS measurements the bulk surface film is removed.

For orientation distribution measurements Schulz scans were carried out. Firstly, the $I(\psi)$ profiles corresponding to the 30.1° reflection showed narrow maxima at $\psi \sim 0^\circ$ in all AAO samples (Figure 5.12). Secondly, the $I(\psi)$ profile belonging to the $2\theta = 19.1^\circ$ reflection exhibited a maximum at $\psi \sim 40^\circ$. The reflection could be indexed as acetaminophen form III (211) or (202)⁶⁵ lattice planes. But in both cases, the theoretical angle between the (400) and these two planes is 38.6° . In the last step, acetaminophen form III in AAO membranes was annealed above the form III melting point

corresponding to the AAO pore sizes.⁹ The annealing step converted form III crystals to form II crystals. The transition was only observed in 60 nm AAO samples where acetaminophen was annealed at 135°C for 1 h or in 25 nm AAO where acetaminophen was annealed at 120°C for 1 h under argon. After annealing, the form I crystals dominated inside the AAO membranes with pore sizes larger than 100 nm (WAXS not shown).

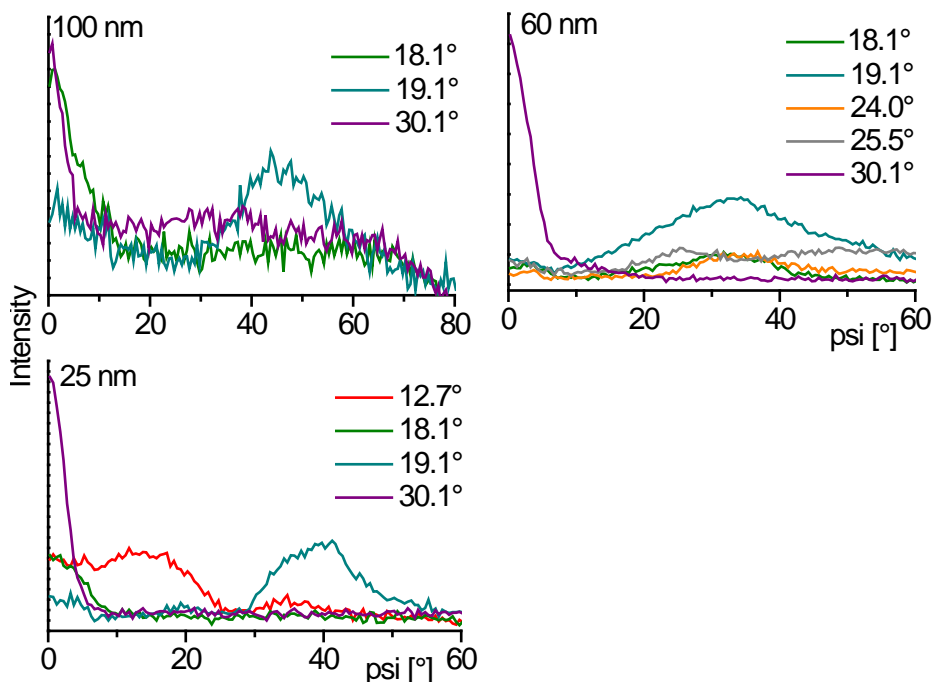


Figure 5.12: Schulz scans of acetaminophen form III in AAO 100 nm, 60 nm, and 25 nm prepared at wetting temperature of 175 °C for 30 min, cooled at -0.5 K/min in the presence of a bulk surface reservoir.

Texture analysis of acetaminophen in larger pores ($d = 400$ nm) also revealed a preferred crystal growth direction aligned to the AAO pore axis (Figure 5.13). The $I(\psi)$ profile corresponding to the 30.1° reflection showed a pronounced maximum at $\psi \sim 0^\circ$, indicating that the form III (400) lattice planes are oriented normal to the AAO pore axis. In 400 nm AAO membranes this crystallite orientation did not dominate inside the pores. It is not clear which crystal form(s) was observed. Note in Figure 5.13 the reflections were indexed based on acetaminophen form III.

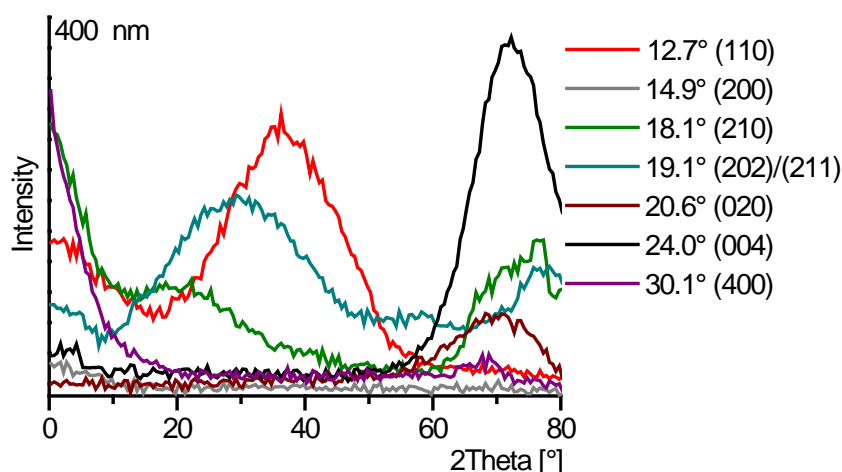


Figure 5.13: Schulz scans of acetaminophen form III in 400 nm AAO prepared at wetting temperature of 175 °C for 30 min, cooled at -0.5 K/min in the presence of a bulk surface reservoir.

For example, the theoretical angle between the form III (400) and (110) ($2\theta \sim 12.7^\circ$) lattice planes is 54.1° . The Schulz scan corresponding to the (110) crystal planes displayed a maximum at $\psi \sim 38^\circ$. It can be concluded that different polymorphic forms occur inside 400 nm AAO membranes.

However, the results revealed that acetaminophen cooled with -0.5 K/min in the presence of a bulk surface reservoir showed uniaxial form II and/or form III crystals in AAO membranes smaller than 100 nm. Both forms had a preferred crystal growth direction aligned with the AAO pore axis.

For example, acetaminophen in 25 nm AAO cooled at a rate of -0.5 K/min in the presence of a bulk surface reservoir yielded form II or form III crystals indicated by the occurrence of the 2θ form II reflection at $14.9^\circ(020)$ and 30.1° or only the 2θ form III reflection at $30.1^\circ(400)$. But both forms grew with crystal faces oriented normal to the AAO pore axis, as apparent from narrow $I(\psi)$ maxima at $\psi \sim 0^\circ$ for the form II reflection at $2\theta = 14.9^\circ$ and $2\theta = 30.1^\circ$, and for the form III reflection at $2\theta = 30.1^\circ$, respectively (Figure 5.14). Acetaminophen form III crystals can be converted in form II crystals.

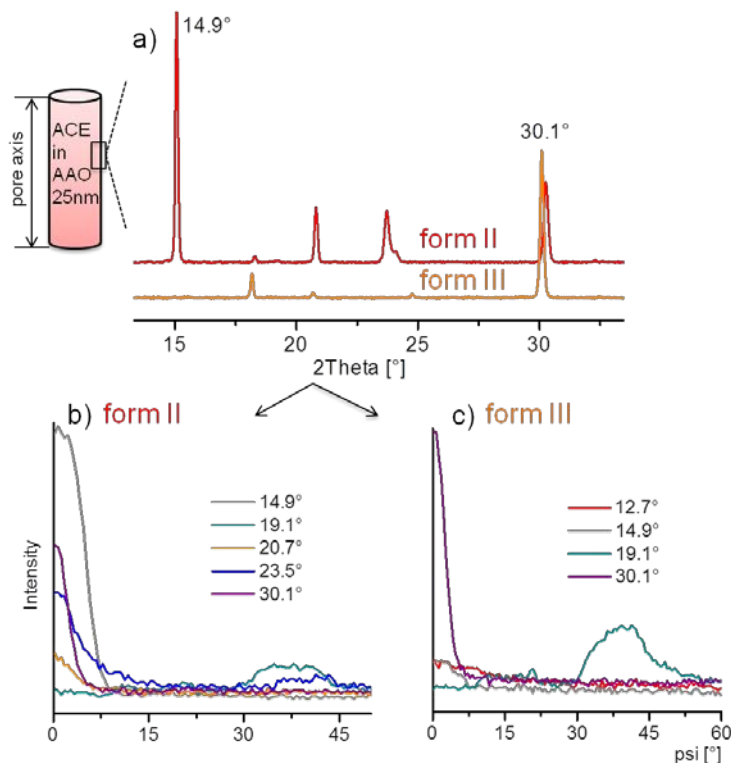


Figure 5.14: Acetaminophen in 25 nm AAO prepared at wetting temperature of 175 °C for 30 min, cooled at -0.5 K/min in the presence of a bulk surface reservoir, removal of the latter. (a) $\theta/2\theta$ scans of form II and III, (b) Schulz scans of form II, (c) Schulz scans of form III.

5.4.2 Cold Crystallization (Isothermal Crystallization)

Firstly, cold crystallization (CC) of acetaminophen in 60 nm AAO membranes revealed that the access to a bulk surface reservoir influenced the stability of amorphous forms (see Chapter 5.1.3). Secondly, acetaminophen in CPG membranes cold crystallized at 80 °C for 2 h in absence of bulk surface reservoir yields form III⁹ crystals. Acetaminophen in AAO membranes was cold crystallized based on those two results. Actually, there is still an open question how the AAO pore sizes affected the crystallization behavior of acetaminophen during cold crystallization. For this purpose, two samples sets were investigated:

CASE A: cold crystallization in the presence of a bulk surface reservoir

The infiltrated AAO membranes were re-heated to 180 °C for 2 min on a hot-stage with molten material on it. The samples were quenched below 0 °C, stored below −10 °C for 10 min, then re-heated and quenched again. After 3 times the samples were fast transferred in the furnace and re-heated to 80 °C for 2 h under argon. The surface material was removed before WAXS measurements.

CASE B: cold crystallization in the absence of a bulk surface reservoir

The non-isothermal steps were carried out in the same sequence. Except that the samples had no contact to excess bulk acetaminophen surface material.

Figure 5.15 shows the theta/2theta patterns of the cold crystallized samples in the presence of a bulk surface reservoir. In 25 nm AAO the single peak at $2\theta = 30.1^\circ$ indicated acetaminophen form III and in 60 nm AAO membranes the 14.9° reflection revealed the polymorphic form II but with traces of form III. The same sample annealed at 135 °C for 2 h showed exclusively the (020) and (040) reflections indicating uniformly oriented form II crystals (see Chapter 5.1.2 Figure 5.2).

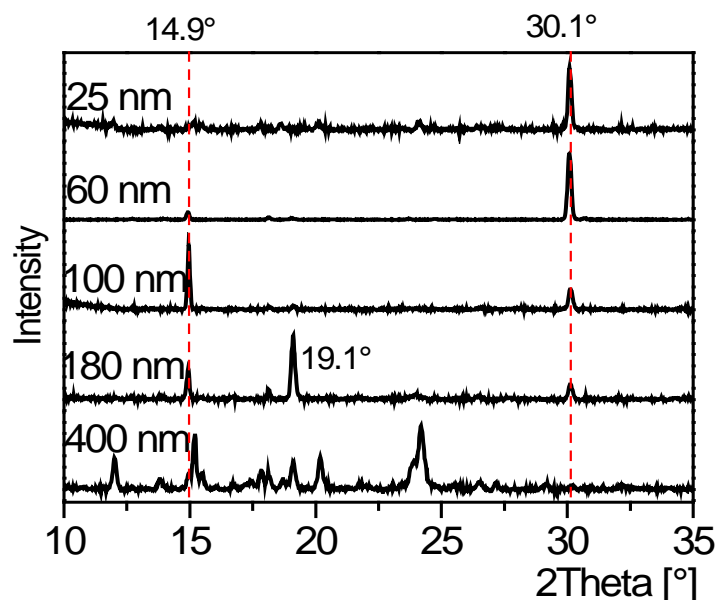


Figure 5.15: CASE A: $\theta/2\theta$ scans of acetaminophen in AAO 25–400 nm cold crystallized at 80 °C for 2 h in the presence of a bulk surface reservoir, measured after removal of the bulk surface material.

In 100 nm AAO membranes the ratio of the relative intensities of the (020) and (040) reflections is 1:0.3. This is in line with results of acetaminophen form II in 60 nm AAO. On the other hand, it is not really clear which polymorphic forms occurred in 180 nm or 400 nm AAO membranes. Mixtures of forms II and III with traces of form I may grow inside the nanopores.

Schulz scans belonging to the 2θ peak at 30.1° of acetaminophen in 25 nm, 60 nm, and 100 nm (Figure 5.16) showed pronounced maxima at $\psi \sim 0^\circ$. In 25 nm AAO membranes, the reflection corresponded to the form III (400) lattice planes. In 60 nm AAO, the $I(\psi)$ profile corresponding to $2\theta = 30.1^\circ$ (purple line) showed a higher intensity than the intensity profile of the 14.9° reflection (gray line) at $\psi = 0^\circ$. It can be assumed that the nanopores contain a mixture of form II and III crystals. In 100 nm AAO membranes, the (020) reflection revealed a higher maximum at $\psi \sim 0^\circ$ as the (040) reflection (purple line). The changed intensity ratio may indicate more form II crystals inside the pores.

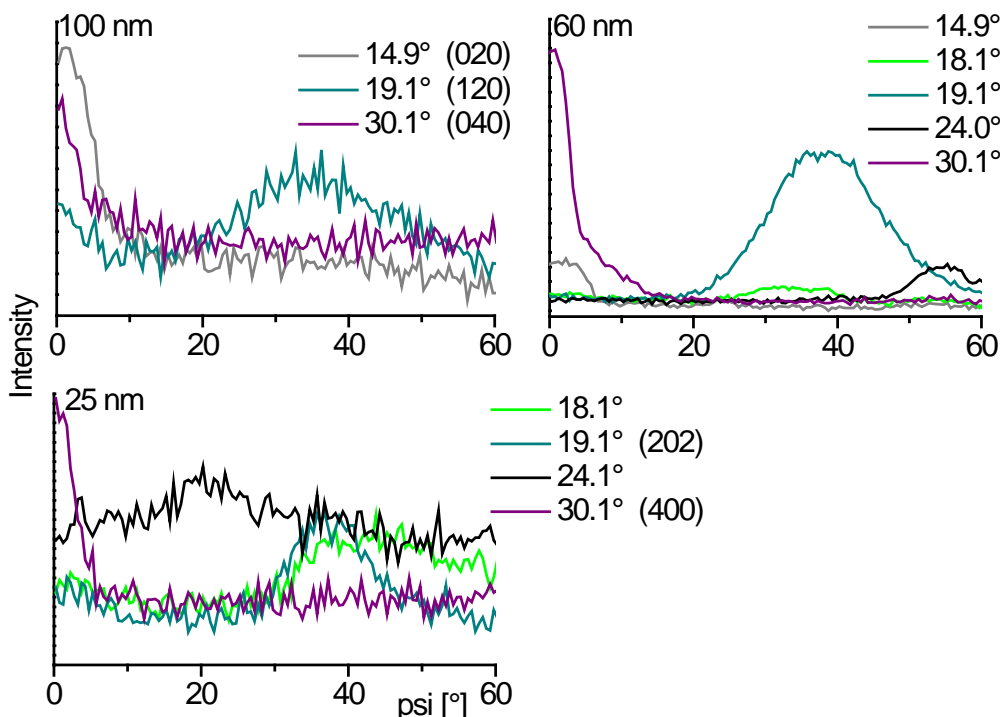


Figure 5.16: Schulz scans of acetaminophen in AAO membranes cold crystallized at 80°C for 2 h in the presence of a bulk surface reservoir, measured after removal of the bulk surface material.

Acetaminophen in AAO membranes non-isothermally crystallized (Figure 5.12) or cold crystallized (Figure 5.16) in the presence of a bulk surface reservoir revealed not a clear relationship between the AAO pore sizes (i.e., surface-to-volume ratio) and the orientation distribution inside the pores. The estimated Hermans' order parameter of the 30.1° reflection (Table 5.3) amounted between ~ 0.70 and ~ 0.90 . The parameter showed no influence on the orientation distribution depending on the pore size or the crystallization conditions.

Table 5.3: Hermans' order parameter for acetaminophen in AAO membranes non-isothermal and cold crystallized.

AAO Membrane [nm]	Crystallization conditions	Hermans' Order Parameter f $2\theta = 30.1^\circ$
25	cooled at -0.5 K/min	0.87
60	in the presence of a	0.92
100	bulk surface reservoir	0.71
400		0.84
25	cold crystallized	0.61
60	at 80°C for 2 h in the presence of a	0.91
100	bulk surface reservoir	0.69

In the second part, amorphous acetaminophen in AAO membranes with pore sizes ranging from 25 nm to 400 nm was cold crystallized in the absence of a bulk surface reservoir. Collected WAXS patterns showed no reflection for acetaminophen in AAO membranes with pore sizes smaller than 100 nm. Reflections only occurred in pores larger than 180 nm. The main peak was visible at $2\theta \sim 24.0^\circ$ and might belong to form III (WAXS not shown).

The cold crystallization results are summarized in Figure 5.17. The results revealed that the crystallization parameters such as the pore size or the bulk surface material had an influence on the occurrence of acetaminophen modifications and hence, on the crystallization kinetics. Acetaminophen in AAO with pore sizes smaller than 100 nm and cold crystallized at 80°C for 2 h in the presence of a surface reservoir yielded form III crystals. Cold crystallization in larger pores ($d > 100$ nm) preferred more the formation of form I crystals. Acetaminophen cold crystallized in the absence of a bulk

surface reservoir suppressed the crystalline state in favor of the amorphous form especially in AAO nanopores smaller than 100 nm.

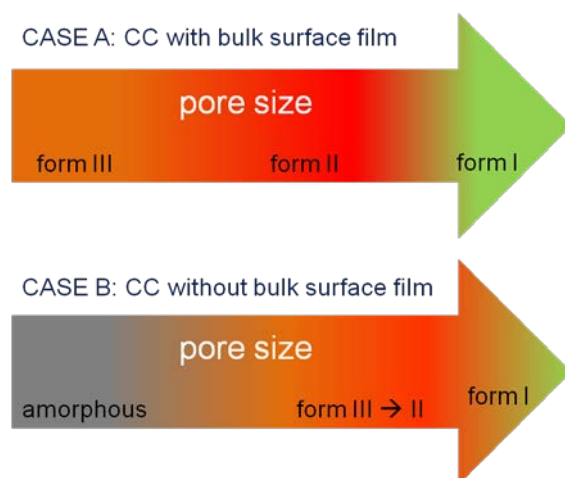


Figure 5.17: Acetaminophen in AAO cold crystallized at 80°C for 2 h in the presence (case A) or in the absence (case B) of a bulk surface reservoir.

5.5 Discussion of Acetaminophen in 2D-Confinement

The crystallization conditions such as pore morphology, pore size, thermal history, and presence or absence of bulk surface reservoir have been investigated in order to know their influence on the stability of acetaminophen forms under confinement.

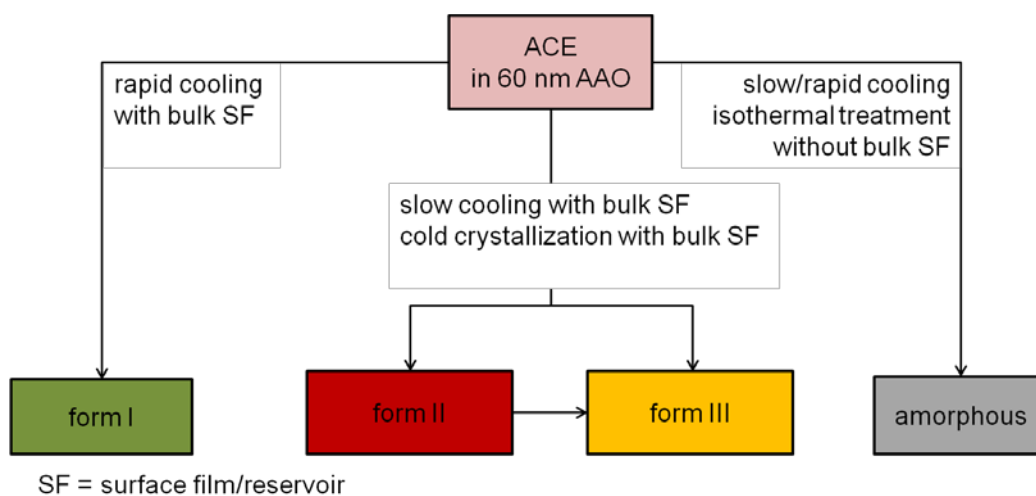


Figure 5.18: Acetaminophen in 60 nm AAO.

The results revealed that the mentioned crystallization parameter can be used as a tool for selective crystallization in AAO membranes. Figure 5.18 shows the routes for high-yield production of acetaminophen forms in 60 nm AAO membranes.

5.5.1 Crystallite Orientation and Crystal Growth Kinetics in AAO Membranes

(1) Crystallite Orientation

Directly after non-isothermal crystallization, form III crystals with pronounced uniaxial orientation were present in 60 nm AAO membranes. The ($h00$) lattice planes were oriented normal to the AAO pore axis see Chapter 5.1.2. Form III crystals undergo a solid/solid transition to form II crystals when the AAO membrane is annealed above the melting temperature of form III in 60 nm AAO. An interesting fact is that both forms grew with a highly oriented crystal texture. In acetaminophen form II the ($0k0$) lattice planes (Figure 5.19) and in form III the ($h00$) lattice planes are oriented normal to the AAO pore axis.

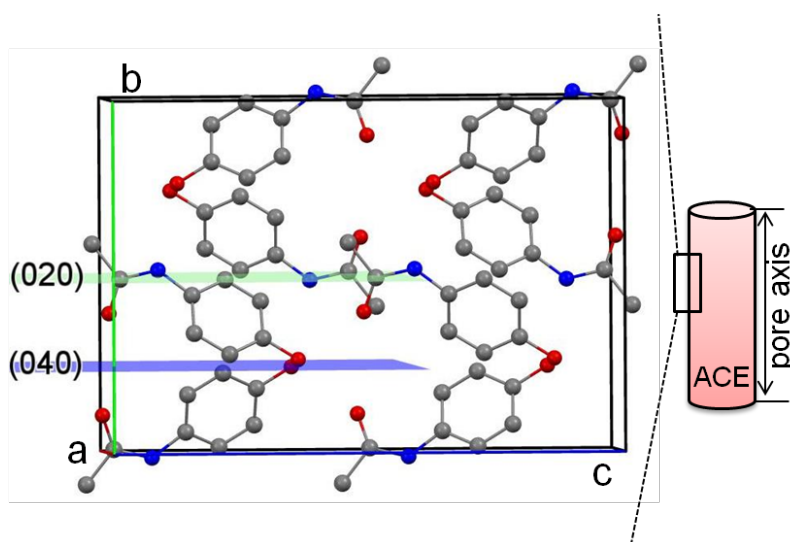


Figure 5.19: Acetaminophen form II ($0k0$) lattice planes oriented normal to the AAO pore axis, visualized with Mercury 3.1. Oxygen atoms are red, nitrogen atoms are blue, carbon atoms are grey, hydrogen atoms are not shown.

Schulz scans yielding orientation distributions of lattice planes revealed that orientation distributions of form III (400) and form II (040) lattice planes coincide. Additionally, form III (400) and form II (040) lattice planes have similar d -values. *Perrin et al.*⁶⁵ suggest that form II and III have topologically equivalent two-dimensional layers of hydrogen-bonded acetaminophen molecules. But they differ with respect to the tilt angles between the benzene rings and the hydrogen-bonding plane.

In the diffraction patterns of form II and III, the positions of several peaks coincide. These findings suggest similar unit cells and hence, similar main lattice planes along the directions oriented parallel to the AAO pore axis. The extension of the orthorhombic unit cell form II in $\langle 0k0 \rangle$ direction is equal to the extension of a suggested orthorhombic unit cell form III in $\langle h00 \rangle$ direction.

The results can be summarized as follows. Slow cooling rates at -0.5 K/min in the presence of a bulk surface reservoir yielded uniaxial oriented acetaminophen form III crystals in 60 nm AAO. Due to the close structure registry of form III in the $\langle h00 \rangle$ and of form II in the $\langle 0k0 \rangle$ directions uniformly oriented form III crystals can undergo a monotropic solid/solid transition to also uniformly oriented form II crystals. The solid/solid transition can propagate through the AAO pores due to their highly similar structure and due to the cylindrical pore geometry.

(2) Crystal Growth Kinetics

Crystallite coherence lengths of form I and form II crystals were estimated using the Scherrer equation (see Eq. 4.1). In 60 nm AAO membranes acetaminophen form I crystals have coherence lengths parallel to the AAO pore axis of ~ 43 nm and form II crystals have a length of ~ 63 nm. One can conclude that different cooling rates yield different polymorphs and that the polymorph crystals differ in their crystallite coherence lengths. Therefore a mechanism might exist that influences the crystallization kinetics. Crystallization happened when the material was in contact with an acetaminophen bulk surface reservoir on top of the AAO membranes. In the bulk material, crystal formations occur via heterogeneous nucleation. Bulk acetaminophen crystals impinge on the AAO membrane surfaces and might offer pre-existing crystal faces for heterogeneous nucleation on the AAO pore mouth. Only bulk crystals which have their fast growth

direction aligned with the AAO pore axis can grow into the pore. It is a well-known fact that anisotropic pores dictate fast crystal growth parallel to the pore axis (Figure 5.20). This observation has been interpreted as a version of the Bridgman single-crystal growth process.¹⁰⁰ Furthermore, slow growing crystals or crystal faces without their fast-growth direction aligned with the AAO pore axis are suppressed in cylindrical nanopores. Other nucleation mechanisms that initiate the formation of crystals away from the pore mouth might be suppressed.



Figure 5.20: Schematic view of acetaminophen form III/form II fast-growth direction aligned with the AAO pore axis.

After nucleation some crystal faces can grow faster in specific crystallographic directions. The growth rates are influenced by the attachment rates of the molecular building blocks to each crystal face. Following the Hartman and Perdok³⁷ model (see Chapter 1.1.3) it can be concluded that acetaminophen should have rough crystal faces without connected nets of molecular growth units oriented normal to the AAO pore axes. During crystal growth, the energy of a crystal face guides the crystal growth direction. It can be assumed that the occurrence of preferred crystal faces of form II/III are influenced by the different growth rates of lattice planes. On a fast-growing crystal plane, the attachment rates of building blocks normal to the growth direction are higher than on a slow-growing crystal face. It can be concluded that the form III $\langle h00 \rangle$ direction is a fast-growing direction aligned to the AAO pore axis. Attachment-energy prediction¹⁰¹ suggests that the (020) lattice plane of acetaminophen form II is a slow

growing face. This could suggest that form III is nucleated firstly, and then converted to form II crystals undergoing a solid/solid transition.

Furthermore, growing crystals compete for growth volume. In straight non-connected nanopores the crystal growth rate parallel to the pore axes is higher than in any other direction (Figure 5.20). The free growth path there is tens of micrometers. Instead the free growth path in diameter is only few tens of nanometers.

The crystal growth is also affected by kinetic selection processes¹¹. Rapid cooling from melt favors more nucleation than crystal growth. Crystallization takes place at low temperatures, and therefore at high supercooling. High supercooling supports homogeneous nucleation with formation of many nuclei. Hence, many growing crystals compete for growth volume. It is possible that crystals with different growth directions have a change to occupy a certain growth volume. Fast growing crystals originated from the heterogeneous nucleation close to the pore mouth might grow, but they might also impinge on other growing crystals. As a consequence, the dominance of the crystallites having (020)/(040) form II or (400) form III lattice planes oriented normal to the pore axis are suppressed. In 60 nm AAO, rapid cooling from melt in the presence of a bulk surface reservoir favors several populations of form I crystals with different orientations. Furthermore, the different growth directions of form I crystals explain the shorter crystallite coherence length. Form II and/or form III crystals can rapidly grow along the AAO pores. In contrast, growing form I crystals may impinge on other growing form I crystals.

(3) Amorphous Form

Amorphous form can be reached when material is quenched from melt due to rapid cooling.²⁴ In thermodynamics terms, it can be said that if no crystallization occurs, the nuclei for the crystalline forms cannot overcome the critical size r^* and will not reach a size necessary for crystal growth. Henceforth, the amorphous form is thermodynamically stable under the given system. Not reaching the crystalline state can be also due to kinetic reasons. During rapid cooling the material is transferred to lower temperatures very quickly. At low temperatures molecular mobility might be too small to observe crystallization²². The investigation of acetaminophen in 60 nm AAO showed

that the amorphous form can also be obtained by slow cooling at -0.5 K/min in the absence of a bulk surface reservoir. It might be assumed that the occurrence of amorphous acetaminophen in AAO membranes is linked to the availability of material during cooling. In absence of bulk acetaminophen in each pore, the material crystallizes separately. Therefore, nucleation process shifts from heterogeneous to homogeneous. As a result, the reduced number of heterogeneous nuclei or the increase of homogeneous nuclei in smaller pores could contribute to slow crystallization kinetics since each crystallizing volume is homogeneously nucleated. Or in other words, the system must overcome a higher nucleation barrier.

The formation of amorphous drugs may be of interest for further studies. In most of the cases amorphous forms could have better dissolution rates and hence, a better bioavailability than their crystalline counterparts. For drug formulation, it could be useful to know which conditions support the amorphous form. Furthermore, the results show that the amorphous form is stable under typical storage conditions for specific shelf time intervals.

5.5.2 Influence of Pore Sizes and Volume on Crystallization in AAO Membranes

The results from Chapter 5.4 revealed that the occurrence of acetaminophen modifications depended on different factors such as the pore volume, the pore size and hence, the crystal size. The existence of different formations under confinement can also have kinetic reasons. Acetaminophen in AAO with pore sizes from 25 nm to 400 nm slowly cooled with bulk surface reservoir revealed form II/form III crystals with their $(0k0)/(h00)$ lattice planes oriented normal to the AAO pore axis. It can be assumed that the same nucleation and crystal growth mechanism takes place as described for acetaminophen in 60 nm AAO. Table 5.4 summarizes the occurrence of the $(0k0)$ and $(h00)$ lattice planes in 25 nm and 60 nm AAO membranes.

Table 5.4: Acetaminophen in 25 and 60 nm AAO cooled at -0.5 K/min in the presence of a bulk surface reservoir.

Polymorph: main reflections (Index)	AAO 60 nm (11 samples)	AAO 25 nm (17 samples)
form II: $14.9^\circ(020)$, $30.1^\circ(040)$	36%	53%
form III: $30.1^\circ(400)$	36%	47%
other main reflections of form II or III occasionally form I	27%	/

In both AAO pore sizes form II or form III reflections occur with a 50% probability. Further, in 25 nm AAO membranes other crystallite orientations are suppressed due to the vicinity of the pore walls.

Cold crystallization experiments in AAO membranes with pore sizes of 60 nm or smaller, in absence of a bulk surface reservoir, yielded amorphous acetaminophen. The same results can be achieved when acetaminophen is cooled from melt with no contact with bulk surface material. In absence of bulk material, the nucleation process starts in each pore separately towards a more homogeneous nucleation. Nucleation is more favored than crystal growth. The crystallization kinetics may be influenced by immobilized surface layers. Such layers can have a thickness of around one nanometer and are formed at high energy pore walls.²² This effect could be relevant when the surface-to-volume ratio increase due to smaller pore sizes (Table 5.5). Acetaminophen can interact with the hydroxyl-terminated AAO pore walls which might stabilize the amorphous form in smaller pore sizes ($d < 100$ nm).

Table 5.5: Estimated single pore volume, pore area, and surface-to-volume ratio of cylindrical AAO pores.

	AAO 25 nm	AAO 60 nm	AAO 180 nm	AAO 400 nm
r [nm]	12.5	30	90	200
h [μ m]	100	100	100	100
<u>cylindrical single pore</u>				
volume $\pi r^2 h$ [μ m ³]	0.05	0.28	1.1	13
area $2\pi r^2 + 2\pi r h$ [μ m ²]	7.8	19	38	130
surface-to-volume ratio	160	68	35	4.0

AAO nanopores with pore sizes larger than 180 nm have a higher pore volume and therefore, more material inside the pores. In such pores, cold crystallized acetaminophen tends to be converted to the crystalline state. One explanation might be that fewer molecules are influenced by the AAO pore walls than in pores below 180 nm. Away from AAO pore walls, the material may form 3D crystal structure more easily. Due to the higher pore volume it is more likely that additional to homogeneous nucleation heterogeneous nucleation may occur inside the pores, which influence the ability of the material to crystallize.

Cold crystallization has been done at one specific temperature and in a chosen time period. It should be kept in mind that other temperatures or longer cold crystallization time might yield different results. The main aim of this investigation is to present the influence of the AAO pore size on the crystallization behavior.

5.5.3 Influence of Pore Morphology on Crystallization in Nanoporous Matrices

Figure 5.21 displays an overview of acetaminophen formation in 60 nm CPG. The results show that the crystallization parameters have importance to control the crystallization of acetaminophen under confinement.

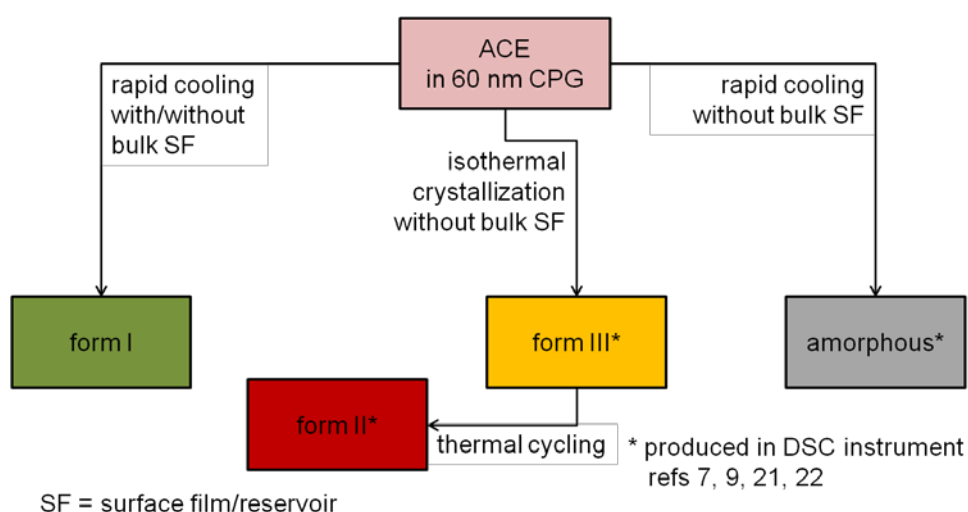


Figure 5.21: Acetaminophen in 60 nm CPG.

After comparison of the two systems, anisotropic AAO and isotropic CPG membranes, the results revealed that the pore morphology influences the crystallization kinetics. For example, acetaminophen in AAO cooled at -0.5 K/min in contact with a bulk surface reservoir contained uniaxial oriented form III crystals. Under identical conditions form I crystals are preferentially formed in CPG membranes. In AAO membranes the uniformly oriented form III crystals undergo a solid/solid transition to also uniformly oriented form II crystals. In CPG matrices the solid/solid transition is suppressed. The differences are explained as follows. Crystallization in CPG is initiated by a few heterogeneous nuclei due to the interconnection of the pores. It can be assumed that crystal growth of form I occurs along directions with slow growth rates. Crystal faces with their fast-growth direction aligned to the pore axis can grow in both AAO and CPG membranes. However, in CPG, due to the curved morphology, fast growing crystal faces will impinge on the pore walls. Therefore, one can assume that the limited free growth path in CPG membranes prevents the kinetic selection process of form II/III which occurs in AAO membranes (Figure 5.22).

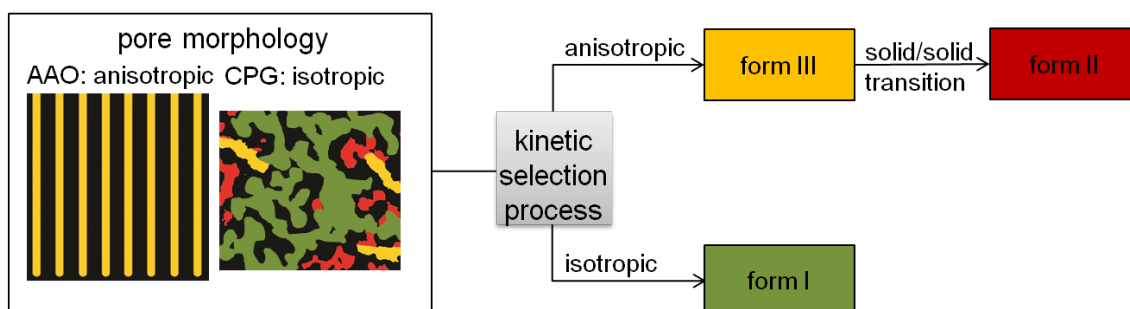


Figure 5.22: The pore morphology directs polymorph formation and influences the kinetics of the solid/solid transition of acetaminophen.

In CPG membranes, form II was only achieved during thermal cycling of form III. One reason why the solid/solid transition easily occurs in AAO could be the length of the nanopores. In AAO membranes the transition front propagates through the straight pore. In CPG, the propagation front will impinge on pore walls after short path. In CPG matrices, the formation of form II crystals with different orientations might be accompanied by the formation of energetically unfavorable grain boundaries.⁸⁷

6 Release Kinetics of Acetaminophen from AAO Membranes

AAO membranes with tailored pore geometries are interesting materials for controlled drug delivery systems. The ordered and controlled pore structures can have an influence on dissolution rates of the drug molecules from the pores and therefore, of the drug release.^{18, 20} In general, the drug release is a kinetic process and quantified by the dissolution rate in dependence on the time. For testing the release kinetics of acetaminophen dissolution measurements were performed. Such *in vitro* tests provide an opportunity to make precise and reproducible release measurements. The methods are divided in two types: natural or forced convection.⁴¹ The main difference is that the forced convection includes a degree of agitation. The used dissolution test apparatus in this study falls in the latter category. Release kinetic measurements give answers how the elution of a drug depends on parameters such as solid form (i.e., crystalline or amorphous) or particle size. Beside this, drug dissolution is affected by more parameters such as the surface wetting, the chosen medium, or the matrix material.

6.1 Controlled Drug Release from 60 nm AAO Membranes

To achieve acetaminophen form I, form II and amorphous form in 60 nm AAO membranes, the material was infiltrated and cooled as is described in Chapter 5.1. Prior infiltration, the AAO membranes were cut in 1 x 1 cm pieces. After infiltration and cooling, all samples were cleaned with a wetted tissue to remove any residues outside the AAO membranes. The collected WAXS patterns were in line with nanosized acetaminophen form I from Ch. 5.1.1, Figure 5.1 or with form II from Ch. 5.1.2, Figure 5.2. The main $\theta/2\theta$ reflections of the crystalline samples are listed in Table 6.1. Amorphous acetaminophen showed no reflections in $\theta/2\theta$ scans. Each AAO membrane contained approximately 3–4 mg acetaminophen.

Table 6.1: Acetaminophen in 60 nm AAO, acetaminophen modifications, and main lattice planes.

AAO membrane [nm]	Acetaminophen modification	Main lattice planes (Index)
60	amorphous	/
	form I	(101) (200) (-220)
	form II	(020) (040)

The dissolution tests itself took place where the AAO membranes were placed in a medium which was shaken (Figure 6.1).

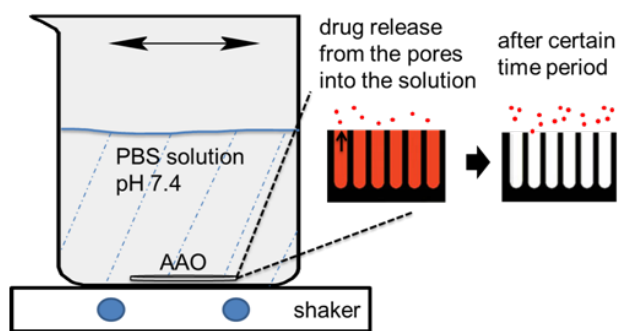


Figure 6.1: Schematic view of dissolution test conditions.

The AAO membranes were immersed in 6 mL phosphate buffered saline solution (PBS pH 7.4) under ambient conditions with shaking at 140 r.p.m. (IKA[®] KS260) over the dissolution testing time. 500 μ L of PBS aliquot were withdrawn after specific time intervals (Table 6.2). Immediately 500 μ L fresh PBS was added to the solution.

Table 6.2: Drug release at specific time intervals.

Release time [min]	Time intervals [min]
first 10	2
10–30	4
30–60	10
60–180	40
180–360	60
then after 1, 2 day(s)	

The amount of released acetaminophen was quantified with an UV–visible spectrophotometer (Varian Cary 50). The absorption maximum for acetaminophen in PBS appeared at 250 nm. Standard solutions with known concentration of acetaminophen were prepared. The sample concentration was adjusted to compensate the dilutions during the replacement with fresh PBS (see Appendix A). After dissolution testing AAO membranes were rinsed with water, and dried under vacuum to check the empty weight of the AAO membrane again. Figure 6.2 shows dissolution data for acetaminophen form I, form II, and amorphous form released from 60 nm AAO membranes, respectively. The released amount of acetaminophen at time $[A]_t$ was divided by the infiltrated material $[A]_0$.

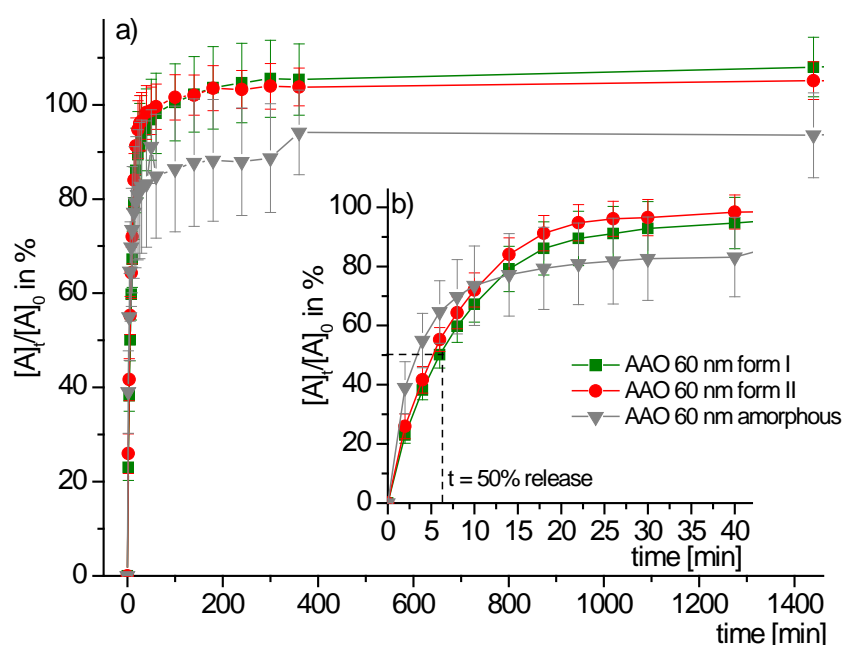


Figure 6.2: Dissolution testing; (a) Acetaminophen form I, form II, and amorphous form embedded in AAO 60 nm. Each data point represents the mean of six determinations \pm standard deviations. (b) The inset showed a zoomed temperature range.

The dissolution data revealed that acetaminophen was dissolved very fast in the first few minutes. The time when 50% of the material was eluted is listed in Table 6.3. As

can be seen, half of the material was eluted into the surrounding PBS medium within minutes.

Table 6.3: Time taken for 50% of acetaminophen release from 60 nm AAO.

Acetaminophen form	50% released at t [min]
form I	~ 8
form II	~ 6
amorphous	~ 4

Moreover, acetaminophen form I and form II were completely eluted within one hour. On the contrary, not each amorphous sample reached complete dissolution. Additionally, amorphous samples showed higher standard deviations than the crystalline counterparts (Figure 6.2).

6.2 Controlled Drug Release from AAO with Pore Sizes Ranging from 25 to 400 nm

To investigate the influence of AAO pore sizes on dissolution, acetaminophen form II was confined to AAO with pore sizes ranging from 25 nm to 400 nm. The infiltrated material was cooled at a rate of -0.5 K/min in the presence of a bulk surface reservoir (Details can be found in Chapter 5.4.1). Before $\theta/2\theta$ measurements the surface material was scrapped off. Under these crystallization conditions uniaxial oriented form II or/and form III crystals were obtained inside the nanopores. The resulting $\theta/2\theta$ patterns are shown in Figure 5.10. Main 2θ reflections depending on the AAO pore size are listed in Table 6.4.

Table 6.4: Acetaminophen form II/III in AAO with pore sizes ranging from 25 nm to 400 nm.

AAO membrane [nm]	Main 2 θ reflections [°]	Comments
400	12.7, 14.9, 20.7, 23.7	mixtures of form II/III
180	14.9, 20.7, 23.7, 30.1	mixtures of form II/III
60	14.9, 30.1	form II
25	14.9, 30.1	form II

The results in Figure 6.3 show that the AAO pore size had no influence on the drug release from AAO membranes. Each pore diameter showed the same initial fast drug dissolution followed by a slower release. At the beginning, acetaminophen form II was eluted fast as a burst. Half of the material was diluted within 10 min. In each AAO pore sizes nearly 100% release were achieved in less than one hour.

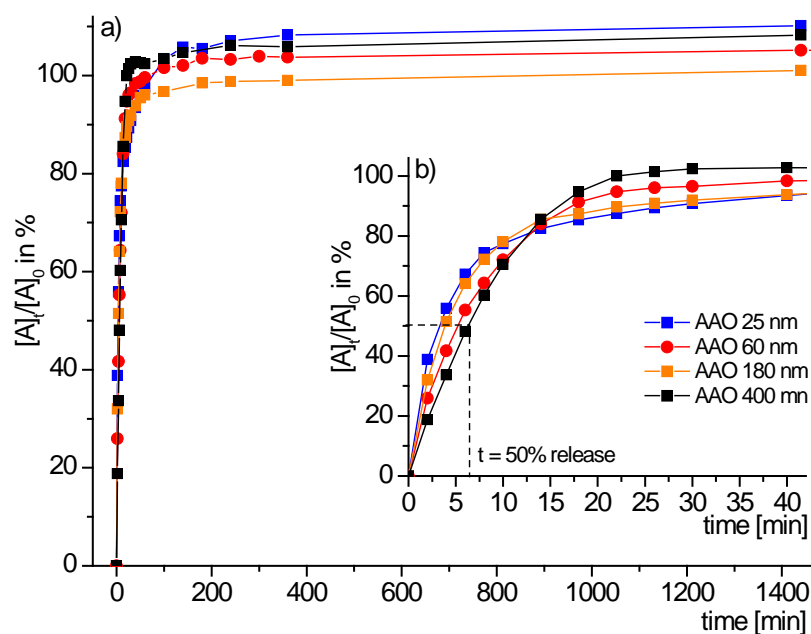


Figure 6.3: Dissolution testing of acetaminophen form II (a) from AAO membranes 25–400 nm. Each data point represents the mean of two determinations, except AAO 60 nm six determinations. (b) The inset showed a zoomed temperature range.

6.3 Kinetic Modeling of the Drug Release

A very important aspect in the pharmaceutical research is the analysis of the drug release mechanism. In the most cases, the dissolution data have been fitted to simple or more sophisticated mathematical models. The vast majority of the mathematical models are based on diffusion equations. A characterization of the drug dissolution mechanism will help to understand the release system. In general, the dissolution can be (i) diffusion, (ii) swelling, or (iii) chemically controlled.¹⁰² The pore morphology also has, beside other parameters, an impact on the dissolution rates.

In this study, the collected dissolution data were fitted to the zero-order and first-order kinetic laws. The zero-order release law can be written as:

$$\frac{[A]_t}{[A]_0} = kt \quad 6.1$$

where $[A]_t$ is the released acetaminophen at time t and $[A]_0$ is the infiltrated material at $t = 0$.

Drug release data can also be fitted to the first-order release kinetic. The linearized form of the first-order law is:

$$\ln\left(\frac{[A]_t}{[A]_0}\right) = -kt \quad 6.2$$

When $\ln[A]_t/[A]_0$ is plotted against t , a first-order release will give a straight line of slope $-k$ ³³.

The obtained data of acetaminophen released from 60 nm AAO membranes in Figure 6.2 were fitted to both kinetic laws. The fitting parameter R^2 (i.e., regression coefficient) was used as the best fit criteria. The coefficient can be estimated with the coefficient of correlation r . The correlation coefficient measures the strength and direction of the linear relationship between two variables.¹⁰³ It is defined as the sample covariance of the variables divided by the product of their sample standard deviations and can be written as:

$$r = \frac{\sum_{i=1}^k [(x_i - \bar{x}) \cdot (y_i - \bar{y})]}{\sqrt{\sum_{i=1}^k (x_i - \bar{x})^2 \cdot \sum_{i=1}^k (y_i - \bar{y})^2}} \quad 6.3$$

where x_i is the concentration, y_i is the absorption signal at 250 nm, \bar{x} and \bar{y} are the arithmetic means¹⁰³, and k is the number of data points.

For a better modeling of the controlled drug release from different matrices more mathematical concepts have been developed. A simple exponential relation gives the Korsmeyer-Peppas model.^{102, 104, 105}

$$\frac{[A]_t}{[A]_0} = kt^n \quad 6.4$$

where n is the diffusional exponent and describes the transport mechanism. With $n = 1$ the release follows the zero-order law (see Eq.6.1). The exponent n has been investigated for different shaped matrices. For example, in a cylindrical system $n = 0.45$ describes a Fickian diffusion and between 0.45 and 0.89 an anomalous (non-Fickian) transport.¹⁰² The limitation factor is that the model should only be used for the first 60% of the release (i.e., $[A]_t/[A]_0 \leq 0.6$).^{102, 104} According to the limitation, dissolution data from Figure 6.2 were also fitted to the Korsmeyer-Peppas model and are shown in Figure 6.4.

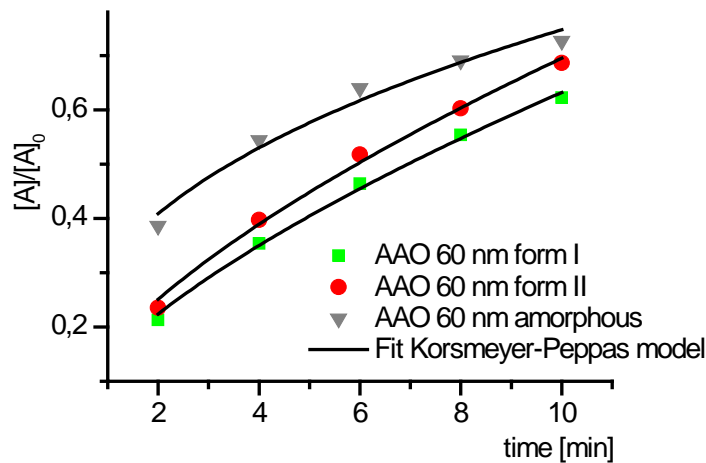


Figure 6.4: Acetaminophen form I, form II and amorphous form confined to AAO. Release data fitted to the Korsmeyer-Peppas model.

For curve fitting the OriginLab software version 8G was used. Equation 6.4 was inserted in the fitting function organizer¹⁰⁶. The organizer works with the Levenberg-Marquardt method¹⁰⁷. This method is typically used to solve non-linear least squares problems. Table 6.5 summarizes the results of the first 10 minutes dissolution.

Table 6.5: Diffusional exponent n and regression coefficient R^2 for drug release of acetaminophen modifications from 60 nm AAO.

Acetaminophen modification	Zero-order kinetic		First-order kinetic	Korsmeyer- Peppas model		
	R^2	k [min^{-1}]	R^2	n	R^2	k [min^{-n}]
amorphous	0.890	0.04	0.824	0.37	0.970	0.31
form I	0.975	0.05	0.894	0.65	0.996	0.14
form II	0.969	0.06	0.891	0.62	0.994	0.18

For both crystalline forms the diffusional exponent n suggests that the drug release mechanism is not diffusion limited. The drug release from AAO membranes takes place via a non-Fickian transport in the first minutes. Obviously, amorphous acetaminophen exhibited lower regression parameters than the crystalline forms. The diffusional exponent n for the amorphous sample amounted below 0.45. The Korsmeyer-Peppas model proposes a Fickian behavior.

6.4 Encapsulation of Acetaminophen in AAO Membrane using Polymer Films

The dissolution results of acetaminophen from Chapters 6.1 and 6.2 revealed that most of the material was eluted within 15 min. For some applications a more controlled or retarded drug release is necessary. In literature¹⁰⁸ one discussed strategy is to reduce the pore size of the nanoporous drug hosts. However, the release kinetics of acetaminophen from AAO membranes showed no effects depending on the pore size (Figure 6.3). *Simovic et al.*¹⁰⁸ retard the drug release via a polymer layer which is placed on top of the drug containers. A biodegradable polymeric microchip is used for controlling the drug

release in the research done by *Grayson at al.*¹⁰⁹. According to the published results a polymer was selected for encapsulating of acetaminophen in AAO nanopores. As a requirement, the polymer should be biocompatible and *in vitro* degradation should be possible. For these reasons poly(L-lactide) PLLA was chosen. PLLA belongs to the aliphatic polyester family which is an attractive group of polymer for medical applications. Further, PLLA has a high level of biocompatibility and degradation rates. The polymer itself degrades *in vivo* through hydrolysis of the ester linkage in the polymer backbone.¹¹⁰ The degradation is also possible when *in vitro* a water based medium is used.

For polymer deposition and dissolution testing, acetaminophen form II was crystallized in 60 nm AAO membranes as illustrated in Figure 6.5 step 1. More details of acetaminophen form II preparation in AAO membranes is described in Chapter 5.1.2. Theta/2 theta measurements showed two dominant reflections at $2\theta = 14.9^\circ$ belonging to the (020) lattice planes and at $2\theta = 30.1^\circ$ belonging to the (040) lattice planes. Both reflections were typical for acetaminophen form II in 60 nm AAO (Figure 5.2b).



Figure 6.5: Schematic view of sample preparation and drug release: (1) acetaminophen form II (red) in AAO membranes (black), (2) PLLA film spin-coated on the infiltrated AAO membrane, (3) degradation of the PLLA film and controlled drug release.

For polymer deposition 10 mg PLLA with number-average molecular weight $M_n = 13500$ from Polymer Source Inc. was completely diluted in 100 μL THF. 10 μL of the solution was spin-coated (30 s 800 r.p.m., G3P-8 Spincoat, SCS) on the AAO membranes containing acetaminophen form II. The process was fourfold repeated, and then the samples were dried for 2 h under vacuum. The weight of the infiltrated acetaminophen and polymer film was monitored. On the membranes 3–4 mg/cm^2 PLLA

polymer were coated (Figure 6.5 step 2). It can be supposed that the rapid evaporation of the solvent prevents elution of the infiltrated acetaminophen during coating. SEM images in Figure 6.6a/b showed a compact polymer structure on AAO membranes. The cross sectional SEM image in Figure 6.6b revealed a polymer film thickness of around 3 μm .

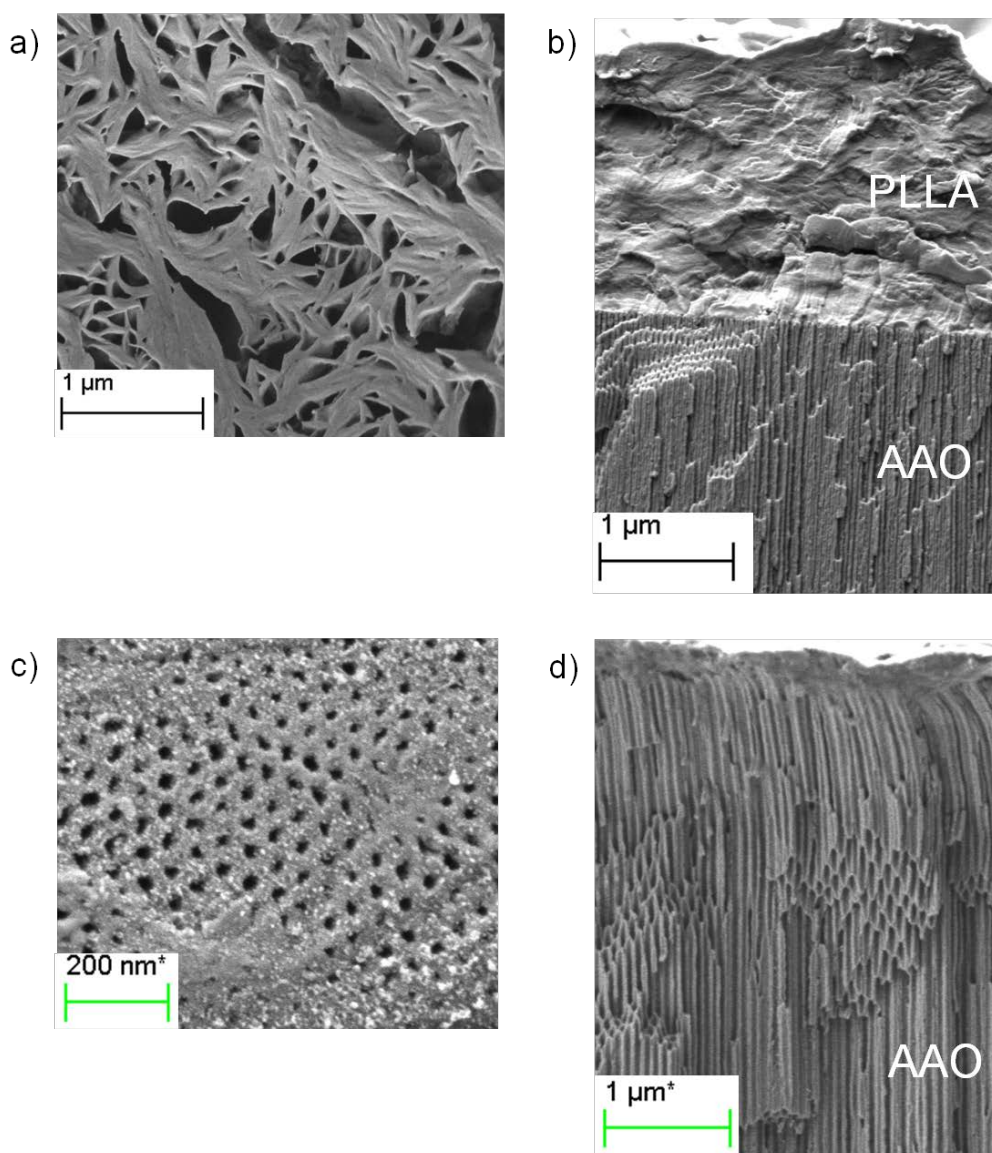


Figure 6.6: SEM images of; (a) PLLA polymer film on the AAO membrane, (b) cross-section view of the AAO membrane (bottom) and the PLLA polymer film (top), (c) residues on the AAO membrane after dissolution test (d) cross-section view of the AAO membrane (bottom) after dissolution test.

Theta/2theta measurements were carried out after spin-coating. The dried PLLA film showed only one strong reflection at $2\theta = 16.6^\circ$ indexed as the (200) or (110) lattice planes according to reference 111. After coating, weak peaks of acetaminophen form II occurred at $2\theta = 14.9^\circ$ (020) and 30.1° (040), respectively. Encapsulated acetaminophen in AAO was also placed in PBS medium as is described in Chapter 6.1. The last step in Figure 6.5 involved the degradation of the PLLA polymer film via hydrolysis of the ester linkage and therefore, the retarded drug release into the surrounding PBS medium. After dissolution and drying, the SEM images (Figure 6.6c/d) of AAO membranes showed residues of PLLA and/or dried PBS solution. Release data of acetaminophen form II in 60 nm AAO coated with PLLA or uncoated are shown in Figure 6.7.

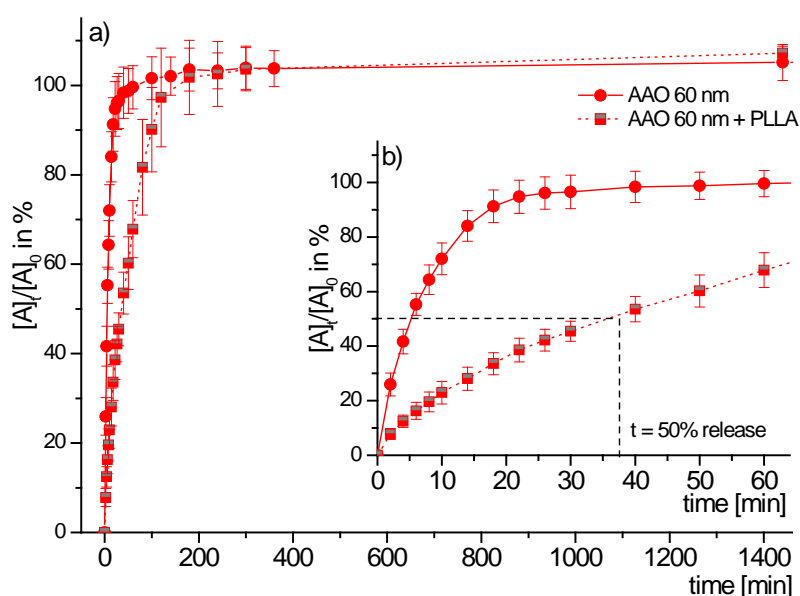


Figure 6.7: Dissolution testing of acetaminophen form II in 60 nm AAO (a) uncoated and coated with PLLA polymer film. (b) The inset showed a zoomed temperature range. Each data point represents the mean of four(coated)/six(uncoated) determinations \pm standard deviations.

Uncoated samples released nearly 50% of the loaded acetaminophen in 6 min. On the other hand, coated samples released the same amount of material in ~35 min (Figure 6.7b). The fitting parameters revealed that the Korsmeyer-Peppas model (Table 6.6) accounted best for the experimental data. The diffusional exponent n suggests a non-

Fickian transport ($n > 0.45$) in the first 60 minutes for coated samples. Moreover, the rate constant k differed significantly between coated and uncoated samples. Higher values indicates a faster release or vice versa. For uncoated samples, the rate constant amounted to ~ 0.2 describing a burst drug release. Lower values with $k \sim 0.05$ indicated a retarded release from coated AAO membranes.

Table 6.6: Release law/model and regression coefficient R^2 for the drug release of acetaminophen from 60 nm AAO coated with PLLA.

Release law/model (fitted time)	Regression coefficient R^2	Rate constant k
Zero-order release (22 min)	0.988	0.015 [min ⁻¹]
First-order release (15 min)	0.886	/
Korsmeyer-Peppas model (60 min)	0.999 ($n = 0.66$)	0.049 [min ⁻ⁿ]

It is remarkable that between coated and uncoated samples the diffusional exponent with $n \sim 0.6$, which describes the transport mechanism, did not change significantly. It seems, that encapsulation of acetaminophen in AAO nanopores influences the dissolution time, but not the dissolution mechanism.

6.5 Discussion

The dissolution testing method is an easy way to study the release of acetaminophen from AAO membranes. Acetaminophen form I, form II and the amorphous form were embedded in AAO membranes with pore sizes of 60 nm, and then placed in water based buffered saline solution. At the beginning, all three forms exhibited high dissolution rates (Figure 6.2). The obtained dissolution profiles showed the best fit results to the Korsmeyer-Peppas model. For the crystalline samples the diffusional exponent amounted to ~ 0.6 and suggested a non-Fickian transport mechanism. On the other hand, for amorphous forms the regression coefficients amounted to lower values (Table 6.5). Amorphous formulations displayed higher standard derivations (Figure 6.2) compared to the crystalline counterparts. The diffusional exponent n amounted to ~ 0.4 for

amorphous samples. The rate constant k with 0.3 is higher than for crystalline samples with $k \sim 0.1$. Additionally for the time period investigated, reaching the total elution was two-times lower for amorphous samples than for crystalline forms. In general, dissolutions of nanosized acetaminophen from 60 nm AAO or form II from AAO membranes with pore sizes ranging from 25 nm to 400 nm can be described as a two-phase release, with an initial burst phase within the first 10 minutes and a slower phase thereafter.

Dissolution rates of crystalline samples are not diffusion controlled. This might suggest that the transport is surface-limited. The slower dissolution rates may be diffusion-controlled release from deeper nanopore structures¹¹².

The results can be explained as follows. During dissolution, solvent molecules rearrange around a solid interface i.e. acetaminophen crystal surfaces. A solid-liquid interface is built with several interactions between solvent molecules and crystal faces. Such short-distance interactions are referred to as solvent forces. Solvent forces depend on the properties of the liquid medium and on the chemical and physical properties of the surfaces (e.g., smooth or rough, amorphous or crystalline). Dissolution rates are also influenced by the geometry of the molecules and how the solvent molecules can be packed around the solid surface.¹¹³ Additionally, dissolving simulations of acetaminophen form I show that release rates depend on the molecules arrangement on crystal faces.¹¹⁴

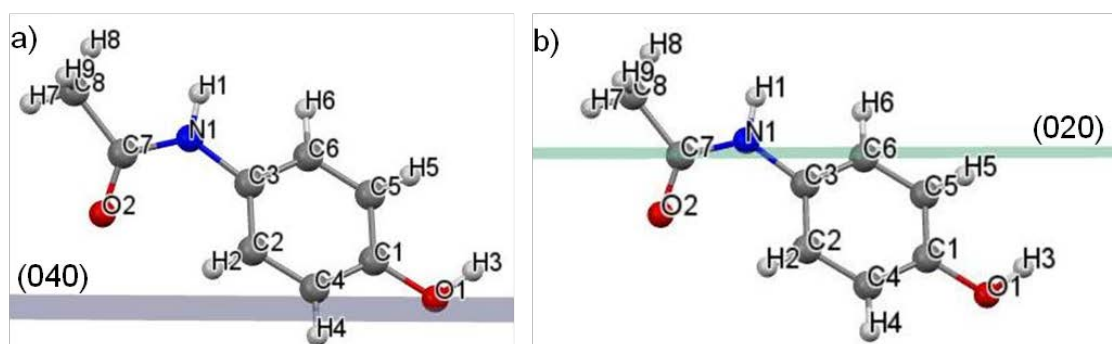


Figure 6.8: Acetaminophen form II in 60 nm AAO. The molecule arrangement in the orthorhombic unit cell is visualized with Mercury 3.1; (a) orthorhombic (040) crystal face, (b) orthorhombic (020) crystal face.

The crystalline nanosized acetaminophen exposed only few crystal faces to the solvent. Outfacing functional groups might interact with water molecules and/or PBS buffer ions. As a result, acetaminophen–acetaminophen molecule interactions will decrease and solvent–acetaminophen interactions will increase. Solvation or hydration forces will become dominant. A good example is, acetaminophen form II in AAO membranes contained uniaxial oriented (020)/(040) crystal faces (Figure 5.19). On such crystal faces the hydroxyl groups of the aryl moieties protrude from the (040) faces (Figure 6.8a) whereas the amide carbonyl groups protrude from the (020) faces (Figure 6.8b). It can be concluded that hydroxyl or amide groups can form strong hydrogen bonds ($\text{O}-\text{H}\cdots\text{O}$) with solvent molecules. One can therefore assume that crystal faces with out-facing hydrophilic functional moiety might facilitate the interaction with solute molecules. As a result, dissolution rates of crystalline forms are as fast as amorphous forms. Note that the concept of solubility should not be applied to amorphous forms. The amorphous material in a solute can be understood as a kinetically driven state that is not in equilibrium.²⁵ In this study, the term ‘solubility’ is used in context of all acetaminophen formulations.

Nevertheless, in all three forms solvent molecules could more or less fluctuate fast through the pores. Fast dissolution rates indicate that solvent molecules and/or diluted molecules are less hindered to move out in the bulk medium. It should be kept in mind that the nanosize of the crystallites also favors higher dissolution rates.

However, dissolution profiles revealed differences between crystalline and amorphous forms. As previously reported⁷, acetaminophen forms rigid amorphous layer on CPG pore walls indicated by a second glass transition step (T_g) at $\sim 35^\circ\text{C}$ additional to the bulk T_g at $\sim 24^\circ\text{C}$. CPG and AAO pore walls are both hydroxyl-terminated and it can be assumed that CPG and AAO pore walls have a similar chemical behavior. Hence, acetaminophen might also form an immobilized layer on AAO pore walls. One can conclude that the amorphous material builds such a stable interfacial layer on AAO pore walls during the aging of the sample. Furthermore, such layers might influence the molecule mobility near the pore walls, too. As a result, complete release of amorphous acetaminophen from AAO nanopores takes more time than for crystalline samples. Crystalline samples may not form interfacial layers on AAO pore walls.

Anodic aluminum oxide membranes with different pore sizes do not influence the release kinetics of acetaminophen. The model drug acetaminophen is a small molecule. Therefore, the chosen pore sizes cannot control the drug delivery of such small sized molecules. Agreeing with a previous study¹¹⁵ of crystal violet in AAO membranes it has been suggested that the molecule size must extent that the pore size becomes the speed-controlling function. Another assumption might be that the crystallinity of the samples compensates the influence of the pore sizes on dissolution rates.

Using a biodegradable polymer for encapsulating acetaminophen in nanopores is one strategy to enlarge the drug release time. Acetaminophen infiltrated in AAO membranes and covered with a PLLA polymer film showed a retarded drug release (Figure 6.7). The dissolution results revealed that the rate constant k decreases from uncoated (0.2) to coated (0.05) samples. The diffusional exponent amounted to ~ 0.6 for coated as well as for uncoated samples. It is assumed that the release is not influenced by the diffusion of the solvent or hydrated acetaminophen molecules through the PLLA polymer film. The polymer film is slowly degraded when placed in the PBS medium due to the hydrolysis of the ester bound. The PLLA polymer film reduces and solvent molecules reach the acetaminophen in the AAO pores. It can be assumed that not all nanopores are open at the same time. Hence, dissolutions only occur when the PLLA polymer film is removed from the pores which lead to a retarded drug release. Experimental data suggests that the dissolution process of encapsulated ACE is surface-limited. Sealing the AAO nanopores with a PLLA polymer film influences the dissolution time due to the removal of the film before dissolution but does not influence the release kinetics.

7 *n*-Tetracosane Confined to Nanoporous Matrices

n-Tetracosane, a saturated hydrocarbon, has been chosen as a second model compound to investigate phase behavior and crystal texture of nanosized materials. *n*-Tetracosane confined in nanopores might link the crystallization results of the low-molecular weight material acetaminophen with the more complex crystallization performance of polymers. *n*-Tetracosane was solidified in anodic aluminum oxide (AAO) and in controlled porous glasses (CPG) membranes. The crystallization parameter i.e., the presence or absence of a bulk surface film, the pore size and the AAO pore wall chemistry were changed. The confined material was investigated using temperature-dependent X-ray diffraction and differential scanning calorimetry.

7.1 Crystallization of Bulk *n*-Tetracosane

As mentioned in Chapter 2.4 *n*-alkanes show, between the solid and the liquid phase, a series of rotator phases. To investigate rotator phases, one option is to crystallize the material in confined geometry. Often it is necessary to start with the bulk material itself, and then investigate the effects of confined geometry on crystallization behavior. For this purpose, bulk *n*-tetracosane was melted on a silicon wafer at 80 °C and cooled to room temperature under ambient conditions. Since rotator phases occur at higher temperatures temperature-dependent measurements are necessary. The crystallized material, independently if solidified on a silicon wafer or in nanopores, was investigated with temperature-dependent WAXS and Schulz scans. The used temperature profile is illustrated in Figure 7.1. A first scan was taken at 25 °C, then the XRD device stepped up to the next temperatures, held the temperature constant for 15 min before a new WAXS or Schulz scan started.

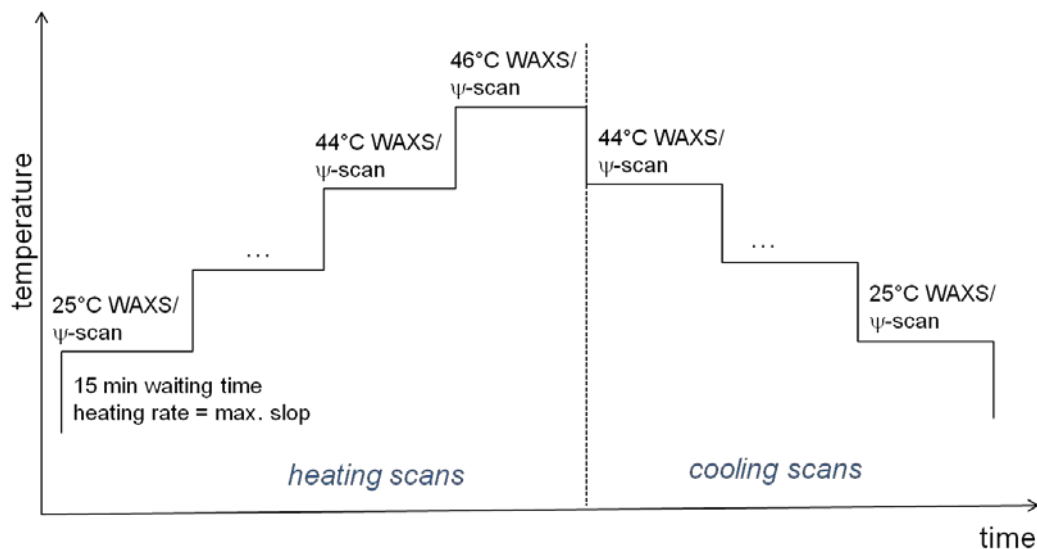


Figure 7.1: Programmed temperature profile for WAXS and Schulz (ψ) scans.

Characteristic reflections of triclinic *n*-tetracosane are the (010) at $2\theta = 19.2^\circ$, the (100) at $2\theta = 19.6^\circ$, the (011) at $2\theta = 23.2^\circ$, and the (111) at $2\theta = 24.7^\circ$ (Figure 7.2). The peaks were indexed according to reference found in the CSD deposition number ZZZOFCO4⁷².

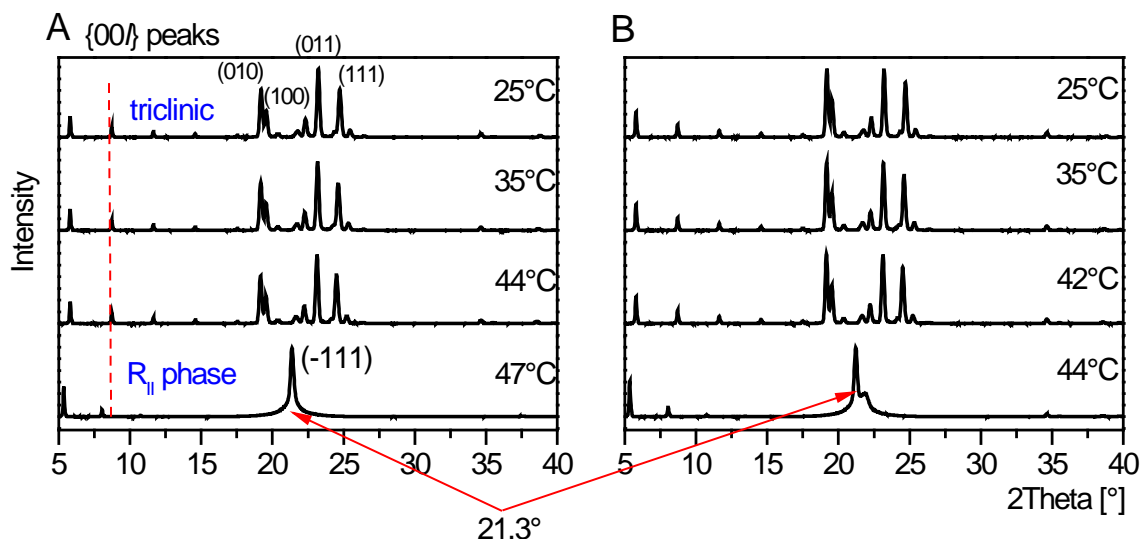


Figure 7.2: $\theta/2\theta$ temperature-dependent scans of bulk *n*-tetracosane, molten at 80 °C on a silicon-wafer, cooled under ambient conditions; A) Heating, B) Cooling.

At lower 2θ values long-spacing $\{00l\}$ reflections with $l = 2-5$ were observed. The reflections are typical for lamellar crystal structures.^{50, 71} Upon heating, the triclinic peaks disappeared whereas a broad single reflection at 21.3° belonging to the (-111) lattice planes emerged. The reflection was indexed based on reference stored in the CDC deposition number ZZZOFC03⁷⁴. In the same temperature range, between 44°C and 47°C , the 2θ lamellar reflections at $5-15^\circ$ shifted to lower values indicating the appearance of the high-temperature R_{II} phase. The occurrence of the rotator phase is in line with results from reference 69.

During the cooling mode (Figure 7.2B), the 21.4° reflection disappeared at 42°C , and then the triclinic phase emerged due to the appearance of the typical reflections. The reverse process, transforming from the R_{II} phase into the triclinic phase, were observed about 4 K lower than the solid/solid transition during heating.

The d -values of the long-spacing $\{00l\}$ layer reflections were estimated with the *Bragg* equation (see Eq. 3.1).

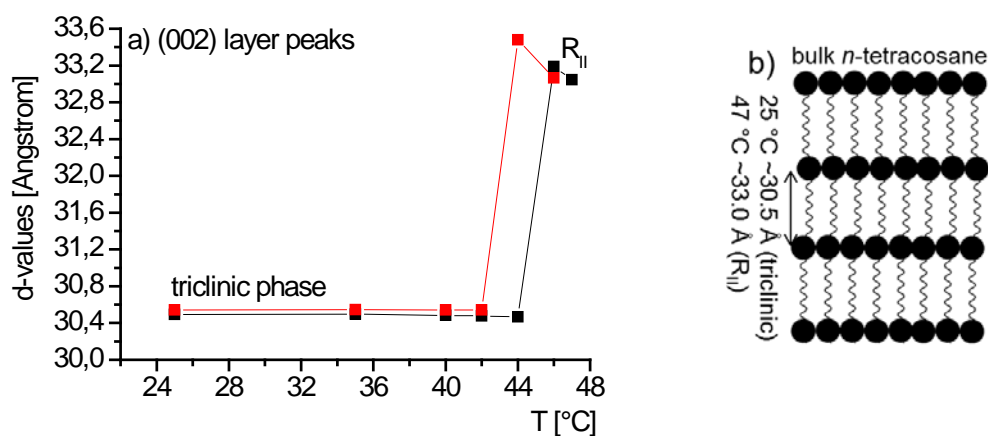


Figure 7.3: d -Values of the (002) layer peaks for bulk n -tetracosane. (a) Heating (black line), Cooling (red line), (b) Schematic view of the layered structures with values of the layer thickness in the triclinic and R_{II} rotator phase.

As can be seen in Figure 7.3a, the layer thickness amounted to approximately 30.5 \AA in the triclinic phase and to $\sim 33 \text{ \AA}$ in the R_{II} phase at 46°C . The interphase transition

triclinic \leftrightarrow R_{II} involves a tilting or vice versa of the molecules that influences the layer thickness. In the R_{II} phase, *n*-tetracosane molecules are non-tilted and hence, the layer thickness increased from ~ 30 Å to 33 Å. Further, the (002) *d*-values displayed hysteresis effects between heating and cooling, indicating that the transformation is hysteretic.

A second DSC heating scan of bulk *n*-tetracosane (Figure 7.4 black line) showed a peak at 49.7 °C ($T_{1\text{peak}}$). The triclinic phase was transformed into the high temperature R_{II} phase, which converted to the liquid phase at 53.1 °C ($T_{2\text{peak}}$). With temperature decreasing (Figure 7.4 blue line) *n*-tetracosane crystallized at 46.7 °C ($T_{3\text{peak}}$) in the R_{II} phase and converted back to the stable triclinic phase at 40.5 °C ($T_{4\text{peak}}$).

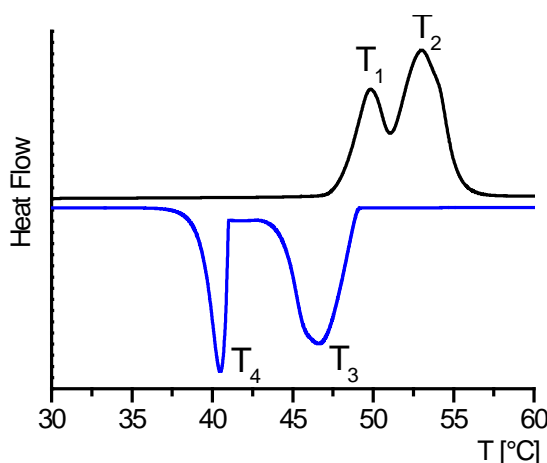


Figure 7.4: Second DSC scans (10 K/min) for bulk *n*-tetracosane; Heating (black line), Cooling (blue line).

Bulk *n*-tetracosane exposed one mesophase referred to as R_{II} phase. Comparison of the two characterization techniques in Figure 7.5 revealed that both detected the transitions triclinic \rightarrow R_{II} and R_{II} \rightarrow melt in the same temperature range only with 2 Kelvin difference. Further, both methods found that the reverse process took place at few Kelvin lower.

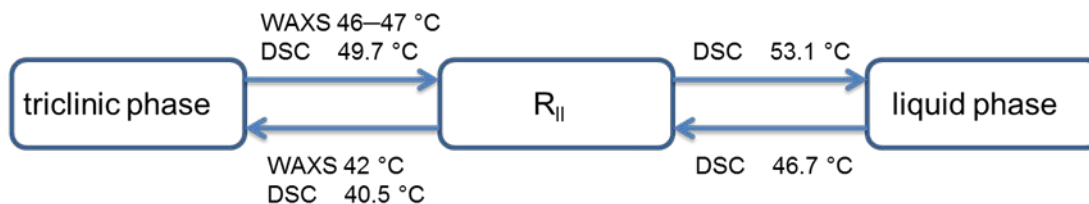


Figure 7.5: Summary of phase transitions during Heating and Cooling of bulk *n*-tetracosane.

7.2 *n*-Tetracosane in AAO Cooled at 0.5 K/min in the Presence of Bulk Material

n-Tetracosane was solidified in anisotropic anodic aluminum oxide (AAO) membranes. The used AAO membranes had pore sizes ranging from 25 nm to 60 nm with pore depth of $\sim 100\ \mu\text{m}$. One AAO membrane series was, before filling with *n*-tetracosane, modified with octadecylphosphonic acid (ODPA). For further information see Chapter 3.1. *n*-Tetracosane in 60 nm AAO was slowly cooled at $-0.5\ \text{K/min}$ in the presence of a bulk surface reservoir. The samples were henceforth referred to as cases A, B, and C. Detailed preparation steps are also found in Chapter 3.1. Before investigations, the bulk surface reservoir was carefully removed. The temperature-dependent $\theta/2\theta$ measurements are shown in Figure 7.6. The red dotted rectangles are illustrated zoomed ranges which are sketched in rows below. The $\theta/2\theta$ patterns revealed a more complex behavior of *n*-tetracosane under confinement than its bulk counterpart. After crystallization, the WAXS patterns were dominated by a reflection at $2\theta = 36.0^\circ$. Apparently, the peak intensity decreased as the temperature increased. Between 35°C and 40°C , a second reflection at $2\theta = 23.4^\circ$ emerged, but completely disappeared when further heated to 46°C . During the cooling scans (Figure 7.7), the main 2θ reflection at 36.0° emerged again. On the other hand, the 2θ peak at 23.4° was not detectable. In AAO membranes with pore sizes of 25 nm a third peak occurred at $2\theta = 21.4^\circ$ and, in the lower 2θ range, weak long-spacing $\{00l\}$ reflections were observed. The lamellar arrangement inside AAO membranes will be discussed in Chapter 7.3.

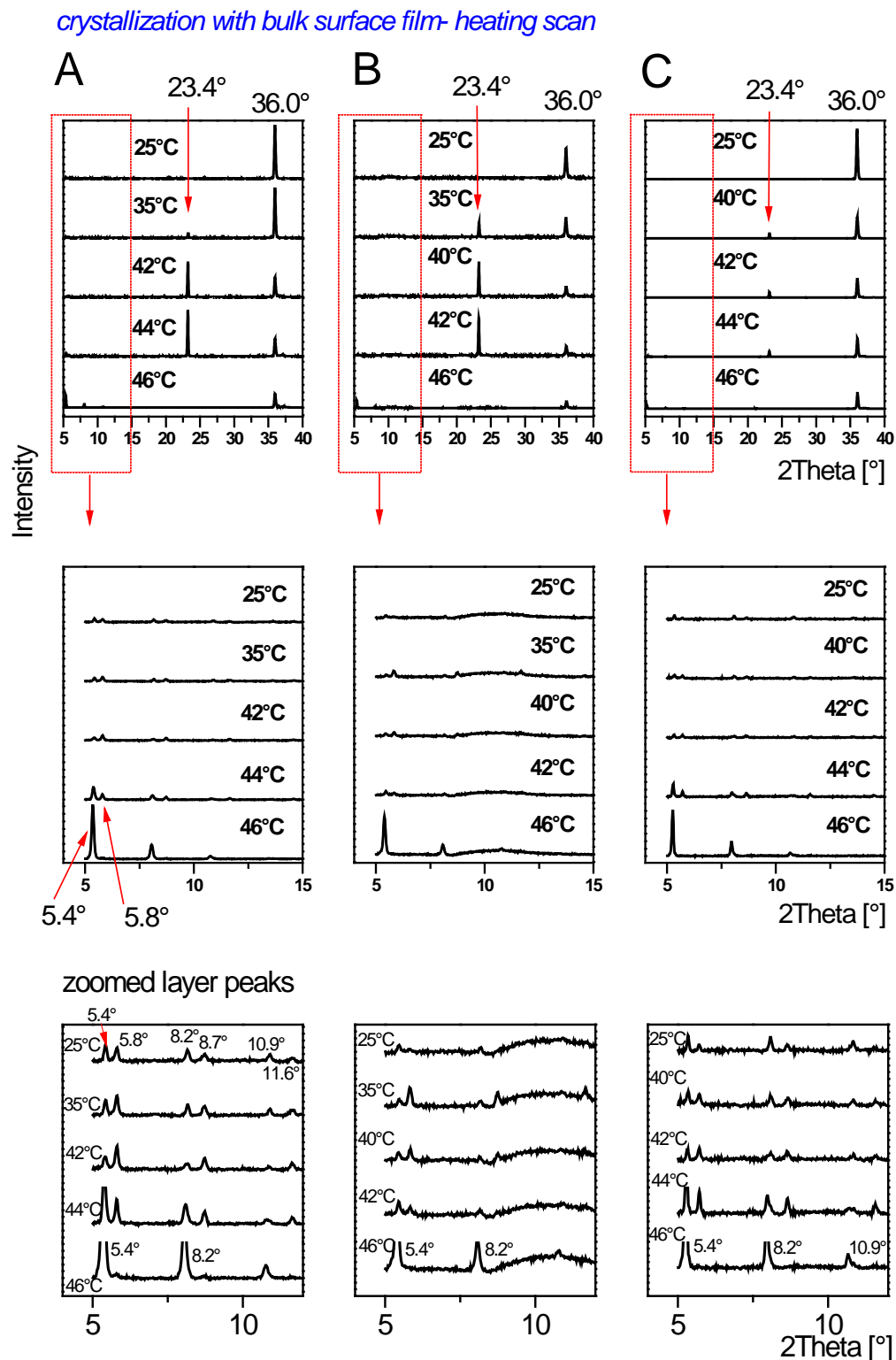


Figure 7.6: $\theta/2\theta$ temperature-dependent heating scans of *n*-tetracosane in AAO cooled at -0.5 K/min in the presence of a bulk surface film, removal of the bulk surface film; A) AAO 60 nm, B) AAO 25 nm, C) AAO 60 nm ODPA-modified. The second and the third rows show zoomed figures.

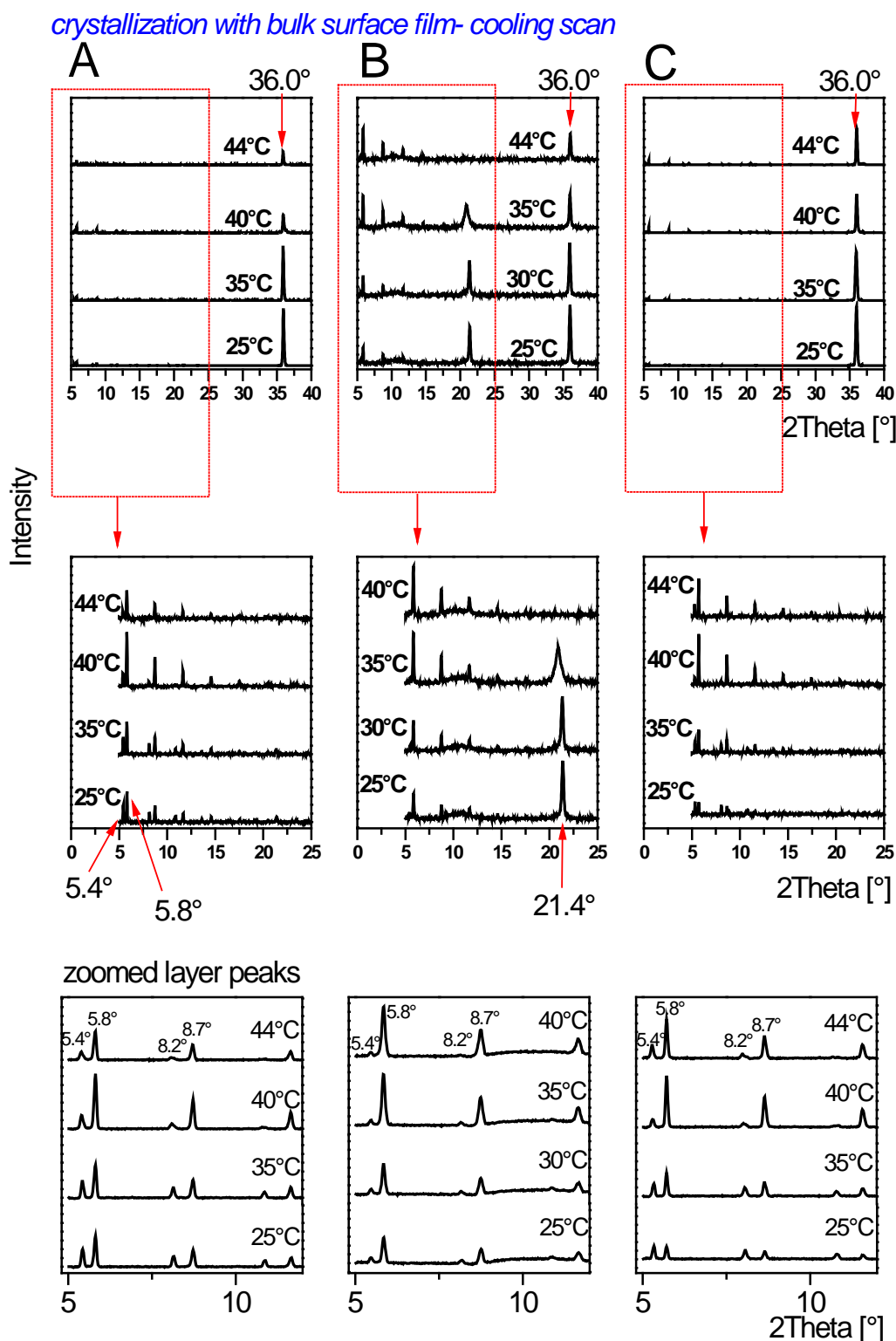


Figure 7.7: $\theta/2\theta$ temperature-dependent cooling scans of *n*-tetracosane in AAO cooled at -0.5 K/min in the presence of a bulk surface film, removal of the bulk surface film; A) AAO 60 nm, B) AAO 25 nm, C) AAO 60 nm ODPA-modified. The second row shows zoomed figures.

Figure 7.8 will have a closer look to the temperature-dependent behavior of the two reflections at $2\theta = 23.3^\circ$ and $2\theta = 36.0^\circ$, respectively. The results will be only discussed for case A corresponding to *n*-tetracosane in AAO with pore sizes of 60 nm cooled at -0.5 K/min in the presence of a bulk surface film.

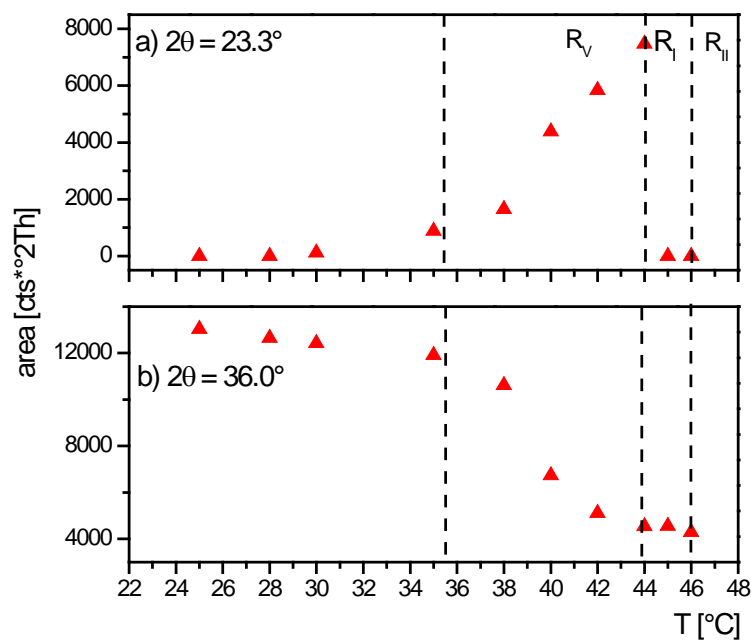


Figure 7.8: Temperature-dependent integrated area as function of the reflections (a) at $2\theta = 23.3^\circ$, (b) at $2\theta = 36.0^\circ$ for 60 nm AAO (corresponding to case A in Figure 7.6). Phase transitions are indicated by dotted lines.

As can be seen in Figure 7.8a, the peak areas as function of the 23.3° peak increased between 36°C and 44°C . In contrast, the peak areas of the 36.0° peak decreased in the same temperature range (Figure 7.8b). In both figures, rotator phases are indicated with dotted lines according to reference 69. Rotator phase R_V occurred between 35°C and 44°C , R_I in the shorter temperature range $44\text{--}46^\circ\text{C}$, and R_{II} was detected at 46°C . For orientation distribution measurements Schulz scans were performed and shown in Figure 7.9a. The measured Schulz scan at a fixed angle of 36.0° corresponded to the (-111) triclinic lattice planes according to CSD deposition number ZZZOFC04⁷². In the mesophase R_V , between 35°C and 40°C , the 2θ peak at 36.0° may correspond to the

(020) lattice planes according to CSD deposition number ZZZOFC based on reference 74. At 46 °C, in the R_{II} phase, the peak intensity at $2\theta = 36.0^\circ$ decreased. Note *n*-tetracosane in the R_{II} phase shows no reflection at $2\theta \sim 36.0^\circ$ according to the stored CSD deposition number ZZZOFC03.

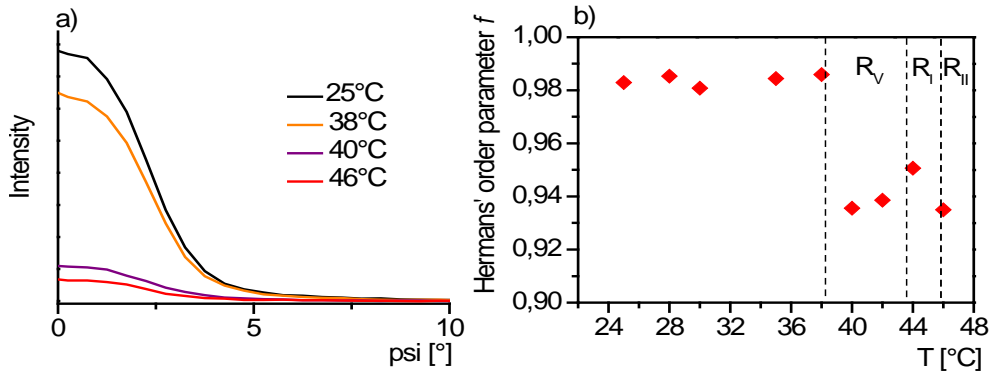


Figure 7.9: Texture analysis of *n*-tetracosane in 60 nm AAO (corresponding to case A in Figure 7.6) prepared by crystallization with bulk surface film measured at the fixed angle of 36.0° , (a) ψ scans, (b) Hermans' order parameter f ⁹¹.

The orientation distribution of the triclinic (-111) lattice planes ($2\theta = 36.0^\circ$) revealed pronounced maxima at $\psi \sim 0^\circ$ (Figure 7.9). The calculated Hermans' order parameter amounted to 1 indicating that the (-111) lattice planes preferentially oriented parallel to the AAO membrane surface. When heated to 38 °C, the maxima at $\psi = 0^\circ$ decreased and hence, the calculated f values in Figure 7.9b decreased, too. The phase transitions sequence $R_V \rightarrow R_I \rightarrow R_{II}$ (black dotted lines) is in line with results as shown in Figure 7.8.

Schulz scans in Figure 7.10a at the fixed angle of 21.4° corresponded to the triclinic (013) lattice planes. The theoretical angle of 35.7° (black dotted line in Figure 7.10a) between the (-111) and (013) triclinic lattice planes was estimated with data from CSD deposition number ZZZOFC04. The $I(\psi)$ profile of the (013) lattice planes ($2\theta = 21.4^\circ$) exhibited a maximum at $\psi \sim 34^\circ$. At 40 °C in a mesophase, the 2θ reflection at 21.4° belonged to the (-111) lattice planes. The theoretical angle between the (020) $2\theta = 36.0^\circ$ and (-111) $2\theta = 21.4^\circ$ lattice planes is 33.9° . The Schulz scan belonging to the (-111) reflection showed a little shift to lower peak values ($\psi \sim 33^\circ$) at 40 °C.

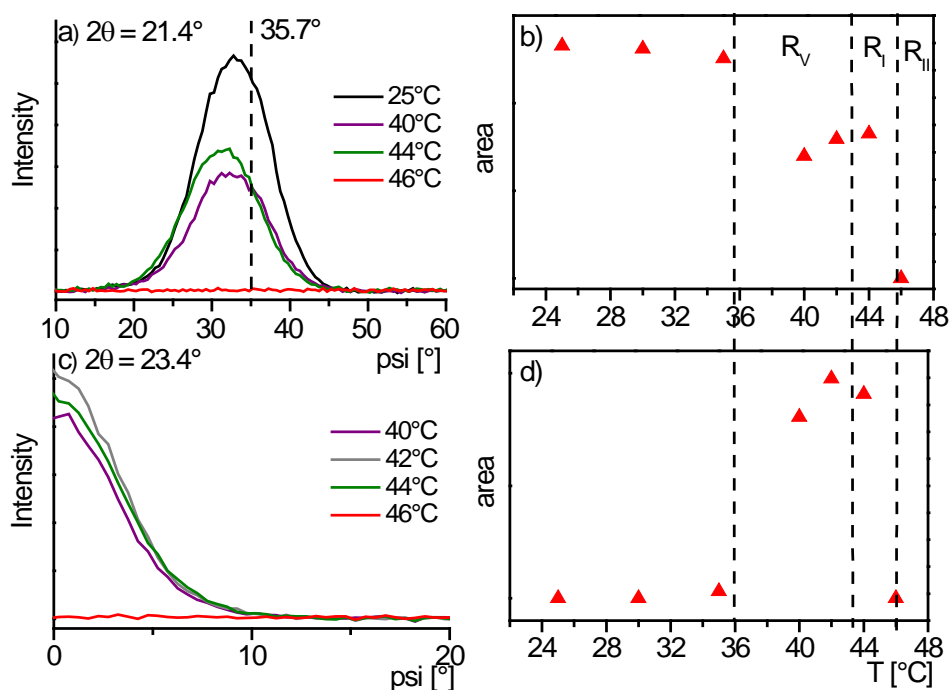


Figure 7.10: Texture analysis of *n*-tetracosane in 60 nm AAO (case A in Figure 7.6) prepared by crystallization with bulk surface film measured at the fixed angle, (a) of 21.4° ψ scans, (b) 21.4° temperature-dependent area of the ψ scans, (c) of 23.4° ψ scans, (d) 23.4° temperature-dependent area of the ψ scans. The theoretical angle between (-111) and (013) lattice planes is indicated with a dotted line.

The measured peak areas corresponding to the 2θ reflection at 21.4° (Figure 7.10b) showed the highest values in the triclinic phase between 25 °C and 35 °C. Further, the peak areas are stepped down, held constant until 44 °C (R_V phase) and decreased to zero at 46 °C ($R_I \rightarrow R_{II}$ phase transition).

The measured peak areas for the 2θ peak at 23.4° had their maximum at 42 °C in the R_V rotator phase (Figure 7.10d). At 46 °C, in the R_{II} phase, the 23.4° reflection disappeared completely. Therefore, the peak at 23.4° was indexed as the (311) lattice planes⁷⁴ belonging to a mesophase.

7.3 Lamellar Crystals of *n*-Tetracosane in AAO Membranes

The next topic will go back to the temperature-dependent $\theta/2\theta$ measurements for *n*-tetracosane as shown in the Figure 7.6. The zoomed ranges showed weak long-spacing $\{00l\}$ reflections in the lower 2θ range. It should be kept in mind that bulk *n*-tetracosane had typical triclinic layer reflections which shifted to lower 2θ values in the R_{II} phase at 46 °C (Figure 7.2).

n-Tetracosane in 25 nm AAO cooled at a rate of -0.5 K/min in the presence of a bulk surface reservoir showed phase transitions and long-spacing $\{00l\}$ reflections, as seen in Figure 7.11. Firstly, in the triclinic phase, the pattern is dominated by a 2θ reflection at 36.0°. At 35 °C, a second reflection at 23.4° emerged belonging to the (311) lattice planes in the R_V rotator phase. Weak triclinic long-spacing $\{00l\}$ reflections were observed until 44 °C. At the same temperature, the relative intensities of the (00 l) peaks increased.

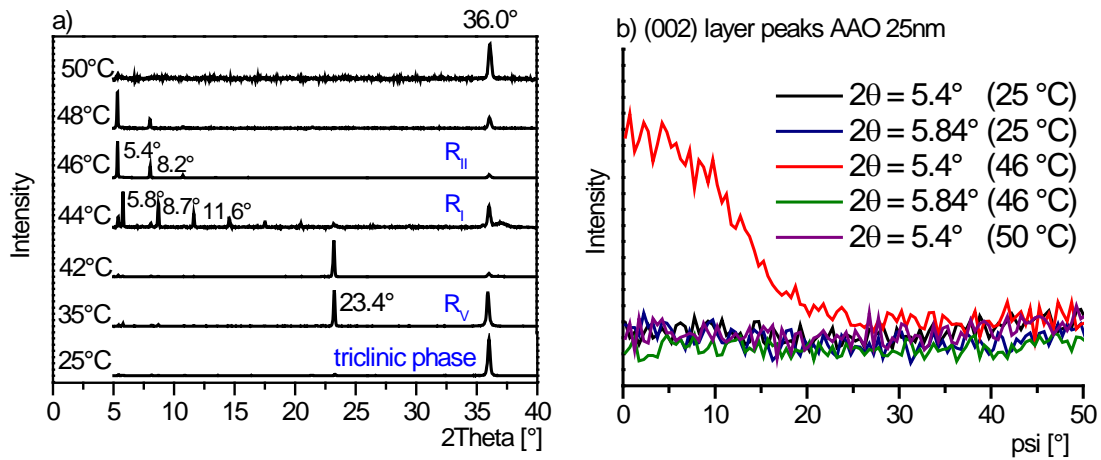


Figure 7.11: *n*-Tetracosane in 25 nm AAO cooled at -0.5 K/min in the presence of a bulk surface reservoir, removal of the bulk surface film; (a) $\theta/2\theta$ temperature-dependent heating scans, phase transitions are ordered for increasing temperatures. (b) temperature-dependent Schulz scans, $2\theta = 5.84^\circ$ corresponds to the (002) triclinic lattice planes, $2\theta = 5.4^\circ$ corresponds to the (002) orthorhombic lattice planes.

At 44 °C, triclinic and high temperature {00*l*} reflections occurred together in AAO membranes. Further, the peak intensities of the 2θ = 23.4° and of the 36.0° reflections decreased. Finally, at 48 °C, R_{II} long-spacing {00*l*} reflections were visible until melting. In the cooling run, the long-spacing {00*l*} reflections were not observed.

Schulz scan corresponding to the triclinic (002) lattice planes ($2\theta \sim 5.8^\circ$) showed no maximum at $\psi = 0^\circ$ (Figure 7.11b). On the other hand, at 46°C , the $I(\psi)$ profile belonging to the orthorhombic (002) lattice planes ($2\theta = 5.4$) exhibited a weak maximum at $\psi \sim 0^\circ$.

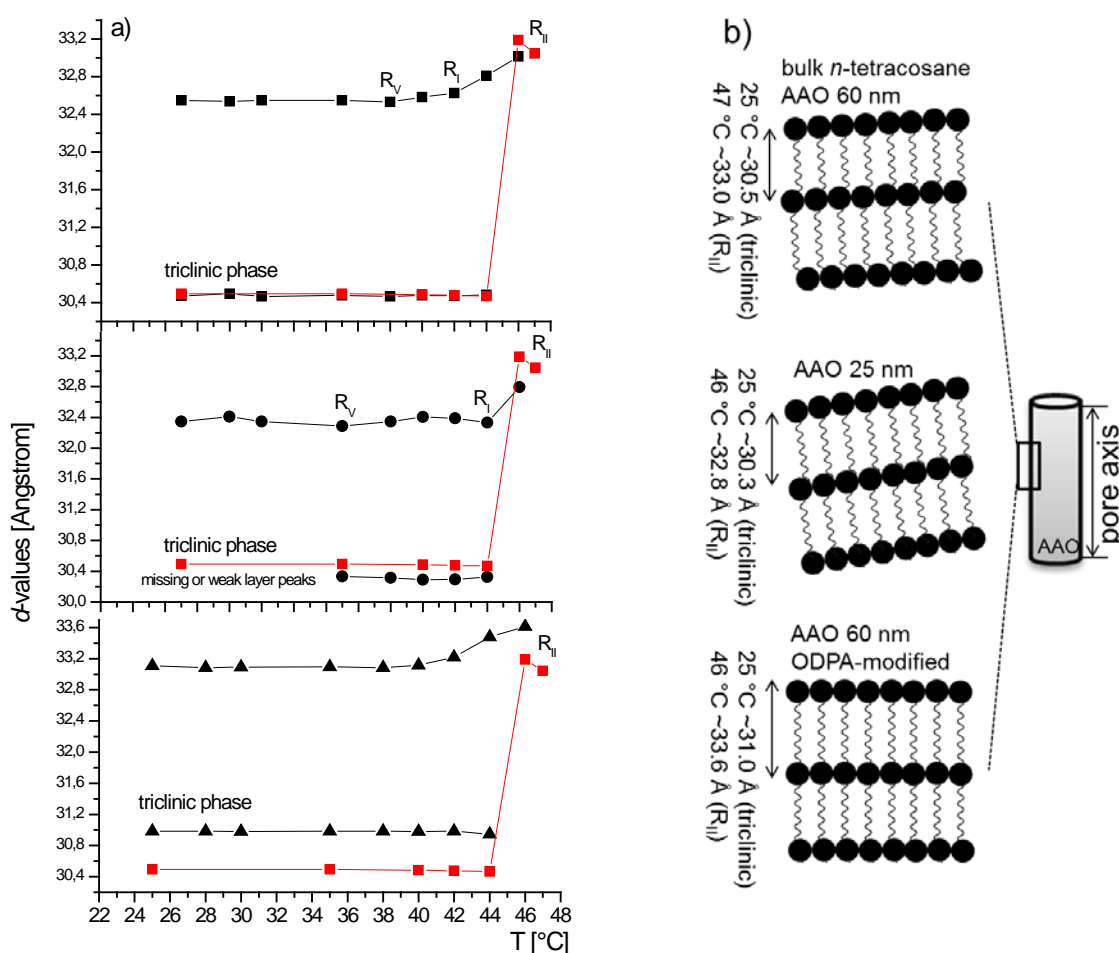


Figure 7.12: *n*-Tetracosane confined to AAO membranes; (a) *d*-values of (002) layer peaks for —■— bulk *n*-tetracosane, —■— AAO 60 nm, —●— AAO 25 nm, —▲— AAO 60 nm ODPa-modified. (b) Schematic view of the layered structures for bulk material and *n*-tetracosane in AAO membranes where lamellar layers are oriented normal to the AAO pore axis.

Estimated d -values of the $\{00l\}$ long-spacing layer reflections of 60 nm, 25 nm, and 60 nm ODPa-modified AAO samples are summarized in Figure 7.12. Values for bulk *n*-tetracosane (red rectangle) are shown for comparison. For triclinic *n*-tetracosane in 60 nm AAO d -values amounted to 30.5 Å (Figure 7.12a black rectangle). Between 40 °C and 44 °C, d -values amounted to 32.5 Å assuming that not the orthorhombic R_{II} layer arrangement occurred but rather R_V and/or R_I rotator phases. Between 44 °C and 46 °C in the R_{II} rotator phase, the d -values increased to 33.0 Å.

In 25 nm AAO membranes d -values amounted to 30.3 Å and are slightly lower than for bulk material (bulk d -values = 30.5 Å). At 44 °C, layer thickness increased from 32.3 Å to 32.8 Å (Figure 7.12a black circle). *n*-Tetracosane in AAO membranes with ODPa modified pore walls (Figure 7.12a black triangle) showed layer thicknesses of around 31 Å in the triclinic (bulk d -values = 30.5 Å) and 33.6 Å (bulk d -values = 33.2 Å) in the orthorhombic R_{II} phase. A schematic view of the layer structures is given in Figure 7.12b. The results will be discussed in Chapter 7.8.3.

7.4 *n*-Tetracosane in AAO Cooled at 0.5 K/min in Absence of Bulk Material

Infiltrated *n*-tetracosane in AAO membranes were cooled from 80°C to room temperature at -0.5 K/min in the absence of a bulk surface reservoir. The samples were referred to as cases D, E, and F (Table 3.2), preparation details are given in Chapter 3.1. *n*-Tetracosane confined in 25 nm and 60 nm AAO membranes showed a dominant peak at $2\theta = 21.4^\circ$. The peak was indexed as the triclinic (013)⁷² or the (-111)⁷⁴ lattice planes belonging to a mesophase (Figure 7.13). The peak intensity of the 21.4° reflection decreased when heated up to 40°C. Moreover, the peak shape became broader and peak maxima shifted to lower 2θ -values.

In all three samples (i.e., 25 nm, 60 nm, or 60 nm ODPa-modified AAO membranes) a peak at $2\theta = 36.0^\circ$ occurred. The peak only dominated the patterns of *n*-tetracosane in AAO membranes with ODPa modified pore walls. On the other hand, the 36.0°

reflection was detectable in the temperature range from 25 °C to 40 °C independently of the AAO pore size or the pore wall modification. As previously mentioned, the peak belongs to the triclinic (-111)⁷² lattice planes at 25 °C and to the (020)⁷⁴ lattice planes in a rotator phase at ~35 °C. Additional peaks emerged at $2\theta = 19.3^\circ$ and at 23.4° , respectively.

During cooling scans (Figure 7.14), the 2θ peak at $2\theta = 36.0^\circ$ emerged again but showed, in all investigated samples, hysteresis effects. At 25 °C, the WAXS patterns were dominated by the $2\theta = 36.6^\circ$ peak. At $2\theta = 21.4^\circ$ a weak peak was observed. Last point to mention is that *n*-tetracosane in AAO cooled at -0.5 K/min in the absence of a bulk surface reservoir showed no evidence of layer reflection in the used $\theta/2\theta$ geometry. No reflections at lower 2θ values were observed, not in the heating neither in the cooling scans.

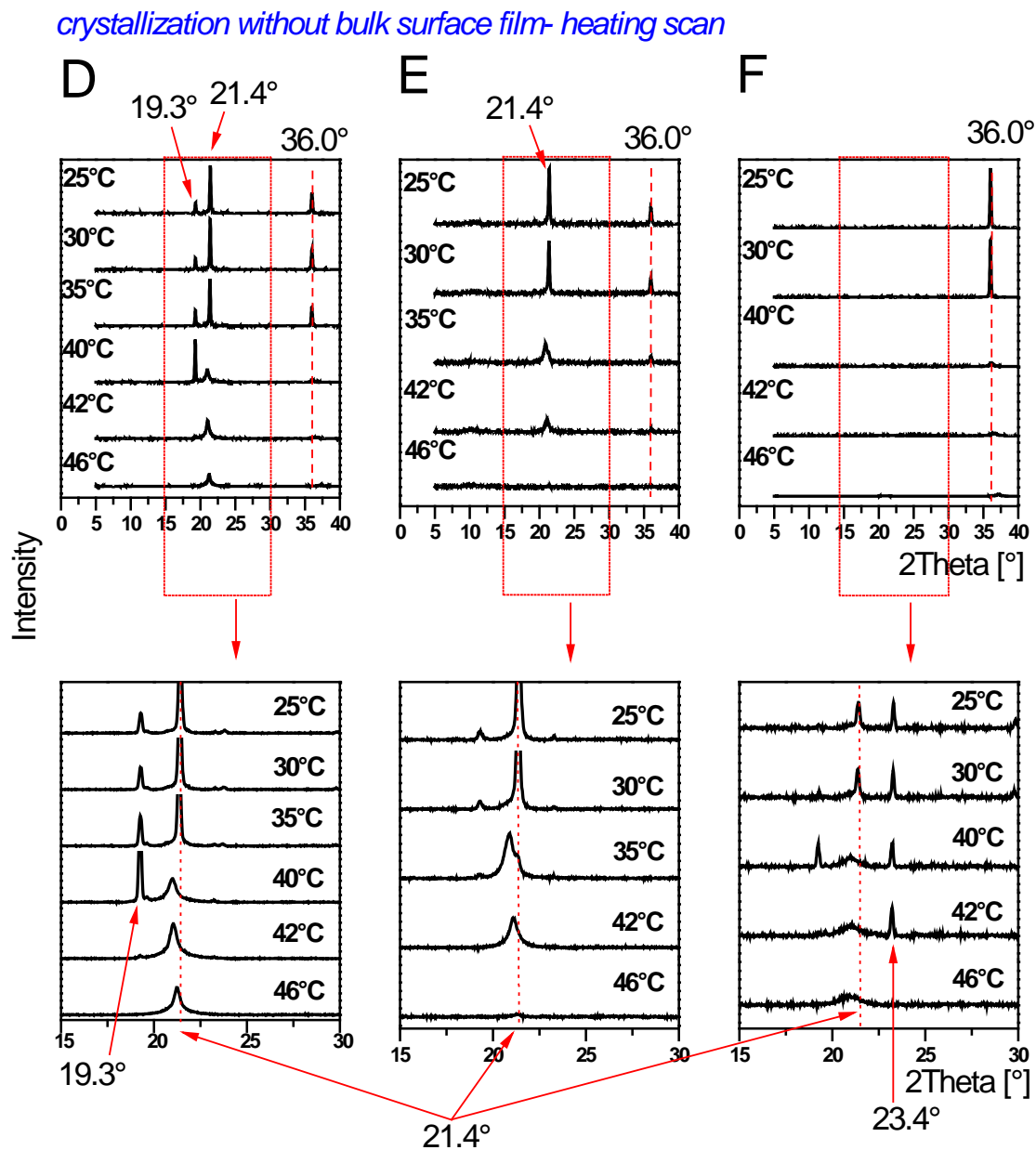


Figure 7.13: $\theta/2\theta$ temperature-dependent heating scans of *n*-tetracosane in AAO cooled at -0.5 K/min in the absence of a bulk surface film; D) AAO 60 nm, E) AAO 25 nm, F) AAO 60 nm ODPA-modified. The second row shows zoomed figures.

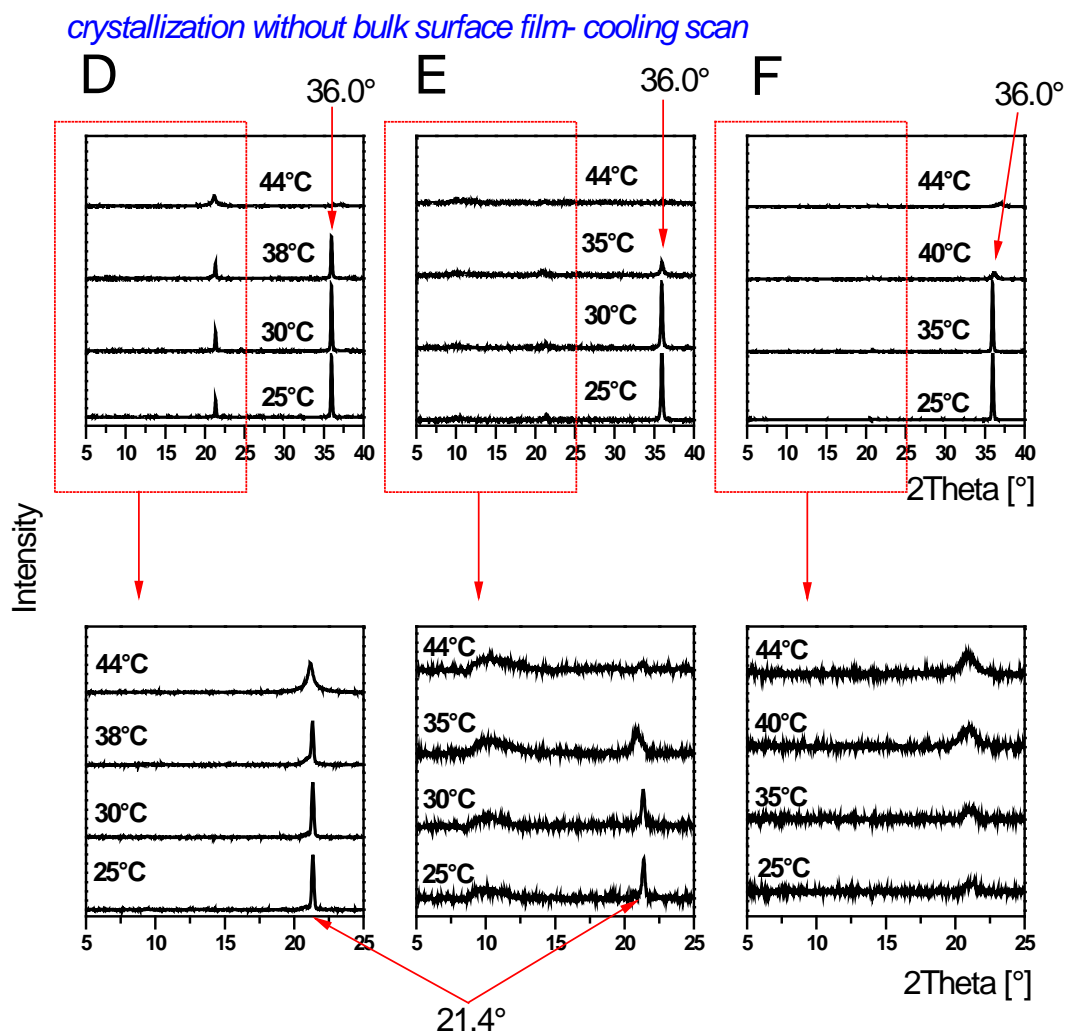


Figure 7.14: $\theta/2\theta$ temperature-dependent cooling scans of *n*-tetracosane in AAO cooled at -0.5 K/min in the absence of a bulk surface film; D) AAO 60 nm, E) AAO 25 nm, F) AAO 60 nm ODPA-modified. The second row shows zoomed figures.

The orientation distribution of a set of lattice planes belonging to the above-mentioned characteristic reflections was obtained by Schulz scans. The (-111) lattice planes ($2\theta = 36.0^\circ$) of *n*-tetracosane in 60 nm AAO crystallized at a cooling rate of -0.5 K/min without bulk surface reservoir had narrow orientation distribution with respect to the AAO membrane surface. This is obvious from the maximum at $\psi = 0^\circ$ at 25°C (Figure 7.15a). The estimated Hermans' order parameters f^{91} amounted to ~ 0.96 (Figure 7.15b).

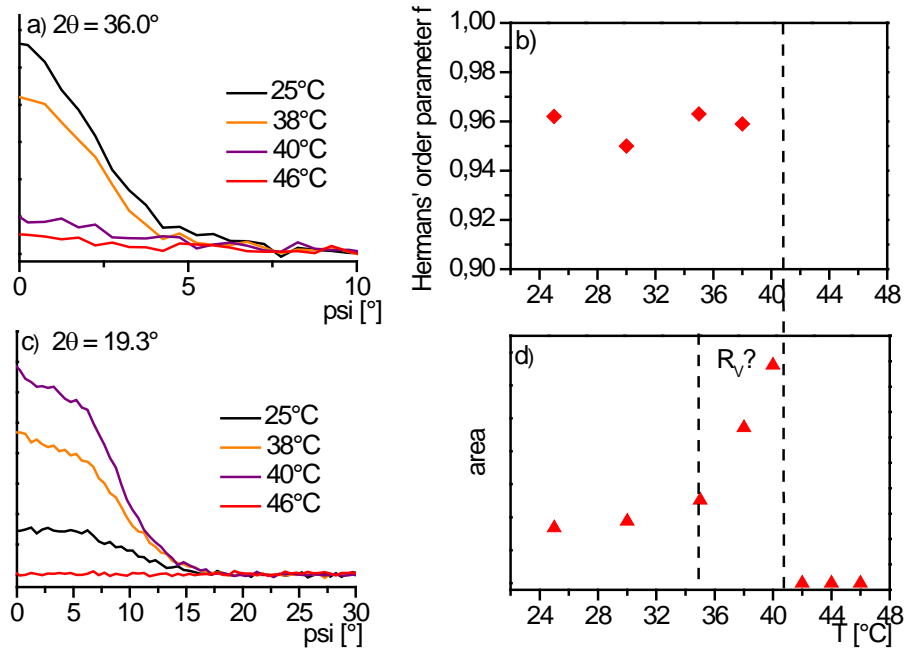


Figure 7.15: Texture analysis of *n*-tetracosane in 60 nm AAO (case D in Figure 7.13) cooled at -0.5 K/min in the absence of a bulk surface reservoir; (a) measured at the fixed angle of 36.0° ψ scans, (b) Hermans' order parameter f^{91} , (c) measured at the fixed angle 19.3° ψ scans, (d) temperature-dependent area of the ψ scans.

Apparently, the $I(\psi)$ profiles intensities at $\psi \sim 0^\circ$ belonging to the (-111) reflection decreased when the temperature increased from 25°C to 40°C (Figure 7.15a). The peak at $2\theta = 19.3^\circ$ (Figure 7.15c) showed an intensity increasing at $\psi \sim 0^\circ$ in the same temperature range. At 40°C , the $2\theta = 19.3^\circ$ reflection reached a maximum. Above 40°C , the $I(\psi)$ profiles or the estimated area showed a sharp decreasing as can be seen in Figure 7.15c/d. The 2θ peak at 19.3° is a typical triclinic reflection corresponding to the (010) lattice planes, but might also belong to a mesophase.

7.5 *n*-Tetracosane in CPG Cooled at 0.5 K/min

As the crystallization experiments of acetaminophen from Chapter 5.5.3 showed, the pore morphology of nanoporous matrices was an important tool to control the nucleation and crystal growth mechanism. Crystallization in anodic aluminum oxide (AAO) offered different crystal growth paths than in controlled porous glasses (CPG). In the first part of the study, *n*-tetracosane was confined in anisotropic AAO membranes. Now, in the forthcoming chapters, *n*-tetracosane is crystallized in isotropic CPG membranes. Therefore, infiltrated *n*-tetracosane in 2 nm, 25 nm, and 60 nm CPG was cooled at a cooling rate of -0.5 K/min in the presence (cases G–I) or in the absence of a bulk surface reservoir (cases J–L in Table 3.2).

The crystal texture of *n*-tetracosane in CPG non-isothermally crystallized (Figure 7.16) showed different $2\theta/2\theta$ patterns compared to *n*-tetracosane in AAO membranes (Figure 7.6 or Figure 7.13). The dominant 2θ peak at 36.0° of nanosized *n*-tetracosane in AAO membranes was missed in CPG samples. Further, in 60 nm and 25 nm CPG membranes, the reflection at $2\theta = 21.4^\circ$ emerged as main peak. In the 2θ range $23\text{--}24^\circ$ weak peaks were observed. It is remarkable that *n*-tetracosane in 25 nm and 60 nm CPG membranes showed long-spacing $\{00l\}$ reflections. The occurrence of the layered structures seems to be related to the availability of bulk *n*-tetracosane surface material during cooling. Lamellar crystals were only observed when *n*-tetracosane was crystallized in the presence of a bulk surface reservoir.

In CPG membranes with pore sizes of 2 nm no crystalline reflections occurred neither in the presence either in the absence of a bulk surface reservoir. Crystalline structures are suppressed. During the cooling scans, no reflections were measured in such small pore sizes (Figure 7.17). On the other hand, in 60 nm and 25 nm CPG membranes the 2θ peak at 21.4° emerged again during cooling.

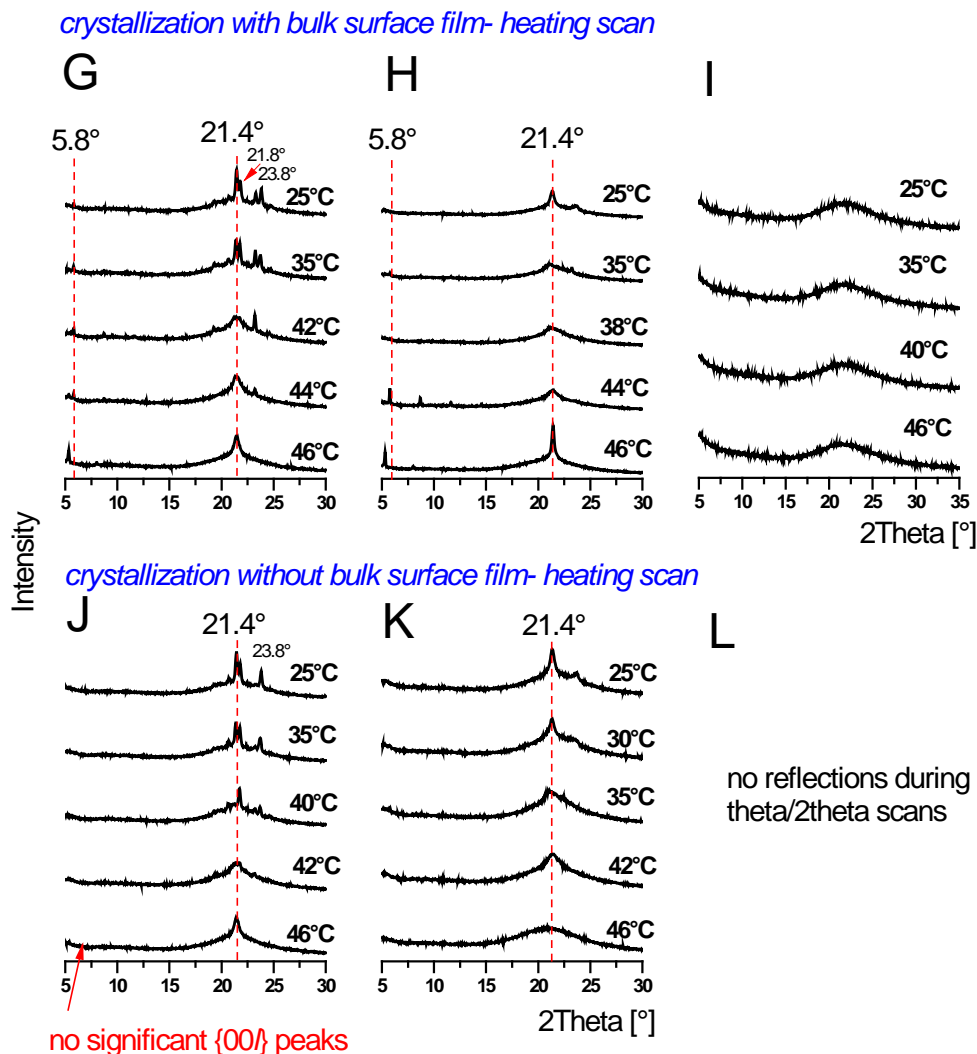


Figure 7.16: $\theta/2\theta$ temperature-dependent heating scans of *n*-tetracosane in; G) CPG 60 nm, H) CPG 25 nm, I) CPG 2 nm and cooled at -0.5 K/min in the presence of a bulk surface reservoir. J) CPG 60 nm, K) CPG 25 nm, L) CPG 2 nm and cooled at -0.5 K/min in the absence of a bulk surface reservoir. Note the amorphous halo that can be seen around $2\theta = 22^\circ$ is originating from the CPG matrix. *n*-Tetracosane in 2 nm CPG revealed no reflections.

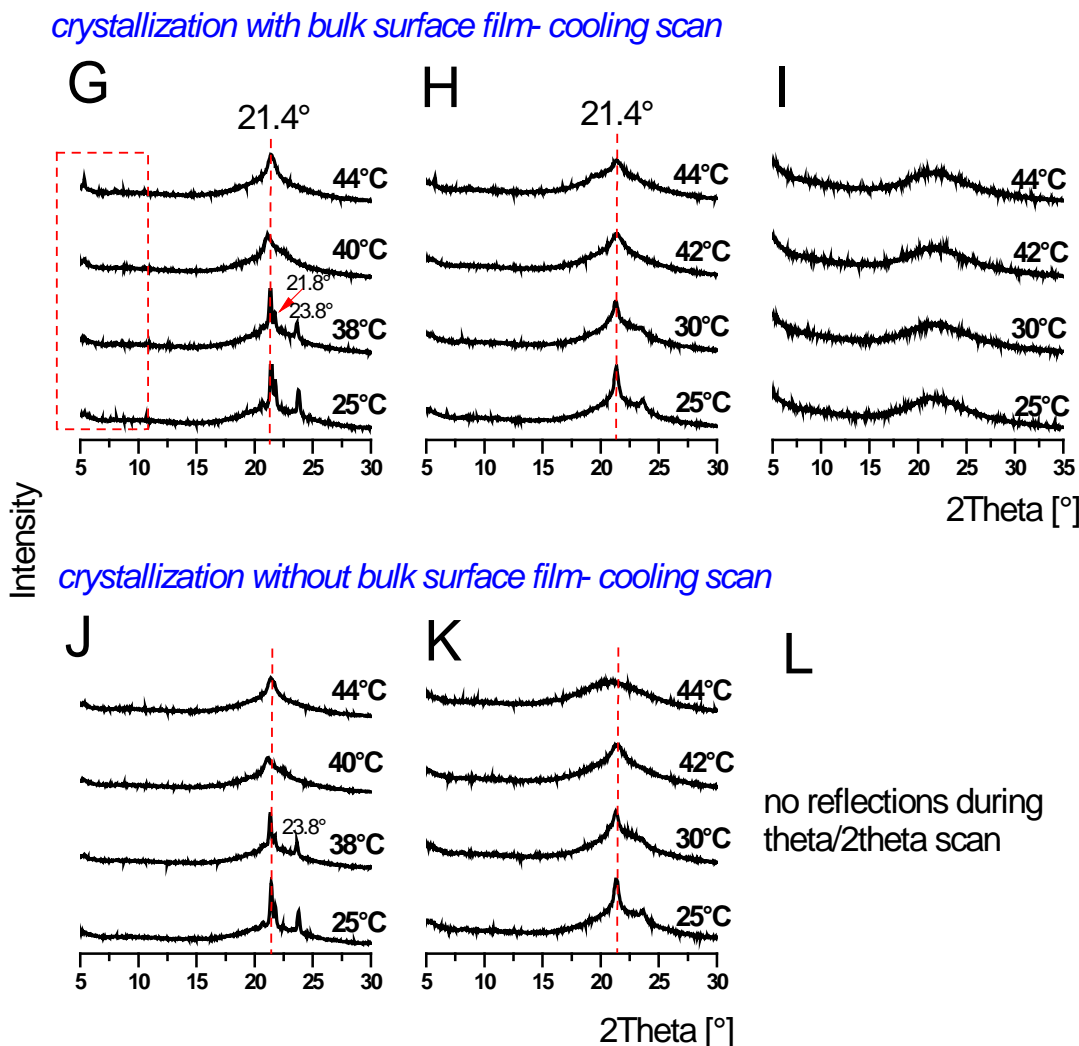


Figure 7.17: $\theta/2\theta$ temperature-dependent cooling scans of *n*-tetracosane in; G) CPG 60 nm, H) CPG 25 nm, I) CPG 2 nm and cooled at -0.5 K/min in the presence of a bulk surface reservoir. J) CPG 60 nm, K) CPG 25 nm, L) CPG 2 nm and cooled at -0.5 K/min in the absence of a bulk surface reservoir.

As previously described, *n*-tetracosane in 25 nm CPG crystallized at a cooling rate of -0.5 K/min in the presence of a bulk surface reservoir yielded a triclinic main peak at $2\theta = 21.4^\circ$ (Figure 7.16 case H or Figure 7.18a). At 42°C , the peak widths became broader which may indicate the R_V rotator phase. Triclinic long-spacing $\{00l\}$ reflections occurred in the temperature range between 44°C and 46°C . Above 46°C , the peak maxima shifted to lower 2θ values indicating the R_{II} rotator phase. At the same

temperature the 21.4° peak disappeared. Estimated layer thicknesses amounted to 31 Å at 44 °C and to 33.2 Å at 48 °C, respectively (Figure 7.18b).

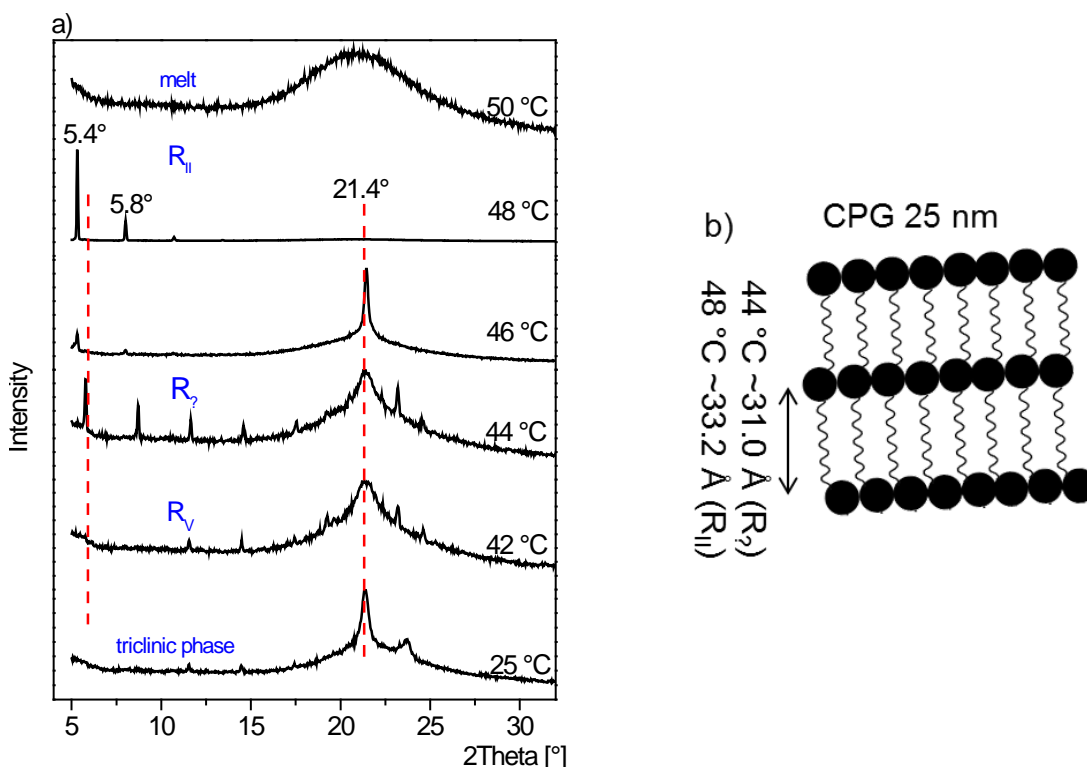


Figure 7.18: *n*-Tetracosane in 25 nm CPG corresponding to sample H cooled at -0.5 K/min in the presence of a bulk surface reservoir; (a) $\theta/2\theta$ scans, (b) d -values and schematic view of the lamellar layers.

7.6 Thermal Analysis of *n*-Tetracosane in Nanoporous Matrices

To support WAXS results thermal measurements were performed. One sample set was used for temperature-dependent X-ray studies as shown in chapters 7.2–7.4, the other set was used for DSC analysis. Figure 7.19 shows the first DSC heating scans (solid black lines) and first cooling scans (solid blue lines) of *n*-tetracosane in 25 nm, 60 nm, and 60 nm ODPA-modified AAO membranes, respectively. Lines a–c correspond to *n*-tetracosane samples crystallized at a cooling rate of -0.5 K/min in the presence of a

bulk surface reservoir. Lines d–f represent samples which were cooled at a rate of -0.5 K/min in the absence of a bulk surface reservoir.

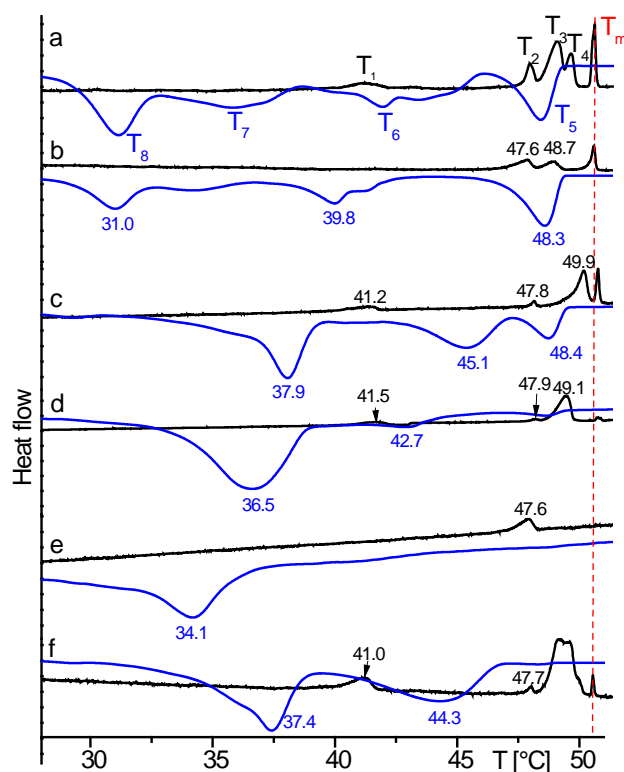


Figure 7.19: First DSC scans (10 K/min) of *n*-tetracosane in; (a) AAO 60 nm, (b) AAO 25 nm, (c) AAO 60 nm ODPA-modified and crystallized at a cooling rate of -0.5 K/min in the presence of a bulk surface reservoir, (d) AAO 60 nm, (e) AAO 25 nm, (f) AAO 60 nm ODPA-modified and crystallized at a cooling rate of -0.5 K/min in the absence of a bulk surface reservoir. Heating scan (black line), Cooling scan (blue line).

n-Tetracosane in 60 nm AAO crystallized with bulk surface reservoir (Figure 7.19 black line a) showed five endothermic peaks. The first small one emerged at 40.9 °C and indicated the interphase transition triclinic \rightarrow R_V. The next three peaks appeared at $T_{2\text{peak}} = 47.7$ °C (R_V \rightarrow R_I transition), $T_{3\text{peak}} = 48.7$ °C (R_I \rightarrow R_{II} transition), and $T_{4\text{peak}} = 49.3$ °C (R_{II} \rightarrow melt), respectively. The classifications of the transitions are taken from references 51, 69. The red line with the melting point at $T_{m,\text{peak}} \sim 50.3$ °C marked the bulk melting point of *n*-tetracosane.

The cooling process (Figure 7.19 solid blue line a) displayed four exothermic peaks. The first occurred at $T_{5\text{peak}} = 48.1\text{ }^{\circ}\text{C}$ where the melted material converted into the rotator phase R_{II} . The next peaks were observed at $41.7\text{ }^{\circ}\text{C}$ ($T_{6\text{peak}}$) and $35.7\text{ }^{\circ}\text{C}$ ($T_{7\text{peak}}$), respectively. The peaks belonged to interphase transitions. The last huge peak at $31.1\text{ }^{\circ}\text{C}$ ($T_{8\text{peak}}$) was the transformation into the stable triclinic phase.

Lines b and c in Figure 7.19 show results of *n*-tetracosane in 25 nm and 60 nm ODPa-modified AAO membranes crystallized in the presence of bulk surface material. Both samples had an endothermic peak around $47\text{ }^{\circ}\text{C}$ and a bulk melting peak indicated with a red dotted line. In 25 nm AAO membranes the endothermic peak at $\sim 41\text{ }^{\circ}\text{C}$ was not observed. DSC measurements revealed that the transformation temperature $R_{\text{II}} \rightarrow \text{triclinic}$ shifted from $31\text{ }^{\circ}\text{C}$ in 60 nm AAO to $38\text{ }^{\circ}\text{C}$ in 60 nm ODPa-modified AAO membranes (Figure 7.19 blue lines a and c).

n-Tetracosane in AAO membranes crystallized in the absence of a bulk surface reservoir showed less peaks (Figure 7.19 lines d–f). This observation may relate to the availability of bulk surface reservoir during crystallization. The bulk surface material may have an impact on the occurrence of phase transitions under confinement. A closer discussion is given in Chapter 7.8.

DSC heating and cooling scans of *n*-tetracosane in CPG membranes non-isothermally crystallized at a cooling rate of -0.5 K/min in the presence or in the absence of bulk material are shown in Figure 7.20. The bulk melting point at $\sim 50.4\text{ }^{\circ}\text{C}$ was indicated with a red dotted line. The heating scans of *n*-tetracosane in 25 nm CPG (Figure 7.20 solid black lines a/c) showed two endothermic peaks around $47\text{ }^{\circ}\text{C}$. In smaller pore sizes ($d = 2\text{ nm}$) a weak endothermic peak occurred at $\sim 48\text{ }^{\circ}\text{C}$. During temperature decreasing, the liquid phase converted back in the R_{II} phase at $\sim 48.5\text{ }^{\circ}\text{C}$. At lower temperature, between $40\text{ }^{\circ}\text{C}$ and $41\text{ }^{\circ}\text{C}$, the transition into the triclinic phase was seen.

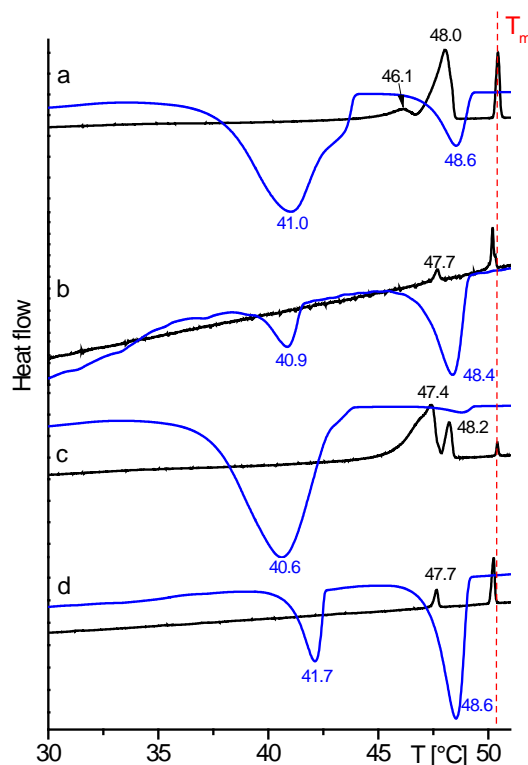


Figure 7.20: First DSC scans (10 K/min) of *n*-tetracosane in; (a) CPG 25 nm, (b) CPG 2 nm and non-isothermally crystallized at a cooling rate of -0.5 K/min in the presence of a bulk surface reservoir, (c) CPG 25 nm, (d) CPG 2 nm and non-isothermally crystallized at a cooling rate of -0.5 K/min in the absence of a bulk surface reservoir. Heating scan (black line), Cooling scan (blue line).

7.7 Aging Behavior of *n*-Tetracosane in AAO Membranes

The results revealed that the crystallization of *n*-tetracosane in AAO membranes was influenced by the crystallization parameters. Therefore, the stability of nanosized structures and their long-life storage are important aspect in the research field. An open question is the aging behavior of nanosized material. Does a molecule rearrangement i.e., change in the $\theta/2\theta$ patterns occur over the storage time? For this purpose *n*-tetracosane in 60 nm AAO cooled at a rate of -0.5 K/min (a) in the presence (Ch. 7.2) or (b) in the absence of a bulk surface reservoir (see Ch. 7.4) has been investigated.

Before WAXS measurements the surface material was carefully removed. First theta/2theta scans were measured two days after infiltration and crystallization.

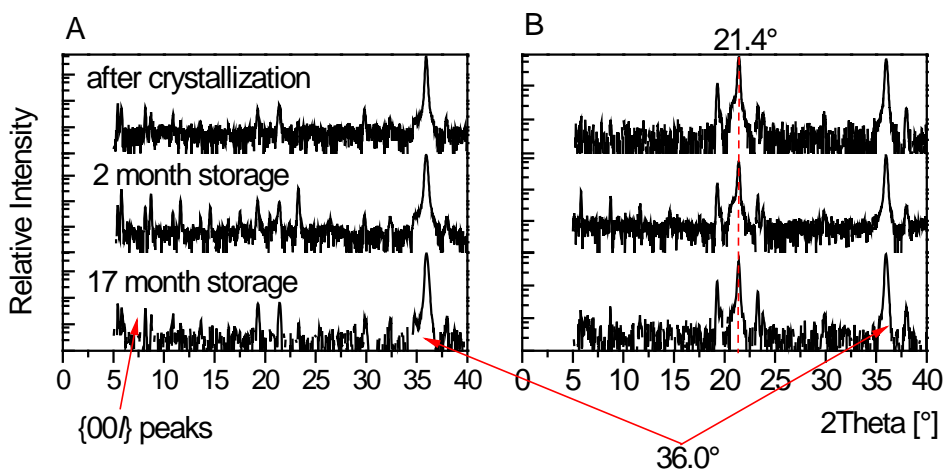


Figure 7.21: Long-time storage of *n*-tetracosane in 60 nm AAO membranes cooled at -0.5 K/min; A) in the presence of a bulk surface reservoir, B) in the absence of a bulk surface reservoir. Note for better visualization the y axis is logarithmic.

The collected theta/2theta patterns in Figure 7.21 are in line with samples prepared in former sections; case A in Figure 7.6 and case D in Figure 7.13, respectively. After the first measurements the samples were stored under ambient conditions. In general can be said that the two crystallization conditions displayed differences in the theta/2theta patterns and these differences were observed over the selected time period. As discussed in Chapter 7.2, crystallization in the presence of a bulk surface reservoir (Figure 7.21A) showed weak long-spacing $\{00l\}$ reflections. Such lamellar reflections were observed in all collected WAXS pattern. Different relative intensities may be from changed illuminated areas of the samples. On the other hand, *n*-tetracosane crystallized in the absence of a bulk surface reservoir (Figure 7.21B) showed no long-spacing $\{00l\}$ layer peaks. After two month storage weak triclinic layer peaks were detected. Such peaks might be from residues of bulk *n*-tetracosane surface material. Complete removing of the material is challenging. However, both patterns are dominated by a strong reflection at $2\theta = 36.0^\circ$.

It can be supposed that long-time storage did not change the crystal texture which directly occurred after crystallization. Molecule rearrangement may occur, but on a very slow time scale. *n*-Tetracosane in AAO membranes is stable over a longer time period which may be of interest for further studies when measurements are more time consuming.

7.8 Discussion of *n*-Tetracosane in 2D-Confinement

The results revealed that *n*-tetracosane in nanoporous matrices showed a more complex crystallization behavior than the bulk material. The investigations highlighted that crystallization conditions such as the presence or the absence of bulk surface reservoirs, the pore sizes, the modification of AAO with ODPA, or the pore morphology play an important role for the crystallization pathways.

7.8.1 Crystallite Orientation of Triclinic *n*-Tetracosane in AAO Membranes

Texture analysis of *n*-tetracosane in AAO membranes crystallized at a rate of -0.5 K/min in the presence (Ch. 7.2) or in the absence (Ch. 7.4) of a *n*-tetracosane surface reservoir revealed uniaxial oriented crystals with their triclinic (-111) lattice planes⁷² oriented normal to the pore axis (Figure 7.22). Directly after non-isothermal crystallization such preferred orientation was observed. When the (-111) lattice planes are oriented normal to the AAO pore axis, the molecules long axes are also oriented normal to the AAO pore axis. In contrast, the (00 l) lattice planes are oriented parallel to the AAO pore axis. The theoretical angle between the (-111) $2\theta = 36.0^\circ$ and (002) ($2\theta = 5.8^\circ$) lattice planes is 69.5° . Furthermore, the (-111) reflection at $2\theta = 36.0^\circ$ was observed in all prepared samples independently of AAO pore sizes or modification of AAO with ODPA. Differences only occur depending on the temperature which will be discussed in the forthcoming section.

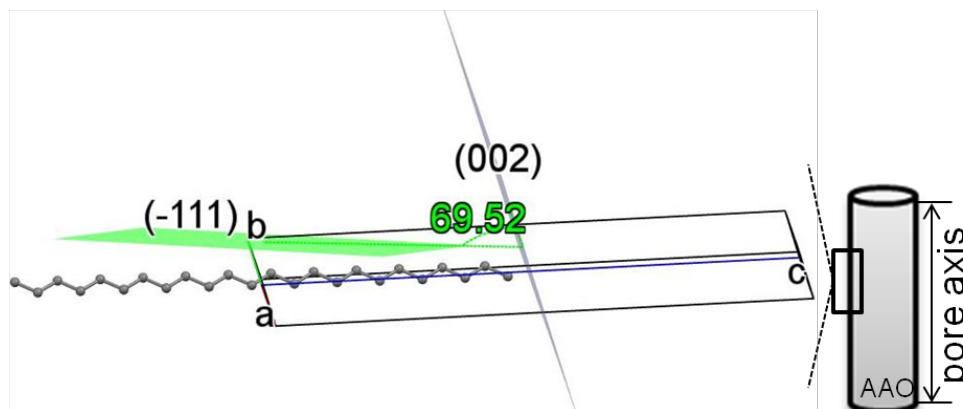


Figure 7.22: The triclinic unit cell of *n*-tetracosane in AAO membranes. The (-111) lattice planes are oriented normal to the pore axis, the (002) lattice planes are oriented parallel to the AAO pore axis. The unit cell is visualized with Mercury 3.1 based on CSD ZZZOF04⁷². Carbon atoms are grey and hydrogen atoms are not shown.

Crystal growth kinetics of *n*-tetracosane in AAO can be explained in the same way as for acetaminophen confined in AAO membranes (see Ch. 5.5.1). When the crystallizable material has contact to a bulk surface reservoir heterogeneous nucleation starts in the bulk surface film. Formed *n*-tetracosane crystals with their (-111) faces oriented normal to the AAO pores axis can grow fast along the nanopores. Other crystal orientations may impinge on the AAO pore walls; other crystal faces oriented normal to the AAO pore axis grow slowly and do not contribute much to crystal growth. In AAO membranes crystal orientations come into focus which have their fast-growing direction aligned with the AAO pore axis. In AAO membranes, the fast growth direction is the direction where the *n*-tetracosane molecules long axes are packed side-by-side and oriented normal to the AAO pore axis. The molecule interactions are stronger between molecules faced side-by-side than between molecules faced end-to-end. The preferred crystallite growth occurred independently from AAO pore size or pore wall modification. Estimated crystallite coherence lengths support this assumption. Along the direction parallel to the AAO pore axis, *n*-tetracosane in 60 nm AAO crystallized with bulk surface reservoir had a coherence length of ~44 nm, 25 nm AAO of ~40 nm, and AAO ODPA-modified of ~40 nm. The coherence lengths were quantified with the Scherrer equation (see Eq. 3.1).

n-Tetracosane in AAO non-isothermally crystallized without contact to a bulk surface reservoir also yielded crystals with the (-111) faces oriented normal to the AAO pore axis. Additionally, a second growth direction at $2\theta = 21.4^\circ$ (013) or (-111) occurred. These results may be explained with homogenous nucleation at higher supercooling. Many homogeneous nuclei can be formed in a narrow temperature range and hence, the growing of more crystals is initiated. The growing crystals compete for growth volume and have a change to occupy a volume portion in the AAO pores. As a consequence, the dominance of the crystallites with their triclinic (-111) lattice planes oriented normal to the AAO pore axis is hindered and a subpopulation of crystals with the triclinic (013) crystal face occur. A second explanation might be that, when crystallized without contact to a bulk surface film, a rotator phase is stabilized inside the AAO nanopores at 25 °C. Thus, the peak at $2\theta = 21.4^\circ$ belongs to the (-111) lattice planes corresponding to a mesophase. *n*-Tetracosane in 60 nm AAO membranes crystallized without bulk surface reservoir had along the direction normal to the (-111) lattice planes ($2\theta = 36.0^\circ$) a coherence length of ~40 nm, in 25 nm AAO membranes of ~34 nm, and in AAO ODPA-modified of ~44 nm. The estimated coherence length for the $21.4^\circ(013)/(-111)$ reflection amounted to the same value. The coherence length reveal that the crystal size is not influenced by the crystallization kinetics i.e., homogeneous or heterogeneous nucleated.

7.8.2 Influence of Pore Size, Bulk Surface Material, and Pore Wall Modification

A second aspect to consider is the effect of the pore size, the bulk surface material and the pore wall modification on crystallite orientation. It is important to understand the relationship between the resulting molecular structures and the crystallization conditions. The investigation will give answers how crystallization parameters affect resulting crystal textures. Interpretation of the temperature-dependent molecule orientation under confinement seems quite complex. However, the next two figures will illustrate the influence of the pore size, the bulk surface material and the AAO

modification with ODPA on the crystallization kinetics on the basis of characteristic lattice planes. As previously mentioned, *n*-tetracosane in AAO membranes cooled at -0.5 K/min in the presence of a bulk surface reservoir had a preferred triclinic crystallite orientation relative to the pore axis. The red dotted line in Figure 7.23 corresponds to the (-111) reflection at $2\theta = 36.0^\circ$ and is plotted as function of the temperature T . The solid black line corresponds to the peak at $2\theta = 23.3^\circ$ belonging to the (311) lattice planes⁷⁴ and is also plotted against the temperature.

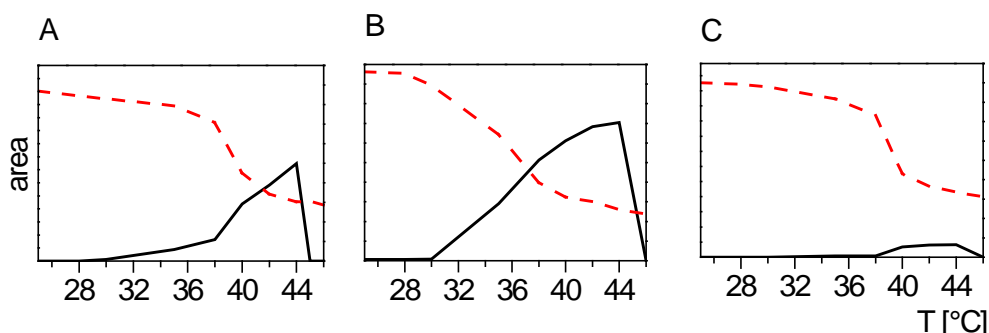


Figure 7.23: *n*-Tetracosane in AAO cooled at -0.5 K/min in the presence of a bulk surface reservoir. Measured areas of the peaks at $2\theta = 36.0^\circ$ (red dotted line) and $2\theta = 23.3^\circ$ (black solid line) as functions of the temperature T . A) AAO 60 nm, B) AAO 25 nm, C) AAO 60 nm ODPA-modified.

Obviously, the $2\theta = 36^\circ$ peak area decreased as the $2\theta = 23.3^\circ$ peak area increased. The 2θ reflection at 23.3° occurred at $\sim 35^\circ\text{C}$ and may belong to the rotator phases R_V or R_I . The occurrence of the 2θ peak at 23.3° is affected by the modification of AAO with ODPA. In modified samples, the 23.3° peak area was weak compared with the corresponding area of the 36.0° reflection in unmodified AAO membranes.

Figure 7.24 shows samples of *n*-tetracosane in AAO membranes cooled at -0.5 K/min in absence of a bulk surface reservoir (see Ch. 7.4). The dotted red line corresponds to the (-111) peak at $2\theta = 36.0^\circ$, the solid black line corresponds to the (013) peak at $2\theta = 21.4^\circ$, respectively. *n*-Tetracosane in 60 nm and 25 nm AAO membranes with unmodified pore walls were dominated by the 21.4° peak. Only the pattern of *n*-tetracosane in ODPA modified AAO was dominated by the reflection at 36.0° . Both

reflections showed a sharp decreasing at 40 °C. Estimated Hermans' order parameters for the 2 θ peak at 36.0° in Figure 7.25 underline these results.

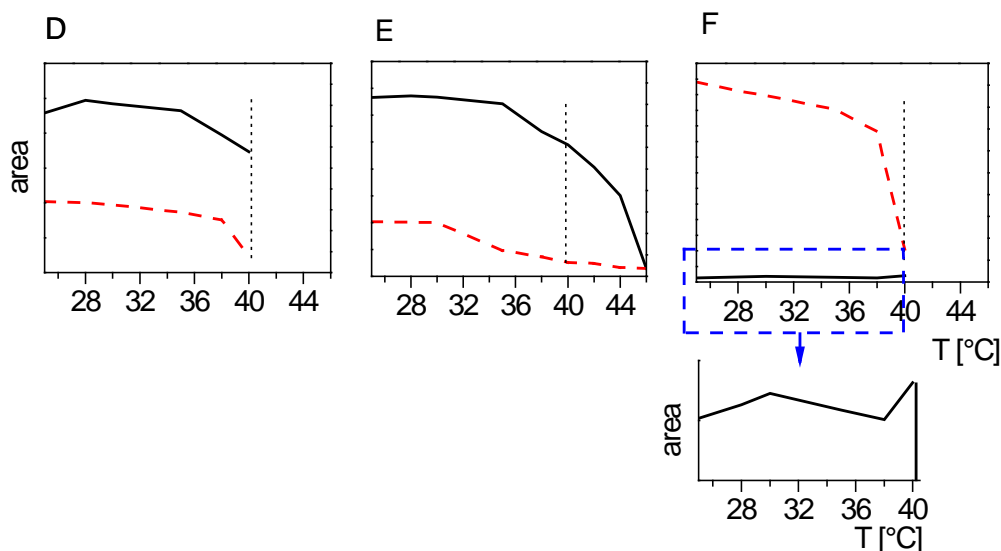


Figure 7.24: *n*-Tetracosane in AAO cooled at -0.5 K/min in the absence of a bulk surface reservoir. Measured areas of the peaks at $2\theta = 36.0^\circ$ (red dotted line) and $2\theta = 21.4^\circ$ (black solid line) as functions of the temperature T . A) AAO 60 nm, B) AAO 25 nm, C) AAO 60 nm ODPA-modified. The second row shows a zoomed figure.

Hermans' order parameters of *n*-tetracosane in 60 nm ODPA-modified AAO membranes (Figure 7.25a/b solid triangle) amounted to ~ 1 in both cases; crystallized with or without bulk surface reservoir. In contrast, the f values decreased from ~ 0.98 at 25°C to ~ 0.94 at 46°C for *n*-tetracosane in unmodified 60 nm AAO membranes crystallized with bulk surface reservoir (Figure 7.25a open rectangle). For samples crystallized without bulk surface reservoir Hermans' order parameters amounted to ~ 0.96 in the temperature range 25 – 40°C (Figure 7.25b open rectangle).

The order parameter decreased from $f = 0.98$ (25°C) to $f = 0.88$ at 46°C for *n*-tetracosane in 25 nm AAO membranes crystallized with bulk surface film (Figure 7.25a open circle). Crystallization without contact to a bulk surface reservoir (Figure 7.25b open circle) yielded f values of ~ 0.92 at 25°C and of ~ 0.76 at 40°C , respectively.

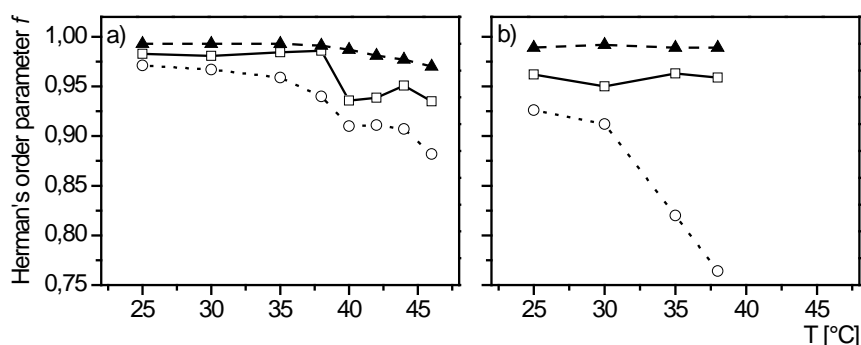


Figure 7.25: Calculated Hermans' order parameters f for the $2\theta = 36.0^\circ$ reflection of *n*-tetracosane in AAO cooled at -0.5 K/min; (a) in the presence of a bulk surface reservoir, (b) in the absence of a bulk surface reservoir. \square — AAO 60 nm, \circ — AAO 25 nm; \blacktriangle — AAO 60 nm ODPA-modified.

The results revealed that the modification of AAO with ODPA suppresses rotator phases. The access to bulk surface reservoir supported the dominance of the (-111) triclinic lattice planes ($2\theta = 36.0^\circ$) in unmodified AAO samples. The results can be explained as follows. ODPA forms a monolayer on flat crystalline alumina substrates with thicknesses from 18.1 \AA to 23.6 \AA ⁷⁷. In cylindrical AAO membranes the monolayer or self-assembly layers may not form. The results exposed that the grafted ODPA directs the *n*-tetracosane molecules in the position where the unit cell long axis is oriented normal to the AAO pore axis. Moreover, the ODPA alkyl chains may interact with the *n*-tetracosane long C–C alkyl chain. Nonpolar molecules mostly interact via van der Waals intermolecular forces⁶⁸. In other words, methylene-methylene interactions between ODPA and *n*-tetracosane and between *n*-tetracosane–*n*-tetracosane molecules exist. But the *n*-tetracosane molecule rotation seems more hindered around their long axis due to the grafting of ODPA molecules. As a result, phase transitions are hindered. Note phase transition involves a changing of the C–C plane around the unit cell long axis¹⁰ and a tilting or vice versa of the molecules.

n-Tetracosane in AAO crystallized with bulk surface reservoir resulted in uniaxial oriented crystals with their triclinic (-111) lattice planes oriented normal to the AAO pore axes. In contrast, *n*-tetracosane in unmodified AAO membranes cooled without

bulk surface reservoir showed a second crystal orientation or subpopulation of crystals with different orientations. As discussed above, the nucleation process changed from heterogeneous starting in bulk material to homogeneous when material nucleates in each AAO nanopore separately. Homogeneous nucleation results in formation of many growing crystals, then crystals with other orientations have also a chance to occupy a certain volume portion. Or, as a second explanation, homogeneous nucleation favors the stabilization of a rotator phase at lower temperatures.

7.8.3 Lamellar Crystals

(1) *Anodic Aluminum Oxide (AAO)*

Bulk *n*-tetracosane formed lamellar crystals which showed typical $\{00l\}$ long-spacing reflections in X-ray studies (Figure 7.2). *n*-Tetracosane confined in AAO membranes crystallized at a rate of -0.5 K/min in presence of a bulk surface reservoir also showed $\{00l\}$ layer reflections (Figure 7.11). Additionally, in AAO membranes triclinic and high temperature layer reflections occurred together. In all AAO membranes the d -values of the $\{00l\}$ layer reflections were higher in the R_{II} than in the triclinic phase. This is in line with the assumption that the phase transition $R_{II} \rightarrow$ triclinic involves a tilting of the molecules. In the R_{II} phase molecules are non-tilted and therefore, the layer thicknesses have higher values. *n*-Tetracosane molecules in 25 nm nanopores, due to the reduced pore size, are more tilted than in 60 nm AAO membranes or in bulk material. Furthermore, it could suggest that the crafted alkyl ODPA chains on the AAO pore walls influence the *n*-tetracosane molecule arrangement. In such samples d -values are higher than in samples with the same pore size but unmodified pore walls. There are two possibilities: (a) the molecules are more stretched or (b) the ODPA alkyl moieties are involved in the detectable *n*-tetracosane layer arrangement that influences the layer spacing.

Note during $\theta/2\theta$ scans the AAO surface is oriented normal to the scattered plane. In this geometry, only crystals that meet the Bragg condition and have the corresponding set of lattice planes normal to the AAO pore axis contribute to the detected scattering intensity. More details are given in the experimental section 3.1.

This might be one reason why layered $\{00l\}$ reflection are absent or have only weak intensities in the used $\theta/2\theta$ geometry. In the literature⁵⁰ layer reflections of *n*-alkanes confined to mesoporous silicon are only detected when the transition geometry is used. Further investigations with changed X-ray geometry may clarify the picture of the layer arrangement of *n*-tetracosane in AAO membranes.

Based on the actual $\theta/2\theta$ results, a two regime model is developed. Lamellar crystals are oriented normal to the AAO pore axis near the AAO pore walls (Figure 7.26a black bars). The molecules long axes are aligned with the AAO pore axis. But the vast majority of the molecules long axes are oriented normal to the AAO pore axis. On the other hand, lamellar crystals are also oriented normal to the AAO pore axis close the pore walls, but in the AAO ‘bulk’ no layered structures are built (Figure 7.26b).

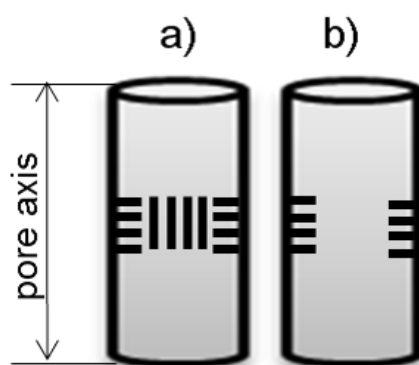


Figure 7.26: Schematic view of the two regime model of *n*-tetracosane in AAO crystallized in the presence of a bulk surface reservoir. (a) Lamellae (black bars) are oriented normal to the AAO pore axis close to AAO pore walls and are oriented parallel to the pore axis far from AAO pore walls. (b) Lamellae (black bars) are oriented normal to the AAO pore axis close to AAO pore walls and no layered structures in the AAO pores.

The next question is, whether the AAO pore sizes influences the lamellae formation. *n*-Tetracosane in 25 nm AAO crystallized with bulk surface reservoir showed strong $\{00l\}$ lamellar layer reflections at 44 °C (Figure 7.11). On the other hand, in the triclinic or in the R_V rotator phase, these reflections exhibited only weak intensities. An

interpretation of the results may be that in the triclinic phase the lamellar crystals are oriented parallel to the AAO pore axis far from AAO pore walls. Lamellar crystals only oriented normal to the AAO pore axis near the AAO pore walls. (Figure 7.26a) At 44 °C, lamellar crystals are also oriented normal to the AAO pore axis farther away from AAO pore walls. (Figure 7.27)

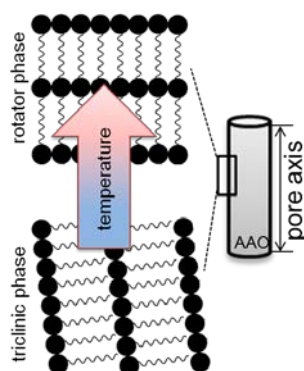


Figure 7.27: A schematic view of lamellar layers in 25 nm AAO where at 25 °C lamellar layers nearly oriented parallel to the AAO pore axis and at 44 °C lamellar layers oriented normal to the AAO pore axis.

One can suppose that in 25 nm AAO membranes the lamellar orientation is more influenced by the pore walls than in 60 nm nanopores. Molecules are more affected by the AAO pore wall surface. As a result, in 25 nm AAO more molecules have their long axis oriented aligned with the AAO pore axis resulting in $\{00l\}$ layer reflection at 44 °C. Nevertheless, it seems challenging to explain the lamellar arrangement sufficiently. Theta/2theta measurements could only detect lattice planes oriented parallel to the AAO membrane surface. Actually, first measurements with a changed X-ray geometry (in-plane geometry) revealed no reflections. Additionally, $I(\psi)$ profiles are only accessible up to $\sim 70^\circ$ (see Ch. 3.2.3). The theoretical angle between the (-111) and $(00l)$ lattice planes is around 70° so that the $I(\psi)$ maximum of the $(00l)$ reflections would occur outside the accessible range. However, further predictions require more detailed information about the lamellar crystals formed in the AAO nanopores.

n-Tetracosane in AAO crystallized without bulk surface reservoir displayed no $\{00l\}$ lamellar layer peaks in the used theta/2theta reflection geometry. Access to bulk surface

reservoir initiated homogeneous nucleation where the material nucleates in each pore separately which may lead to a disturbing of the layer arrangement near the AAO pore walls.

(2) *Controlled Porous Glasses (CPG)*

n-Tetracosane in CPG membranes with pore sizes larger than 2 nm cooled in the presence of a bulk surface film also showed lamellar crystals. In contrast, when crystallized without bulk surface reservoir such lamellar arrangement is missing. This observation underlines that the access to additional bulk material influences the possibility of lamellar formation near the pore walls.

7.8.4 Rotator Phases of *n*-Tetracosane in AAO Membranes

n-Tetracosane in AAO membranes showed, between the triclinic and the liquid phase, a series of rotator phases. WAXS and DSC studies revealed a relationship between phase transition temperatures and crystallization conditions such as the pore size, the contact to bulk surface material, or the modification of AAO with ODPA.

Table 7.1: Phase transition temperatures of *n*-tetracosane in AAO membranes measured with first DSC heating scans.

Sample name	AAO membrane [nm]	Transition temperatures on heating [°C]			
		R _V	R _I	R _{II}	melt
A	60	41.0	47.7	48.7	49
B	25			47.6	48.7
C	60 ODPA-mod	41.2		47.8	49.9
D	60	41.5		47.9	49.1
E	25				47.6
F	60 ODPA-mod	41.0		47.7	>48
	literature ^{69c}	43	44	47	51

^c The Material is mixed with hexane and dropped on a silicon wafer. The solvent is evaporated, and then the sample is mounted in an X-ray oven.

Table 7.1 lists the detected rotator phase sequences in all investigated AAO membranes. For example, *n*-tetracosane in 60 nm AAO crystallized with a bulk surface reservoir (case A) displayed the rotator phase sequence: triclinic– R_V – R_I – R_{II} –liquid. But, as can be seen in Table 7.1, not each sample showed all phase transitions.

Figure 7.28 summarizes the phase transitions for *n*-tetracosane in 60 nm AAO (case A). WAXS and DSC measurements detected the above mentioned phase sequence but differ in their phase transition temperatures. The temperature differences were not observed for bulk material. In DSC pans only small pieces of AAO membranes were used which should have a good thermal contact to the DSC pans. Additionally, the XRD heating device is not precise as the DSC device.

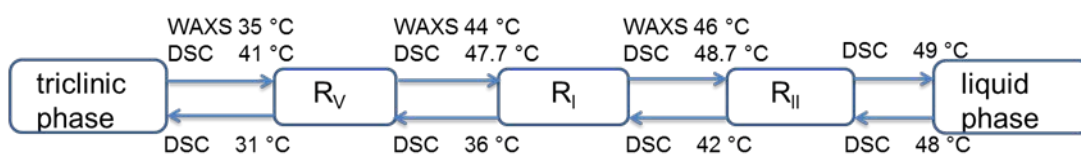


Figure 7.28: Summary of phase transitions of *n*-tetracosane in 60 nm AAO crystallized in the presence of a bulk surface reservoir. Note the X-ray measurements ends up to 46°C.

However, according to the WAXS and DSC results, the temperature range of the R_V phase is enlarged or the R_I phase region is reduced. For example, *n*-tetracosane in 60 nm AAO membranes crystallized with bulk surface reservoir showed the interphase transition triclinic→ R_V at 41.0 °C and the interphase transition R_V → R_I at ~48 °C, respectively. A thin film of *n*-tetracosane on a silicon wafer⁶⁹ displays phase transitions at 43 °C (triclinic→ R_V) and at 44 °C (R_V → R_I), respectively. One can suppose that in rotator phases there are numbers of gauche-bond defects near the chain ends⁶⁸ this will be reduce the lengthwise overlap of the adjacent segments⁵¹ and a tilting of the molecules may favor. In the R_V rotator phase molecules are tilted as compared to the R_I phase with non-tilted molecules. Consequently, a tilted molecule arrangement may be preferentially chosen under confinement.

WAXS studies in Chapter 7.2 and DSC heating scans in Chapter 7.6 support the notion that some phase transitions do not occur; (i) when material crystallized in each pore separately, (ii) in 25 nm AAO, and (iii) in ODPA modified AAO membranes. Reasons for suppressed phase transitions can be complex. For example, *n*-tetracosane confined in 25 nm AAO membranes crystallized with bulk surface reservoir showed only the phase transition triclinic \rightarrow R_{II} at $\sim 47^\circ$ (Table 7.1). On the other hand, $\theta/2\theta$ measurements exhibited interphase transitions at 35 °C (triclinic \rightarrow R_V) and at $\sim 46^\circ$ C (R_V \rightarrow R_{II}), respectively (Figure 7.6). As previously mentioned, the transition R_V \leftrightarrow R_I involves only a change in the molecule tilt angle. The transition R_I \leftrightarrow R_{II} includes a change in the layer stacking sequence AB \leftrightarrow ABC accompanied by a lattice distortion. The phase transition enthalpy of R_I \leftrightarrow R_{II} should be higher than for the R_V \leftrightarrow R_I transition. Some phase transitions show only a small enthalpy change and may not be detected during a DSC scan.

7.8.5 Summary

Crystallite orientation, rotator phases and lamellar crystals formation of *n*-tetracosane confined in cylindrical, isolated AAO and in curved, interconnected CPG membranes can be summarized as follows. (1) In AAO membranes uniformly oriented crystals grow with their (-111) lattice planes oriented normal to the AAO pore axes. Such preferred growth occurs independently from the AAO pore size, the modification of AAO with ODPA, or the access to bulk surface reservoir. (2) The preferred crystal growth was not detected in CPG membranes. In CPG membranes the free crystal growth path is limited due to the curved morphology. Isotropic pore morphologies do not show crystal texture. (3) Bulk *n*-tetracosane forms lamellar crystals. Under confinement such lamellar structures were also observed, especially in cases of crystallization in contact to a bulk surface reservoir. Actually, a two regime model of the lamellar crystal arrangement in AAO membranes is suggested. The lamellar layers are oriented normal to the pore axis near the AAO pore walls and (a) oriented parallel to the pore axis far from AAO pore walls, or (b) no layered structures occurred in the AAO pores. But a changed X-ray geometry (e.g., in-plane) may help to explain the

lamellar arrangement in AAO membranes in more details. (4) *n*-Tetracosane in CPG membranes also exhibited lamellar structures especially in the rotator phases. (5) The crystalline phase was suppressed in smaller CPG membranes ($d \sim 2$ nm). One assumption might be that on CPG walls a rigid amorphous layer is built and the thickness of the layer lies in the pore size range. (6) In 60 nm AAO membranes the temperature range, where the R_V rotator phase occur, could be enlarged. Under confinement, a tilting of the molecules is favored and rotator phase R_V will be more stabilized. (7) *n*-Tetracosane in 60 nm AAO membranes crystallized with bulk surface reservoir revealed the rotator phase sequence: triclinic- R_V - R_I - R_{II} -liquid. (8) In AAO pore sizes smaller than 60 nm the observation of the phase transition is challenging. One reason might be the influence of AAO pore walls due to the surface-to-volume ratio increasing in smaller pore sizes. (9) Crafted ODPAs on AAO pore walls might interact via the alkyl moieties with the alkyl moieties of *n*-tetracosane. Hence, on the AAO pore wall an interphase of the octadecyl moieties of ODPAs and the alkyl moieties of *n*-tetracosane exist. The octadecyl moieties support the molecule arrangement where the long axis is oriented normal to the pore axis. Such interaction hinders the occurrence of rotator phases. (10) Confined *n*-tetracosane shows stable crystallite orientation for a longer time interval. The nanosized material can be used for more time consuming investigations. Sample storage under ambient conditions is possible.

8 Conclusions and Outlook

Acetaminophen, a low-molecular weight polymorphic drug, and *n*-tetracosane, a saturated hydrocarbon, have been chosen as model guest compounds embedded in two nanoporous matrices: AAO containing aligned cylindrical, isolated pores and CPG containing curved, interconnected pores. Additional studies reveal that both model guests are sensitive to changes in their crystallization conditions. The influence of the crystallization parameters (i.e., the pore morphology, the thermal history, the pore sizes, the pore wall chemistry, the presence or the absence of a bulk surface reservoir) of the crystallizing species on crystallization kinetics was systematically screened. For example, in the case of acetaminophen it could be shown that the pore morphology is an important parameter controlling polymorph formation as well as crystallite orientation, and the kinetics of solid/solid transitions under confinement. Non-isothermal crystallization of acetaminophen in AAO with a pore diameter of 60 nm at -0.5 K/min in the presence of a bulk surface reservoir yields highly oriented form II/form III crystals. Under identical conditions, acetaminophen form I crystals preferentially grow in CPG. Acetaminophen form II and form III crystals have a close structure registry along the crystal directions aligned with the AAO pore axes. Thus, in AAO membranes uniformly oriented form III crystals undergo a solid/solid transition to uniformly oriented form II crystals during which the transition front propagates through the straight AAO pores. In CPG membranes, the propagation front will impinge on the pore walls after a short propagation path. One can conclude that under identical crystallization conditions the pore morphology initiates a kinetic selection process.

Apart from crystalline forms for pharmaceutical application, the amorphous form of a drug is of interest. Amorphous forms often exhibit higher dissolution rates and hence better bioavailability regarding to the thermodynamic more stable crystalline forms. Therefore, amorphous forms and their life time are pharmaceutically relevant aspects. Amorphous acetaminophen in AAO membranes can easily be obtained by rapid quenching of the melt without bulk acetaminophen surface reservoir. Moreover, crystallization can be suppressed in AAO membranes with 25 nm pores. It can be

assumed that nucleation of acetaminophen in isolated AAO pores is predominantly homogeneous which could be one reason for the retarded crystallization kinetics. Nanosized amorphous acetaminophen is stable for several months.

The study on crystallization parameters such as the thermal history, and the presence or the absence of bulk surface reservoir shows that they can be used as a tool for high-yield productions of specific polymorphs of polymorphic drugs in AAO membranes. Crystallization parameters can be optimized to obtain the desired drug polymorph or crystallite orientation. The capability to produce drugs consisting of specific polymorphs with specific crystal orientation does not only enable polymorph-specific drug release but also crystal-face specific drug release from nanosized drug carriers. Drug release rates can be linked to specific crystal faces. Rough crystal faces have out-facing functional moieties which can interact with solvent molecules. Dissolution tests of acetaminophen in AAO membranes reveal that form I and form II crystals having rough crystal faces exposed to the environment are dissolved nearly as fast as amorphous acetaminophen in a burst mechanism within the first few minutes. However, complete dissolution was only observed for crystalline acetaminophen, whereas in the case of amorphous acetaminophen a small portion of the material did not dissolve. This outcome indicates that amorphous acetaminophen forms stable interfacial layers on the AAO pore walls during the aging of the sample. Fitted release data suggest that the dissolution of acetaminophen from AAO membranes is not diffusion-controlled within the first minutes. It can be assumed that the dissolution is surface-limited. Retardation of the release of acetaminophen from AAO was accomplished by encapsulation of acetaminophen in AAO with a biodegradable polymer. The dissolution tests show a delay in the drug release. The encapsulation process retards the drug release but does not modify the release kinetics.

In this thesis, controlled polymorph formation in geometrically defined nanoconfinement and the use of AAO membranes as drug delivery carriers was combined. This concept might be extended to the use of other matrices, for example titanium oxide nanotube arrays¹¹⁶, or block copolymer membranes²⁰ as drug delivery systems. Titania nanotube arrays have, for example, been used as orthopedic or dental

implants¹⁸ due to their high biocompatibility. First drug release kinetics based on titania nanotube arrays show promising results.¹¹²

Crystallization of *n*-tetracosane has also been studied, because this member of the *n*-alkane family is representative of compounds forming lamella crystals. Besides triclinic lamella crystals, bulk *n*-tetracosane forms one rotator phase between the solid triclinic and the isotropic liquid phase. Non-isothermal crystallization of *n*-tetracosane in unmodified 60 nm AAO pores in the presence of a bulk *n*-tetracosane surface reservoir yields the rotator phase sequence: triclinic–R_V–R_I–R_{II}–liquid. The occurrence of rotator phases is linked to crystallization parameters such as the pore size, the presence of bulk surface reservoirs of *n*-tetracosane, and the modification of the AAO pore walls with coupling agents such as ODPA. Furthermore, *n*-tetracosane in AAO non-isothermally crystallized with or without bulk surface reservoirs of *n*-tetracosane revealed uniaxial oriented crystals. It can be assumed that only crystals with their directions of fast growth aligned to the AAO pore axis will fill the volume of the nanopores. Other crystals with different orientations might impinge on the AAO pore walls and will not be able to grow further. The preferred crystal growth occurs independently from AAO pore size or modification of AAO with ODPA. On the other hand, modification of AAO with ODPA suppresses the occurrence of rotator phases. The octadecyl moieties of ODPA and the alkyl moieties of *n*-tetracosane build an interphase near the AAO pore wall. The crafted ODPA molecules favor a strong alignment of *n*-tetracosane where the long axes of the *n*-tetracosane molecules are oriented normal to the AAO pore axis.

Interpretation of the lamellar order in AAO membranes is difficult; therefore, a two regime model is described here. *n*-Tetracosane in AAO crystallized with a bulk surface reservoir forms lamellar crystals which are oriented normal to the AAO pore axis near the pore walls. On the other hand, away from the pore walls (a) the lamellae are oriented parallel to the AAO pore axis or (b) no layered structures are built.

In CPG membranes, lamellar order is also detected. No crystalline structures occur in smaller CPG pores (mean pore diameter ~2 nm) and hence, no layered arrangement is observed in wide-angle X-ray scattering experiments. In such small pores, with large surface-to-volume ratio, the AAO pore walls prevent ordering of a large portion of *n*-tetracosane molecules so that crystallization is inhibited. In general, *n*-tetracosane shows

a more complex phase behavior than the high-molecular weight analogue polyethylene¹³. But the variation of the crystallization parameters such as the pore size and the contact with an *n*-tetracosane bulk surface reservoir offers opportunities to investigate phase transitions depending on the temperature. Interpretations are often complicated.

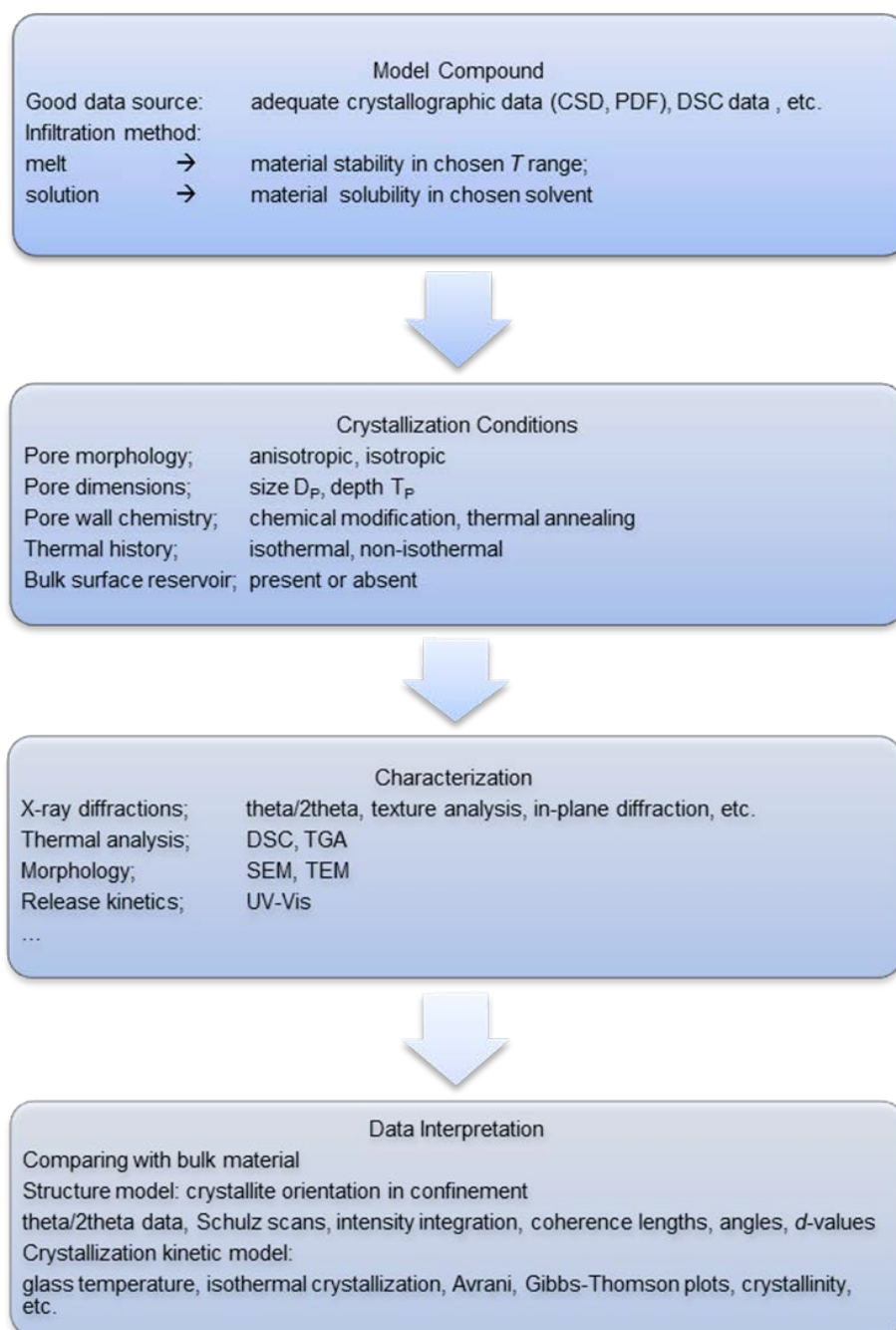


Figure 8.1: Schematic view of mesoscopic crystal engineering.

The use of anisotropic AAO and isotropic CPG membranes as hosts for crystallizable guests opens new pathways to manipulate crystal growth with control over polymorph formation, phase transitions and crystallite orientation. This work highlights the influence of crystallization parameters such as the pore morphology, the thermal history, the pore sizes, the pore wall chemistry, and the presence or the absence of bulk surface reservoir on crystal growth in nanoscale environments. The present study offers strategies to modify the crystallization pathways and extends the parameter space by parameters such as the pore morphology and the presence or the absence of a bulk reservoir of the crystallizing species in contact with the crystallizing nanostructures for mesoscopic crystal engineering (Figure 8.1). The methods might be transferred into other areas of interest such as polymorphism screening, and the preparation of nanostructures where the functional properties depend on the way the materials crystallize. Examples are nanowires with ferroelectric or specific optoelectronic properties.

The use of anodic aluminum oxide membranes as nanoporous matrices is one aspect; the characterization of AAO membranes is another. For example, electron paramagnetic resonance spectroscopy shows a relationship between the AAO preparation (i.e., electrolyte solution) and formation of organic radicals. AAO pore walls are grafted with alkyl chains by modifying them with ODPa which result in hydrophobic low energy surfaces. A deeper understanding of how such coupling agents arrange on curved pore walls is a quite interesting topic.¹¹⁷ Another question is, whether the polarity ($-\text{OH} > -\text{NH}_2 > -\text{CH}_3$) of the functional group has an influence on the AAO surface energy. New functional groups will change the AAO surface chemistry (i.e., hydrophilic–hydrophobic properties) which might influence the crystallization kinetics. Nevertheless, the density of hydroxyl groups on AAO pore walls is a good example of an important parameter for the binding rate of coupling agents. Determination of the hydroxyl groups should be investigated with proper surface characterization techniques.^{76, 77, 79}

9 Bibliography

1. Alcoutlabi, M.; McKenna, G. B. *J. Phys. Condens. Matter* **2005**, *17*, R461-R524.
2. Hamilton, B. D.; Ha, J.-M.; Hillmyer, M. A.; Ward, M. D. *Acc. Chem. Res.* **2012**, *45*, 414-423.
3. Lu, J.; Rohani, S. *Curr. Med. Chem.* **2009**, *16*, 884-905.
4. Jiang, Q.; Ward, M. D. *Chem. Soc. Rev.* **2014**, *43*, 2066-2079.
5. Masuda, H.; Fukuda, K. *Science* **1995**, *268*, 1466-1468.
6. Enke, D.; Janowski, F.; Schwieger, W. *Micropor. Mesopor. Mater.* **2003**, *60*, 19-30.
7. Rengarajan, G. T.; Enke, D.; Steinhart, M.; Beiner, M. *Phys. Chem. Chem. Phys.* **2011**, *13*, 21367-21374.
8. Hamilton, B. D.; Hillmyer, M. A.; Ward, M. D. *Cryst. Growth Des.* **2008**, *8*, 3368-3375.
9. Beiner, M.; Rengarajan, G. T.; Pankaj, S.; Enke, D.; Steinhart, M. *Nano Lett.* **2007**, *7*, 1381-1385.
10. Huber, P.; Wallacher, D.; Albers, J.; Knorr, K. *Europhys. Lett.* **2004**, *65*, 351-357.
11. Steinhart, M.; Göring, P.; Dernaika, H.; Prabhakaran, M.; Gösele, U.; Hempel, E.; Thurn-Albrecht, T. *Phys. Rev. Lett.* **2006**, *97*, 027801.
12. Steinhart, M.; Senz, S.; Wehrspohn, R. B.; Gösele, U.; Wendorff, J. H. *Macromolecules* **2003**, *36*, 3646-3651.
13. Shin, K.; Woo, E.; Jeong, Y. G.; Kim, C.; Huh, J.; Kwang-Woo, K. *Macromolecules* **2007**, *40*, 6617-6623.

14. Hamilton, B. D.; Weissbuch, I.; Lahav, M.; Hillmyer, M. A.; Ward, M. D. *J. Am. Chem. Soc.* **2009**, *131*, 2588-2596.
15. Shingne, N.; Geuss, M.; Hartmann-Azanza, B.; Steinhart, M.; Thurn-Albrecht, T. *Polymer* **2013**, *54*, 2737-2744.
16. Duran, H.; Hartmann-Azanza, B.; Steinhart, M.; Gehring, D.; Laquai, F.; Feng, X.; Müllen, K.; Butt, H.-J.; Floudas, G. *ACS Nano* **2012**, *6*, 9359-9365.
17. Grigoriadis, C.; Duran, H.; Steinhart, M.; Kappl, M.; Butt, H.-J.; Floudas, G. *ACS Nano* **2011**, *11*, 9208-9215.
18. Losic, D.; Simovic, S. *Expert Opin. Drug Deliv.* **2009**, *6*, 1363-1381.
19. Perry, J. L.; Martin, C. R.; Stewart, J. D. *Chem. Eur. J.* **2011**, *17*, 6296-6302.
20. Jeon, G.; Yun Yang, S.; Kon Kim, J. *J. Mater. Chem.* **2012**, *22*, 14814-14834.
21. Rengarajan, G. T.; Enke, D.; Beiner, M. *Open J. Phys. Chem.* **2007**, *1*, 18-24.
22. Rengarajan, G. T.; Enke, D.; Steinhart, M.; Beiner, M. *J. Mater. Chem.* **2008**, *15*, 2537-2539.
23. Desiraju, G. R. *J. Am. Chem. Soc.* **2013**, *135*, 9952-9967.
24. Cui, Y. *Int. J. Pharm.* **2007**, *339*, 3-18.
25. Hilfiker, editor, *Polymorphism*. Wiley-VCH Verlag GmbH Co. KGaA: **2006**.
26. Pethrick, R. A. *Polymer Structure Characterization from Nano to Macro Organization*; RSC Publishing, Cambridge, **2007**.
27. Mullin, J. W. *Crystallization*; Butterworth-Heinemann: **2001**.
28. *The Collected Works of Gibbs, J. W.* Longmas, Green and Co., New York, London, Totonto, **1928**.

29. Turnbull, D. J. *J. Chem. Phys.* **1950**, *18*, 198-203.
30. He, B. B. *Two-Dimensional X-Ray Diffraction*; John Wiley & Sons, Inc.: Hoboken, New Jersey, **2009**.
31. Spieß, L.; Teichert, G.; Schwarzer, R.; Behnken, H.; Genzel, C. *Moderne Röntgenbeugung*; Vieweg+Teubner, GWV Fachverlage GmbH: Wiesbaden, **2009**.
32. Massa, W. *Kristallstrukturbestimmung*; B. G. Teubner Verlag: Wiesbaden, **2007**.
33. Atkins, P.; de Paula, J. *Physical Chemistry*; W. H. Freeman and Company: New York, **2006**.
34. Ward, M. D. *Chem. Rev.* **2001**, *101*, 1697-1725.
35. Jackson, K. A. Chapter 21 The Surface-Roughening Transition. In *Kinetic Processes*; Wiley-VCH Verlag GmbH & Co. KGaA: **2004**; pp 283-310.
36. Lovette, M. A.; Robben Browning, A.; Griffin, D. W.; Sizemore, J. P.; Snyder, R. C.; Doherty, M. F. *Ind. Eng. Chem. Res.* **2008**, *47*, 9812-9833.
37. Hartman, P.; Perdok, W. G. *Acta Cryst.* **1955**, *8*, 49-52.
38. Grimbergen, R. F. P.; Meekes, H.; Bennema, P.; Strom, C. S.; Vogels, L. J. P. *Acta Cryst.* **1998**, *A54*, 491-500.
39. Hartman, P.; Bennema, P. *J. Cryst. Growth* **1980**, *49*, 145-156.
40. Bennema, P.; Meekes, H.; Boerrigter, S. X. M.; Cuppen, H. M.; Deij, M. A.; van Eupen, J.; Verwer, P.; Vlieg, E. *Cryst. Growth Des.* **2004**, *4*, 905-913.
41. Florence, A. T.; Attwood, D. *Physicochemical Principles of Pharmacy*; Pharmaceutical Press: **2006**.
42. Bernstein, J.; Davey, R. J.; Henck, J.-O. *Angew. Chem. Int. Ed.* **1999**, *38*, 3440-3461.

43. Datta, S.; Grant, D. J. W. *Nat. Rev. Drug Discov.* **2004**, *3*, 42-57.
44. Burger, A.; Ramberger, R. *Mikrochim. Acta* **1979**, *2*, 259-271.
45. Ha, J.-M.; Wolf, J. H.; Hillmyer, M. A.; Ward, M. D. *J. Am. Chem. Soc.* **2004**, *126*, 3382-3383.
46. Ha, J.-M.; Hillmyer, M. A.; Ward, M. D. *J. Phys. Chem. B* **2005**, *109*, 1392-1399.
47. Ha, J.-M.; Hamilton, B. D.; Hillmyer, M. A.; Ward, M. D. *Cryst. Growth Des.* **2009**, *9*, 4766-4777.
48. Henschel, A.; Huber, P.; Knorr, K. *Phys. Rev. E* **2008**, *77*, 042602.
49. Duran, H.; Steinhart, M.; Butt, H.-J.; Floudas, G. *Nano Lett.* **2011**, *11*, 1671-1675.
50. Henschel, A.; Hofmann, T.; Huber, P.; Knorr, K. *Phys. Rev. E* **2007**, *75*, 021607.
51. Kumar, M. V.; Prasad, S. K.; Rao, D. S. S. *Langmuir* **2010**, *26*, 18362-18368.
52. Kim, B. S.; Jeong, Y. G.; Shin, K. *J. Phys. Chem. B* **2013**, *117*, 5978-5988.
53. Yan, X.; Wang, T. B.; Gao, C. F.; Lan, X. Z. *J. Phys. Chem. C* **2013**, *117*, 17245-17255.
54. Su, Y.; Liu, G.; Xie, B.; Fu, D.; Wang, D. *Acc. Chem. Res.* **2014**, *47*, 192-201.
55. Masuda, H.; Yada, K.; Osaka, A. *Jpn. J. Appl. Phys.* **1998**, *37*, L 1340-L 1342.
56. Li, A. P.; Müller, F.; Birner, A.; Nielsch, K.; Gösele, U. *J. Appl. Phys.* **1998**, *84*, 6023-6026.
57. Schwirn, K.; Lee, W.; Hillebrand, R.; Steinhart, M.; Nielsch, K.; Gösele, U. *ACS Nano* **2008**, *2*, 302-310.
58. Steinhart, M. *Adv. Polym. Sci.* **2008**, *220*, 123-187.

59. Lee, W.; Ji, R.; Gösele, U.; Nielsch, K. *Nature Materials* **2006**, *5*, 741-747.
60. <http://www.drugbank.ca/> (accessed Juni/18, 2012).
61. Welton, J. M.; McCarthy, G. J. *Powder Diffr.* **1988**, *3*, 102-103.
62. Naumov, D. Y.; Vasilchenko, M. A.; Howard, J. A. K. *Acta Crystallogr., Sect. C.: Cryst. Struct. Commun.* **1998**, *54*, 653.
63. Drebuschak, T. N.; Boldyreva, E. V. *Z. Kristallogr.* **2004**, *219*, 506-512.
64. Di Martino, P.; Conflant, P.; Drache, M.; Huvenne, J.-P.; Guyot-Hermann, A.-M. *J. Therm. Anal. Calorim.* **1997**, *48*, 447-458.
65. Perrin, M.-A.; Neumann, M. A.; Elmaleh, H.; Zaske, L. *Chem. Commun.* **2009**, 3181-3183.
66. Peterson, M. L.; Morissette, S. L.; McNulty, C.; Goldsweig, A.; Shaw, P.; LeQuesne, M.; Monagle, J.; Encina, N.; Marchionna, J.; Johnson, A.; Gonzalez-Zugasti, J.; Lemmo, A. V.; Ellis, S. J.; Cima, M. J.; Almarsson, O. J. *J. Am. Chem. Soc.* **2002**, *124*, 10958-10959.
67. Nichols, G.; Frampton, C. S. *J. Pharm. Sci.* **1998**, *87*, 684-693.
68. Ocko, B. M.; Wu, X. Z.; Sirota, E. B.; Sinha, S. K.; Gang, O.; Deutsch, M. *Phys. Rev. E* **1997**, *55*, 3164-3182.
69. Sirota, E. B.; King, J., H. E.; Singer, D. M.; Shao, H. H. *J. Chem. Phys.* **1993**, *98*, 5809-5824.
70. Zammit, U.; Marinelli, F.; Mercuri, F.; Paoloni, S. *J. Phys. Chem. B* **2010**, *114*, 8134-8139.
71. Craievich, A. F.; Doucet, J.; Denicolo, I. *Phys. Rev. B* **1985**, *32*, 4164-4168.
72. Gerson, A. R.; Nyburg, S. C. *Acta Cryst.* **1992**, *B48*, 737-741.

73. Fletcher, D. A.; McMeeking, R. F.; Parkin, D. J. *Chem. Inf. Comput. Sci.* **1996**, *36*, 746-749.
74. Mazee, W. M. *Rec. Tra. Chim.* **1948**, *67*, 197-213.
75. Fontes, G. N.; Malachias, A.; Magalhaes-Paniago, R.; Neves, B. R. A. *Langmuir* **2003**, *19*, 3345-3349.
76. Lushtinetz, R.; Seifert, G.; Jaehne, E.; Adler, H.-J. P. *Macromol. Symp.* **2007**, *254*, 248-253.
77. Lushtinetz, R.; Oliveira, A. F.; Duarte, H. A.; Seifert, G. *Z. Anorg. Allg. Chem.* **2010**, *636*, 1506-1512.
78. Love, J. C.; Estroff, L. A.; Kriebel, J. K.; Nuzzo, R. G.; Whitesides, G. M. *Chem. Rev.* **2005**, *105*, 1103-1169.
79. Thissen, P.; Valtiner, M.; Grundmeier, G. *Langmuir* **2010**, *26*, 156-164.
80. Hoque, E.; DeRose, J. A.; Kulik, G.; Hoffmann, P.; Mathieu, H. J.; Bhushan, B. *J. Phys. Chem. B* **2006**, *110*, 10855-10861.
81. Hoque, E.; DeRose, J. A.; Hoffmann, P.; Mathieu, H. J.; Bhushan, B.; Cichomski, M. *J. Chem. Phys.* **2006**, *124*, 174710-1-174710-6.
82. Schreiber, F. *Prog. Surf. Sci.* **2000**, *65*, 151-256.
83. Liakos, I. L.; McAlpine, E.; Chen, X.; Newman, R.; Alexander, R. M. *Appl. Surf. Sci.* **2008**, *255*, 3276-3282.
84. Textor, M.; Ruiz, L.; Hofer, R.; Rossi, A.; Feldman, K.; Hähner, G.; Spencer, N. D. *Langmuir* **2000**, *16*, 3257-3271.
85. Cui, S. T.; Gupta, S. A.; Cummings, P. T.; Cochran, H. D. *J. Chem. Phys.* **1996**, *105*, 1214-1220.

86. Pecharsky, V. K.; Zavalij, P. Y. Origin of the powder diffraction pattern. In *Fundamentals of Powder Diffraction and Structural Characterization of Materials*; Springer Science+Business Media, Inc.: **2003**; pp 153-158.
87. Graubner, G.; Rengarajan, G. T.; Anders, N.; Sonnenberger, N.; Enke, D.; Beiner, M.; Steinhart, M. *Cryst. Growth Des.* **2014**, *14*, 78-86.
88. Schulz, L. G. *J. Appl. Phys.* **1949**, *20*, 1030-1033.
89. Shingne, N. Morphology and Crystal Orientation of Ferroelectric P(VDF-ran-TrFE) Nanostructures in Porous Aluminium Oxide, Martin-Luther-Universität Halle-Wittenberg, Dissertation, **2010**.
90. Chernock, W. P.; Beck, P. A. *J. Appl. Phys.* **1952**, *23*, 341-345.
91. Hermans, P. H.; Weidinger, A.; Vermaas, D. *Rec. Trav. Chim.* **1946**, *65*, 427-447.
92. Patterson, A. L. *Phys. Rev.* **1939**, *56*, 978-982.
93. Höhne, G. W. H.; Hemminger, W. F.; Flammersheim, H.-J. *Differential Scanning Calorimetry*; Springer-Verlag: Berlin, Heidelberg, New York, **2003**.
94. Cammenga, H. K.; Epple, M. *Angew. Chem.* **1995**, *107*, 1284-1301.
95. Differential Scanning Calorimetry (DSC) A Beginner's Guide. http://www.perkinelmer.de/CMSResources/Images/4474542GDE_DSCBeginnersGuide.pdf (2014).
96. Strobel, G. *The Physics of Polymers*; Springer-Verlag: Berlin-Heidelberg, **2007**.
97. Roland, U.; Holzer, F.; Pöppel, A.; Kopinke, F.-D. *Appl. Catal. B-Environ.* **2005**, *58*, 227-234.
98. Burley, J. C.; Duer, M. J.; Stein, R. S.; Vrcelj, R. M. *Eur. J. Pharm. Sci.* **2007**, *31*, 271-276.

99. Rengarajan, G. T. Polymorphism of Acetaminophen under Nanoconfinement, Martin-Luther-Universität Halle-Wittenberg, Dissertation, **2009**.
100. Bridgman, P. W. *Proc. Am. Acad. Arts Sci.* **1925**, 60, 305-385.
101. Beyer, T.; Day, G. M.; Price, S. L. *J. Am. Chem. Soc.* **2001**, 123, 5086-5094.
102. Siepmann, J.; Peppas, N. A. *Int. J. Pharm.* **2011**, 418, 6-12.
103. Gottwald, W. *Statistik für Anwender*; WILEY-VCH GmbH: Weinheim, **2004**.
104. Korsmeyer, R. W.; Gurny, R.; Doelker, E.; Buri, P.; Peppas, N. A. *Int. J. Pharm.* **1983**, 15, 25-35.
105. Ritger, P. L.; Peppas, N. A. *J. Control Release* **1987**, 5, 23-36.
106. Einführung in Origin 8.1.

<http://www.additive-net.de/ftp/win32/software/origin/EinfuehrunginOrigin8.pdf>
(accessed 09.10.2013).
107. Gavin, H. P. The Levenberg-Marquardt method for nonlinear least squares curve-fitting problems. *<http://people.duke.edu/~hpgavin/ce281/lm.pdf>* (2014).
108. Simovic, S.; Losic, D.; Vasilev, K. *Chem. Commun.* **2010**, 46, 1317-1319.
109. Grayson, A. C. R.; Choi, I. S.; Tyler, B. M.; Wang, P. P.; Brem, H.; Cima, M. J.; Langer, R. *Nat. Mater.* **2003**, 2, 767-772.
110. Weir, N. A.; Buchanan, F. J.; Orr, J. F.; Dickson, G. R. *Proc. Instn. Mech. Engrs. Part H: J. Engineering in Medicine* **2004**, 218, 307-319.
111. Brizzolara, D.; Cantow, H.-J. J.; Diederichs, K.; Keller, E.; Domb, A. J. *Macromolecules* **1996**, 29, 191-197.
112. Aw, M. S.; Addai-Mensah, J.; Losic, D. *Chem. Commun.* **2012**, 48, 3348-3350.

113. Israelachvili, J. N. *Intermolecular and Surface Forces*; Elsevier Inc.: **2011**.
114. Gao, Y.; Olsen, K. W. *Mol. Pharmaceutics* **2013**, *10*, 905-917.
115. Kipke, S.; Schmid, G. *Adv. Funct. Mater.* **2004**, *14*, 1184-1188.
116. Yin, J.; Xu, Q.; Wang, Z.; Yao, X.; Wang, Y. *J. Mater. Chem. C* **2013**, *1*, 1029-1036.
117. Lassiaz, S.; Galarneau, A.; Trens, P.; Labarre, D.; Mutin, H.; Brunel, D. *New. J. Chem.* **2010**, *34*, 1424-1435.

10 List of Figures and Tables

FIGURE 1.1:	THE CRYSTALLIZATION PATHWAY.	1
FIGURE 1.2:	CHART SHOWING NUCLEATION STEPS.	2
FIGURE 1.3:	SCHEMATIC REPRESENTATION OF THE CRYSTAL GROWTH VIA KINK SITES.	6
FIGURE 2.1:	SUMMARY OF RELATIONSHIP BETWEEN INTERPORE DISTANCE D_{INT} , VOLTAGE AND ELECTROLYTE. REPRODUCED FROM REF 59.	14
FIGURE 2.2:	SEM IMAGES OF THE TWO NANOPOROUS MATRICES; (A) ANODIC ALUMINUM OXIDE (AAO), (B) CONTROLLED POROUS GLASSES (CPG).	16
FIGURE 2.3:	STRUCTURE OF ACETAMINOPHEN $C_8H_9NO_2$	17
FIGURE 2.4:	UNIT CELL OF MONOCLINIC ACETAMINOPHEN FORM I, VISUALIZED WITH MERCURY 3.1 BASED ON CSD DEPOSITION NUMBER HXACAN04 ⁶² . OXYGEN ATOMS ARE RED, NITROGEN ATOMS ARE BLUE, CARBON ATOMS ARE GRAY, AND HYDROGEN ATOMS ARE NOT SHOWN.	17
FIGURE 2.5:	UNIT CELL OF ORTHORHOMBIC ACETAMINOPHEN FORM II, VISUALIZED WITH MERCURY 3.1 BASED ON CSD DEPOSITION NUMBER HXACAN23 ⁶³ . OXYGEN ATOMS ARE RED, NITROGEN ATOMS ARE BLUE, CARBON ATOMS ARE GRAY, AND HYDROGEN ATOMS ARE NOT SHOWN.	18
FIGURE 2.6:	STRUCTURE OF <i>N</i> -TETRACOSANE ($C_{24}H_{50}$) WITH C–C BOND LENGTH AND BOND ANGLE. ...	19
FIGURE 2.7:	PHASE TRANSITIONS TEMPERATURES OF <i>N</i> -TETRACOSANE: TRICLINIC TO ROTATOR PHASE ($TRICLINIC \rightarrow R_V$), ROTATOR TO ROTATOR PHASE ($R_V \rightarrow R_I$, $R_I \rightarrow R_{II}$), AND ROTATOR TO LIQUID PHASE ($R_{II} \rightarrow MELT$). REPRODUCED FROM REF 69.	20
FIGURE 2.8:	SCHEMATIC VIEW OF THE LAMELLAR ARRANGEMENT. THE MOLECULE LONG CHAINS ARE ORIENTED NORMAL TO THE LAYERS WHICH HAVE AN AB LAYER STACKING SEQUENCE.	20
FIGURE 2.9:	UNIT CELL OF TRICLINIC <i>N</i> -TETRACOSANE, VISUALIZED WITH MERCURY 3.1 BASED ON CSD DEPOSITION NUMBER ZZOFC04 ⁷² . CARBON ATOMS ARE GRAY AND HYDROGEN ATOMS ARE NOT SHOWN.	21
TABLE 2.1:	ANODIZATION AND WIDENED PARAMETERS FOR AAO 20/25, 35 AND 60 NM.	15
TABLE 2.2:	ANODIZATION AND WIDENED PARAMETERS FOR AAO 100, 180 AND 400 NM.	15
TABLE 2.3:	TEXTURAL PROPERTIES OF CPG MEMBRANES.	16
TABLE 2.4:	UNIT CELL PARAMETER OF <i>N</i> -TETRACOSANE.	21
FIGURE 3.1:	SEM IMAGE OF AAO 60 NM ODP-A-MODIFIED.	22
FIGURE 3.2:	TEMPERATURE CONTROLLED FURNACES (1) WITH COOLING SYSTEM (2) AND ARGON OR VACUUM SUPPLY (3), INFILTRATION OF THE AAO MEMBRANES INSIDE THE FURNACE (4).	23
FIGURE 3.3:	ETCHING OF THE ALUMINUM SUBSTRATE WITH STIRRER (1) AND SAMPLE HOLDER IN AN ICE BATH (2).	24
FIGURE 3.4:	TEMPERATURE PROGRAM OF THE COOLING RATES; (A) THE INFILTRATED ACETAMINOPHEN WAS COOLED (A) IN THE PRESENCE OR (B) IN THE ABSENCE OF A BULK SURFACE RESERVOIR. SF STANDS FOR BULK SURFACE MATERIAL.	25
FIGURE 3.5:	BRAGG REFLECTIONS FROM PARTICULAR FAMILY OF LATTICE PLANES WHERE INCIDENT BEAM AND DIFFRACTED BEAM ENCLOSE AN ANGLE OF θ	28

FIGURE 3.6:	THE EWALD SPHERE IN RECIPROCAL SPACE WITH DIFFRACTION VECTOR CONE AND ONE DEBYE RING BELONGING TO A FIXED θ ANGLE.	31
FIGURE 3.7:	X-RAY DIFFRACTION GEOMETRY IN REAL SPACE AND TRANSFER INTO THE RECIPROCAL SPACE.	32
FIGURE 3.8:	PANALYTICAL X'PERT PRO MRD WITH INCIDENT BEAM OPTICS (1), ANTON PAAR HOT-STAGE DHS 1100 (2) AND DIFFRACTED BEAM OPTICS (3).	33
FIGURE 3.9:	GEOMETRY USED FOR X-RAY DIFFRACTION STUDIES IN REAL SPACE. THE SAMPLE IS PLACED IN SUCH A WAY THAT THE SURFACE IS ORIENTED NORMAL TO THE PLANE CORRESPONDING TO THE INCIDENT X-RAY BEAM AND THE DIFFRACTED BEAM. THE DOTTED LINE IS THE TILT AXIS (θ AXIS) IN $\theta/2\theta$ SCANS. FOR SCHULZ SCANS THE SAMPLE IS ROTATED AROUND THE ψ AXIS (SOLID LINE). ON THE RIGHT, A DEBYE RING BELONGING TO A FIXED θ ANGLE IS INDICATED. REPRODUCED FROM REF 87.	33
FIGURE 3.10:	SCHULZ SCAN OF A TEXTURED SAMPLE IN THE RECIPROCAL SPACE; DEBYE RINGS WITH ANISOTROPIC DENSITY DISTRIBUTIONS. FOR SCHULZ SCANS THE SAMPLE IS ROTATED AROUND THE ψ AXIS WHICH IS ORIENTED NORMAL TO THE EQUATOR AND MERIDIAN. THETA AND 2θ ANGLES ARE FIXED.	34
FIGURE 3.11:	POWER COMPENSATED DSC 8500 PERKIN ELMER (1) WITH COOLING DEVICE (2) AND UNIVERSAL CRIMPER PRESS (3).	37
FIGURE 3.12:	DSC HEATING CURVE (10 K/MIN) OF BULK ACETAMINOPHEN FORM II.	38
TABLE 3.1:	ACETAMINOPHEN SOLIDIFIED IN AAO AND CPG MEMBRANES, INFILTRATION PARAMETER, COOLING RATES, CONNECTION TO A BULK SURFACE FILM AND CHAPTER NUMBER.	26
TABLE 3.2:	<i>N</i> -TETRACOSANE SOLIDIFIED IN AAO AND CPG MEMBRANES, INFILTRATION PARAMETER, COOLING RATES, CONNECTION TO A BULK SURFACE FILM AND SAMPLES NAMES.	27
FIGURE 4.1:	THERMO GRAVIMETRIC ANALYSIS OF AAO 25 NM, ALUMINUM SUBSTRATE IS REMOVED; (A) ANNEALED AT 400 °C FOR 2 H UNDER VACUUM, (B) ANNEALED AT 400°C FOR 2 H UNDER VACUUM AND WATER STORAGE FOR 1 H, (C) ANNEALED AT 180 °C FOR 2 H UNDER VACUUM, (D) ANNEALED AT 180 °C FOR 2 H UNDER VACUUM AND WATER STORAGE FOR 1 H.	41
FIGURE 4.2:	PEAK-TO-PEAK AMPLITUDES OF EPR LINE AT ~ 3450G (CORRECTED FOR SAMPLE MASSES, AMPLITUDE/MG, ERROR \pm 2.5%); (A) AAO MEMBRANES PORE SIZES RANGING FROM 20–180 NM, REMOVAL OF THE AAO ALUMINUM SUBSTRATE, (B) SHOWED A ZOOMED RANGE.	44
FIGURE 4.3:	EPR SPECTRA OF 35 NM AAO SURFACE-MODIFIED WITH ODPa (SAMPLE 12).	45
TABLE 4.1:	AAO MEMBRANES FOR EPR MEASUREMENTS	43
FIGURE 5.1:	ACETAMINOPHEN IN 60 NM AAO PREPARED AT WETTING TEMPERATURE OF 175 °C FOR 30 MIN, QUENCHED IN THE PRESENCE OF A BULK SURFACE FILM AND REMOVAL OF THE BULK SURFACE RESERVOIR. (A) $\theta/2\theta$ SCAN, (B) SCHULZ SCAN, (C) FIRST DSC HEATING SCAN (10 K/MIN). THE DOTTED RED LINE CORRESPONDS TO THE BULK MELTING POINT OF ACETAMINOPHEN FORM I.	48
FIGURE 5.2:	ACETAMINOPHEN IN 60 NM AAO PREPARED AT WETTING TEMPERATURE OF 175 °C FOR 30 MIN, COOLED AT -0.5 K/MIN IN THE PRESENCE OF A BULK SURFACE FILM; (A) $\theta/2\theta$ SCAN TAKEN IN THE PRESENCE OF A BULK SURFACE FILM DIRECTLY AFTER NON-ISOTHERMAL CRYSTALLIZATION, (B) $\theta/2\theta$ SCAN AFTER REMOVAL OF THE BULK SURFACE FILM (C) SCHULZ SCAN, (D) FIRST DSC HEATING	

SCAN (10 K/MIN). THE DOTTED LINE CORRESPONDS TO THE BULK MELTING POINT OF ACETAMINOPHEN FORM II.	50
FIGURE 5.3: ACETAMINOPHEN IN 60 NM AAO COOLED AT A RATE OF -0.5 K/MIN IN THE PRESENCE OF A BULK SURFACE FILM (SF). (A) $\theta/2\theta$ SCAN TAKEN IN THE PRESENCE OF A BULK SURFACE FILM DIRECTLY AFTER NON-ISOTHERMAL CRYSTALLIZATION, (B) $\theta/2\theta$ SCANS AFTER REMOVAL OF THE BULK SURFACE FILM, (C) $\theta/2\theta$ SCAN AFTER REMOVAL OF THE BULK SURFACE FILM AND ANNEALING AT 135°C FOR 2 H.	52
FIGURE 5.4: ACETAMINOPHEN IN 60 NM AAO PREPARED AT WETTING TEMPERATURE OF 175°C FOR 30 MIN, QUENCHED WITHOUT CONTACT TO BULK SURFACE RESERVOIR (A) $\theta/2\theta$ SCAN, (B) FIRST DSC HEATING SCAN (10 K/MIN). (C) $\theta/2\theta$ SCAN AND (D) SCHULZ SCAN OF THE SAMPLE STORED 9 MONTH UNDER AMBIENT CONDITIONS.	54
FIGURE 5.5: $\theta/2\theta$ TEMPERATURE-DEPENDENT SCANS OF AMORPHOUS ACETAMINOPHEN IN 60 NM AAO, MOUNTED IN THE XRD DEVICE.	55
FIGURE 5.6: ACETAMINOPHEN IN 60 NM AAO COLD CRYSTALLIZED AT 90°C FOR 4 DAYS IN THE ABSENCE OF A BULK SURFACE RESERVOIR. NOTE THE Y-AXIS IS LOGARITHMIC.	56
FIGURE 5.7: ACETAMINOPHEN IN 60 NM AAO COLD CRYSTALLIZED AT 80°C FOR 2 H IN THE PRESENCE OF A BULK SURFACE FILM, REMOVAL OF THE BULK SURFACE MATERIAL, AND ANNEALING AT 135°C FOR 2 H; (A) $\theta/2\theta$ SCAN, (B) SCHULZ SCAN, (C) FIRST DSC HEATING SCAN (10 K/MIN).	57
FIGURE 5.8: ACETAMINOPHEN IN 60 NM CPG PREPARED AT WETTING TEMPERATURE OF 180°C FOR 2 MIN; (A) QUENCHED IN THE PRESENCE OF A BULK SURFACE FILM, REMOVAL OF THE LATTER, (B) QUENCHED IN THE ABSENCE OF A BULK SURFACE FILM, (C) DSC FIRST HEATING SCAN (10 K/MIN) OF SAMPLE A, (D) DSC FIRST HEATING SCAN (10 K/MIN) OF SAMPLE B. NOTE THE BROAD HALO ORIGINATED BY THE POROUS GLASS MATRIX IS SUBTRACTED.	58
FIGURE 5.9: $\theta/2\theta$ SCANS OF ACETAMINOPHEN IN 60 NM CPG PREPARED AT WETTING TEMPERATURE OF 180°C FOR 2 MIN; (A) AND (B) COOLED AT -0.5 K/MIN IN THE PRESENCE OF A BULK SURFACE FILM, (C) AND (D) COOLED AT -0.5 K/MIN IN THE ABSENCE OF A BULK SURFACE FILM.	59
FIGURE 5.10: $\theta/2\theta$ SCANS OF ACETAMINOPHEN FORM II IN AAO 25–400 NM PREPARED AT WETTING TEMPERATURE OF 175°C FOR 30 MIN, COOLED AT -0.5 K/MIN IN THE PRESENCE OF A BULK SURFACE FILM. BEFORE WAXS MEASUREMENTS THE BULK SURFACE FILM WAS REMOVED.	60
FIGURE 5.11: $\theta/2\theta$ SCANS OF ACETAMINOPHEN FORM III IN AAO 25–400 NM PREPARED AT WETTING TEMPERATURE 175°C FOR 30 MIN, COOLED AT -0.5 K/MIN IN THE PRESENCE OF A BULK SURFACE FILM. BEFORE WAXS MEASUREMENTS THE BULK SURFACE FILM IS REMOVED.	61
FIGURE 5.12: SCHULZ SCANS OF ACETAMINOPHEN FORM III IN AAO 100 NM, 60 NM, AND 25 NM PREPARED AT WETTING TEMPERATURE OF 175°C FOR 30 MIN, COOLED AT -0.5 K/MIN IN THE PRESENCE OF A BULK SURFACE RESERVOIR.	62
FIGURE 5.13: SCHULZ SCANS OF ACETAMINOPHEN FORM III IN 400 NM AAO PREPARED AT WETTING TEMPERATURE OF 175°C FOR 30 MIN, COOLED AT -0.5 K/MIN IN THE PRESENCE OF A BULK SURFACE RESERVOIR.	63
FIGURE 5.14: ACETAMINOPHEN IN 25 NM AAO PREPARED AT WETTING TEMPERATURE OF 175°C FOR 30 MIN, COOLED AT -0.5 K/MIN IN THE PRESENCE OF A BULK SURFACE RESERVOIR, REMOVAL OF THE LATTER. (A) $\theta/2\theta$ SCANS OF FORM II AND III, (B) SCHULZ SCANS OF FORM II, (C) SCHULZ SCANS OF FORM III.	64
FIGURE 5.15: CASE A: $\theta/2\theta$ SCANS OF ACETAMINOPHEN IN AAO 25–400 NM COLD CRYSTALLIZED AT 80°C FOR 2 H IN THE PRESENCE OF A BULK SURFACE RESERVOIR, MEASURED AFTER REMOVAL OF THE BULK SURFACE MATERIAL.	65
FIGURE 5.16: SCHULZ SCANS OF ACETAMINOPHEN IN AAO MEMBRANES COLD CRYSTALLIZED AT 80°C FOR 2 H IN THE PRESENCE OF A BULK SURFACE RESERVOIR, MEASURED AFTER REMOVAL OF THE BULK SURFACE MATERIAL.	66
FIGURE 5.17: ACETAMINOPHEN IN AAO COLD CRYSTALLIZED AT 80°C FOR 2 H IN THE PRESENCE (CASE A) OR IN THE ABSENCE (CASE B) OF A BULK SURFACE RESERVOIR.	68

FIGURE 5.18:	ACETAMINOPHEN IN 60 NM AAO.	68
FIGURE 5.19:	ACETAMINOPHEN FORM II (0k0) LATTICE PLANES ORIENTED NORMAL TO THE AAO PORE AXIS, VISUALIZED WITH MERCURY 3.1. OXYGEN ATOMS ARE RED, NITROGEN ATOMS ARE BLUE, CARBON ATOMS ARE GREY, HYDROGEN ATOMS ARE NOT SHOWN.	69
FIGURE 5.20:	SCHEMATIC VIEW OF ACETAMINOPHEN FORM III/FORM II FAST-GROWTH DIRECTION ALIGNED WITH THE AAO PORE AXIS.	71
FIGURE 5.21:	ACETAMINOPHEN IN 60 NM CPG.	75
FIGURE 5.22:	THE PORE MORPHOLOGY DIRECTS POLYMORPH FORMATION AND INFLUENCES THE KINETICS OF THE SOLID/SOLID TRANSITION OF ACETAMINOPHEN.	76
TABLE 5.1:	$\theta/2\theta$ PEAKS OF ACETAMINOPHEN FORM I WITH THE CORRESPONDING (<i>hkl</i>)-VALUES TAKEN FROM REF 61.	48
TABLE 5.2:	$\theta/2\theta$ PEAKS OF ACETAMINOPHEN FORM II WITH THE CORRESPONDING (<i>hkl</i>)-VALUES TAKEN FROM REF 63.	50
TABLE 5.3:	HERMANS' ORDER PARAMETER FOR ACETAMINOPHEN IN AAO MEMBRANES NON-ISOTHERMAL AND COLD CRYSTALLIZED.	67
TABLE 5.4:	ACETAMINOPHEN IN 25 AND 60 NM AAO COOLED AT -0.5 K/MIN IN THE PRESENCE OF A BULK SURFACE RESERVOIR.	74
TABLE 5.5:	ESTIMATED SINGLE PORE VOLUME, PORE AREA, AND SURFACE-TO-VOLUME RATIO OF CYLINDRICAL AAO PORES.	74
FIGURE 6.1:	SCHEMATIC VIEW OF DISSOLUTION TEST CONDITIONS.	78
FIGURE 6.2:	DISSOLUTION TESTING; (A) ACETAMINOPHEN FORM I, FORM II, AND AMORPHOUS FORM EMBEDDED IN AAO 60 NM. EACH DATA POINT REPRESENTS THE MEAN OF SIX DETERMINATIONS \pm STANDARD DEVIATIONS. (B) THE INSET SHOWED A ZOOMED TEMPERATURE RANGE.	79
FIGURE 6.3:	DISSOLUTION TESTING OF ACETAMINOPHEN FORM II (A) FROM AAO MEMBRANES 25–400 NM. EACH DATA POINT REPRESENTS THE MEAN OF TWO DETERMINATIONS, EXCEPT AAO 60 NM SIX DETERMINATIONS. (B) THE INSET SHOWED A ZOOMED TEMPERATURE RANGE.	81
FIGURE 6.4:	ACETAMINOPHEN FORM I, FORM II AND AMORPHOUS FORM CONFINED TO AAO. RELEASE DATA FITTED TO THE KORSMEYER-PEPPAS MODEL.	83
FIGURE 6.5:	SCHEMATIC VIEW OF SAMPLE PREPARATION AND DRUG RELEASE: (1) ACETAMINOPHEN FORM II (RED) IN AAO MEMBRANES (BLACK), (2) PLLA FILM SPIN-COATED ON THE INFILTRATED AAO MEMBRANE, (3) DEGRADATION OF THE PLLA FILM AND CONTROLLED DRUG RELEASE.	85
FIGURE 6.6:	SEM IMAGES OF; (A) PLLA POLYMER FILM ON THE AAO MEMBRANE, (B) CROSS-SECTION VIEW OF THE AAO MEMBRANE (BOTTOM) AND THE PLLA POLYMER FILM (TOP), (C) RESIDUES ON THE AAO MEMBRANE AFTER DISSOLUTION TEST (D) CROSS-SECTION VIEW OF THE AAO MEMBRANE (BOTTOM) AFTER DISSOLUTION TEST.	86
FIGURE 6.7:	DISSOLUTION TESTING OF ACETAMINOPHEN FORM II IN 60 NM AAO (A) UNCOATED AND COATED WITH PLLA POLYMER FILM. (B) THE INSET SHOWED A ZOOMED TEMPERATURE RANGE. EACH DATA POINT REPRESENTS THE MEAN OF FOUR(COATED)/SIX(UNCOATED) DETERMINATIONS \pm STANDARD DEVIATIONS.	87
FIGURE 6.8:	ACETAMINOPHEN FORM II IN 60 NM AAO. THE MOLECULE ARRANGEMENT IN THE ORTHORHOMBIC UNIT CELL IS VISUALIZED WITH MERCURY 3.1; (A) ORTHORHOMBIC (040) CRYSTAL FACE, (B) ORTHORHOMBIC (020) CRYSTAL FACE.	89
TABLE 6.1:	ACETAMINOPHEN IN 60 NM AAO, ACETAMINOPHEN MODIFICATIONS, AND MAIN LATTICE PLANES.	78

TABLE 6.2:	DRUG RELEASE AT SPECIFIC TIME INTERVALS.	78
TABLE 6.3:	TIME TAKEN FOR 50% OF ACETAMINOPHEN RELEASE FROM 60 NM AAO.	80
TABLE 6.4:	ACETAMINOPHEN FORM II/III IN AAO WITH PORE SIZES RANGING FROM 25 NM TO 400 NM.	81
TABLE 6.5:	DIFFUSIONAL EXPONENT n AND REGRESSION COEFFICIENT R^2 FOR DRUG RELEASE OF ACETAMINOPHEN MODIFICATIONS FROM 60 NM AAO.	84
TABLE 6.6:	RELEASE LAW/MODEL AND REGRESSION COEFFICIENT R^2 FOR THE DRUG RELEASE OF ACETAMINOPHEN FROM 60 NM AAO COATED WITH PLLA.	88
FIGURE 7.1:	PROGRAMMED TEMPERATURE PROFILE FOR WAXS AND SCHULZ (ψ) SCANS.	93
FIGURE 7.2:	$\theta/2\theta$ TEMPERATURE-DEPENDENT SCANS OF BULK <i>N</i> -TETRACOSANE, MOLTEN AT 80 °C ON A SILICON-WAFER, COOLED UNDER AMBIENT CONDITIONS; A) HEATING, B) COOLING.	93
FIGURE 7.3:	d -VALUES OF THE (002) LAYER PEAKS FOR BULK <i>N</i> -TETRACOSANE. (A) HEATING (BLACK LINE), COOLING (RED LINE), (B) SCHEMATIC VIEW OF THE LAYERED STRUCTURES WITH VALUES OF THE LAYER THICKNESS IN THE TRICLINIC AND R_{II} ROTATOR PHASE.	94
FIGURE 7.4:	SECOND DSC SCANS (10 K/MIN) FOR BULK <i>N</i> -TETRACOSANE; HEATING (BLACK LINE), COOLING (BLUE LINE).	95
FIGURE 7.5:	SUMMARY OF PHASE TRANSITIONS DURING HEATING AND COOLING OF BULK <i>N</i> -TETRACOSANE.	96
FIGURE 7.6:	$\theta/2\theta$ TEMPERATURE-DEPENDENT HEATING SCANS OF <i>N</i> -TETRACOSANE IN AAO COOLED AT -0.5 K/MIN IN THE PRESENCE OF A BULK SURFACE FILM, REMOVAL OF THE BULK SURFACE FILM; A) AAO 60 NM, B) AAO 25 NM, C) AAO 60 NM ODPA-MODIFIED. THE SECOND AND THE THIRD ROWS SHOW ZOOMED FIGURES.	97
FIGURE 7.7:	$\theta/2\theta$ TEMPERATURE-DEPENDENT COOLING SCANS OF <i>N</i> -TETRACOSANE IN AAO COOLED AT -0.5 K/MIN IN THE PRESENCE OF A BULK SURFACE FILM, REMOVAL OF THE BULK SURFACE FILM; A) AAO 60 NM, B) AAO 25 NM, C) AAO 60 NM ODPA-MODIFIED. THE SECOND ROW SHOWS ZOOMED FIGURES.	98
FIGURE 7.8:	TEMPERATURE-DEPENDENT INTEGRATED AREA AS FUNCTION OF THE REFLECTIONS (A) AT $2\theta = 23.3^\circ$, (B) AT $2\theta = 36.0^\circ$ FOR 60 NM AAO (CORRESPONDING TO CASE A IN FIGURE 7.6). PHASE TRANSITIONS ARE INDICATED BY DOTTED LINES.	99
FIGURE 7.9:	TEXTURE ANALYSIS OF <i>N</i> -TETRACOSANE IN 60 NM AAO (CORRESPONDING TO CASE A IN FIGURE 7.6) PREPARED BY CRYSTALLIZATION WITH BULK SURFACE FILM MEASURED AT THE FIXED ANGLE OF 36.0° , (A) ψ SCANS, (B) HERMANS' ORDER PARAMETER F^{91}	100
FIGURE 7.10:	TEXTURE ANALYSIS OF <i>N</i> -TETRACOSANE IN 60 NM AAO (CASE A IN FIGURE 7.6) PREPARED BY CRYSTALLIZATION WITH BULK SURFACE FILM MEASURED AT THE FIXED ANGLE, (A) OF 21.4° ψ SCANS, (B) 21.4° TEMPERATURE-DEPENDENT AREA OF THE ψ SCANS, (C) OF 23.4° ψ SCANS, (D) 23.4° TEMPERATURE-DEPENDENT AREA OF THE ψ SCANS. THE THEORETICAL ANGLE BETWEEN (-111) AND (013) LATTICE PLANES IS INDICATED WITH A DOTTED LINE.	101
FIGURE 7.11:	<i>N</i> -TETRACOSANE IN 25 NM AAO COOLED AT -0.5 K/MIN IN THE PRESENCE OF A BULK SURFACE RESERVOIR, REMOVAL OF THE BULK SURFACE FILM; (A) $\theta/2\theta$ TEMPERATURE-DEPENDENT HEATING SCANS, PHASE TRANSITIONS ARE ORDERED FOR INCREASING TEMPERATURES. (B) TEMPERATURE-DEPENDENT SCHULZ SCANS, $2\theta = 5.84^\circ$ CORRESPONDS TO THE (002) TRICLINIC LATTICE PLANES, $2\theta = 5.4^\circ$ CORRESPONDS TO THE (002) ORTHORHOMBIC LATTICE PLANES.	102
FIGURE 7.12:	<i>N</i> -TETRACOSANE CONFINED TO AAO MEMBRANES; (A) d -VALUES OF (002) LAYER PEAKS FOR —■— BULK <i>N</i> -TETRACOSANE, —■— AAO 60 NM, —●— AAO 25 NM, —▲— AAO 60 NM ODPA-MODIFIED. (B) SCHEMATIC VIEW OF THE LAYERED STRUCTURES FOR BULK MATERIAL AND <i>N</i> -TETRACOSANE IN AAO MEMBRANES WHERE LAMELLAR LAYERS ARE ORIENTED NORMAL TO THE AAO PORE AXIS.	103

FIGURE 7.13:	$\theta/2\theta$ TEMPERATURE-DEPENDENT HEATING SCANS OF <i>N</i> -TETRACOSANE IN AAO COOLED AT -0.5 K/MIN IN THE ABSENCE OF A BULK SURFACE FILM; D) AAO 60 NM, E) AAO 25 NM, F) AAO 60 NM ODPa-MODIFIED. THE SECOND ROW SHOWS ZOOMED FIGURES.	106
FIGURE 7.14:	$\theta/2\theta$ TEMPERATURE-DEPENDENT COOLING SCANS OF <i>N</i> -TETRACOSANE IN AAO COOLED AT -0.5 K/MIN IN THE ABSENCE OF A BULK SURFACE FILM; D) AAO 60 NM, E) AAO 25 NM, F) AAO 60 NM ODPa-MODIFIED. THE SECOND ROW SHOWS ZOOMED FIGURES.	107
FIGURE 7.15:	TEXTURE ANALYSIS OF <i>N</i> -TETRACOSANE IN 60 NM AAO (CASE D IN FIGURE 7.13) COOLED AT -0.5 K/MIN IN THE ABSENCE OF A BULK SURFACE RESERVOIR; (A) MEASURED AT THE FIXED ANGLE OF 36.0° ψ SCANS, (B) HERMANS' ORDER PARAMETER F^{91} , (C) MEASURED AT THE FIXED ANGLE 19.3° ψ SCANS, (D) TEMPERATURE-DEPENDENT AREA OF THE ψ SCANS.	108
FIGURE 7.16:	$\theta/2\theta$ TEMPERATURE-DEPENDENT HEATING SCANS OF <i>N</i> -TETRACOSANE IN; G) CPG 60 NM, H) CPG 25 NM, I) CPG 2 NM AND COOLED AT -0.5 K/MIN IN THE PRESENCE OF A BULK SURFACE RESERVOIR. J) CPG 60 NM, K) CPG 25 NM, L) CPG 2 NM AND COOLED AT -0.5 K/MIN IN THE ABSENCE OF A BULK SURFACE RESERVOIR. NOTE THE AMORPHOUS HALO THAT CAN BE SEEN AROUND $2\theta = 22^\circ$ IS ORIGINATING FROM THE CPG MATRIX. <i>N</i> -TETRACOSANE IN 2 NM CPG REVEALED NO REFLECTIONS.	110
FIGURE 7.17:	$\theta/2\theta$ TEMPERATURE-DEPENDENT COOLING SCANS OF <i>N</i> -TETRACOSANE IN; G) CPG 60 NM, H) CPG 25 NM, I) CPG 2 NM AND COOLED AT -0.5 K/MIN IN THE PRESENCE OF A BULK SURFACE RESERVOIR. J) CPG 60 NM, K) CPG 25 NM, L) CPG 2 NM AND COOLED AT -0.5 K/MIN IN THE ABSENCE OF A BULK SURFACE RESERVOIR.	111
FIGURE 7.18:	<i>N</i> -TETRACOSANE IN 25 NM CPG CORRESPONDING TO SAMPLE H COOLED AT -0.5 K/MIN IN THE PRESENCE OF A BULK SURFACE RESERVOIR; (A) $\theta/2\theta$ SCANS, (B) <i>D</i> -VALUES AND SCHEMATIC VIEW OF THE LAMELLAR LAYERS.	112
FIGURE 7.19:	FIRST DSC SCANS (10 K/MIN) OF <i>N</i> -TETRACOSANE IN; (A) AAO 60 NM, (B) AAO 25 NM, (C) AAO 60 NM ODPa-MODIFIED AND CRYSTALLIZED AT A COOLING RATE OF -0.5 K/MIN IN THE PRESENCE OF A BULK SURFACE RESERVOIR, (D) AAO 60 NM, (E) AAO 25 NM, (F) AAO 60 NM ODPa-MODIFIED AND CRYSTALLIZED AT A COOLING RATE OF -0.5 K/MIN IN THE ABSENCE OF A BULK SURFACE RESERVOIR. HEATING SCAN (BLACK LINE), COOLING SCAN (BLUE LINE).	113
FIGURE 7.20:	FIRST DSC SCANS (10 K/MIN) OF <i>N</i> -TETRACOSANE IN; (A) CPG 25 NM, (B) CPG 2 NM AND NON-ISOTHERMALLY CRYSTALLIZED AT A COOLING RATE OF -0.5 K/MIN IN THE PRESENCE OF A BULK SURFACE RESERVOIR, (C) CPG 25 NM, (D) CPG 2 NM AND NON-ISOTHERMALLY CRYSTALLIZED AT A COOLING RATE OF -0.5 K/MIN IN THE ABSENCE OF A BULK SURFACE RESERVOIR. HEATING SCAN (BLACK LINE), COOLING SCAN (BLUE LINE).	115
FIGURE 7.21:	LONG-TIME STORAGE OF <i>N</i> -TETRACOSANE IN 60 NM AAO MEMBRANES COOLED AT -0.5 K/MIN; A) IN THE PRESENCE OF A BULK SURFACE RESERVOIR, B) IN THE ABSENCE OF A BULK SURFACE RESERVOIR. NOTE FOR BETTER VISUALIZATION THE <i>y</i> AXIS IS LOGARITHMIC.	116
FIGURE 7.22:	THE TRICLINIC UNIT CELL OF <i>N</i> -TETRACOSANE IN AAO MEMBRANES. THE (-111) LATTICE PLANES ARE ORIENTED NORMAL TO THE PORE AXIS, THE (002) LATTICE PLANES ARE ORIENTED PARALLEL TO THE AAO PORE AXIS. THE UNIT CELL IS VISUALIZED WITH MERCURY 3.1 BASED ON CSD ZZZOF04 ⁷² . CARBON ATOMS ARE GREY AND HYDROGEN ATOMS ARE NOT SHOWN.	118
FIGURE 7.23:	<i>N</i> -TETRACOSANE IN AAO COOLED AT -0.5 K/MIN IN THE PRESENCE OF A BULK SURFACE RESERVOIR. MEASURED AREAS OF THE PEAKS AT $2\theta = 36.0^\circ$ (RED DOTTED LINE) AND $2\theta = 23.3^\circ$ (BLACK SOLID LINE) AS FUNCTIONS OF THE TEMPERATURE <i>T</i> . A) AAO 60 NM, B) AAO 25 NM, C) AAO 60 NM ODPa-MODIFIED.	120
FIGURE 7.24:	<i>N</i> -TETRACOSANE IN AAO COOLED AT -0.5 K/MIN IN THE ABSENCE OF A BULK SURFACE RESERVOIR. MEASURED AREAS OF THE PEAKS AT $2\theta = 36.0^\circ$ (RED DOTTED LINE) AND $2\theta = 21.4^\circ$ (BLACK SOLID LINE) AS FUNCTIONS OF THE TEMPERATURE <i>T</i> . A) AAO 60 NM, B) AAO 25 NM, C) AAO 60 NM ODPa-MODIFIED. THE SECOND ROW SHOWS A ZOOMED FIGURE.	121
FIGURE 7.25:	CALCULATED HERMANS' ORDER PARAMETERS <i>F</i> FOR THE $2\theta = 36.0^\circ$ REFLECTION OF <i>N</i> -TETRACOSANE IN AAO COOLED AT -0.5 K/MIN; (A) IN THE PRESENCE OF A BULK SURFACE	

RESERVOIR, (B) IN THE ABSENCE OF A BULK SURFACE RESERVOIR. —□— AAO 60 NM, —○— AAO 25 NM; —▲— AAO 60 NM ODPa-MODIFIED.....	122
FIGURE 7.26: SCHEMATIC VIEW OF THE TWO REGIME MODEL OF <i>N</i> -TETRACOSANE IN AAO CRYSTALLIZED IN THE PRESENCE OF A BULK SURFACE RESERVOIR. (A) LAMELLAE (BLACK BARS) ARE ORIENTED NORMAL TO THE AAO PORE AXIS CLOSE TO AAO PORE WALLS AND ARE ORIENTED PARALLEL TO THE PORE AXIS FAR FROM AAO PORE WALLS. (B) LAMELLAE (BLACK BARS) ARE ORIENTED NORMAL TO THE AAO PORE AXIS CLOSE TO AAO PORE WALLS AND NO LAYERED STRUCTURES IN THE AAO PORES.....	124
FIGURE 7.27: A SCHEMATIC VIEW OF LAMELLAR LAYERS IN 25 NM AAO WHERE AT 25 °C LAMELLAR LAYERS NEARLY ORIENTED PARALLEL TO THE AAO PORE AXIS AND AT 44 °C LAMELLAR LAYERS ORIENTED NORMAL TO THE AAO PORE AXIS.....	125
FIGURE 7.28: SUMMARY OF PHASE TRANSITIONS OF <i>N</i> -TETRACOSANE IN 60 NM AAO CRYSTALLIZED IN THE PRESENCE OF A BULK SURFACE RESERVOIR. NOTE THE X-RAY MEASUREMENTS ENDS UP TO 46°C.....	127
TABLE 7.1: PHASE TRANSITION TEMPERATURES OF <i>N</i> -TETRACOSANE IN AAO MEMBRANES MEASURED WITH FIRST DSC HEATING SCANS.....	126
FIGURE 8.1: SCHEMATIC VIEW OF MESOSCOPIC CRYSTAL ENGINEERING.....	133

11 Abbreviations and Symbols

11.1 Abbreviations

a, b, c	Unit cell parameters, Lengths
a^*, b^*, c^*	Reciprocal lattice vector
A, a	Surface area, pre-Exponential factor, Concentration
AAO	Anodic Aluminum Oxide
ACE	Acetaminophen
APAs	Alkylphosphonic acids
A_o, A_t	Infiltrated material at $t = 0$, Released material at time t
B_0	Magnetic field
C	Center of the Ewald sphere
CC	Cold Crystallization
Ch.	Chapter
C_m	Molar heat capacity
C_p/C_v	Heat capacity at constant pressure/at constant volume
CPG	Controlled Porous Glasses
CSD	Cambridge Structural Database
d	Thickness
d_{hkl}	d -Spacing
D_p, d	Pore diameter/size, Distance

DSC	Differential Scanning Calorimetry	
E	Attachment energy	
e.g.,	For example	Lat.: <i>exempli grata</i>
etc.	More of the same type	Lat.: <i>etcetera</i>
et al.	And others	Lat.: <i>et alii</i>
EPR	Electron Paramagnetic Resonance	
f	Hermans' order parameter	
FWHM	Full Width at Half Maximum	
G	Gibbs free energy	
g_e	g-Value of a radical	
H	Enthalpy	
h	Plank constant	
H_{HKL}	Reciprocal lattice vector	
I	Intensity	
i.e.,	That is	Lat.: <i>id est</i>
in vivo	'within the living'	
in vitro	'in glass'	
K	Crystallite shape factor	
k, k_B	Constant, Boltzmann's constant	
M_n	Number Average Molecular Weight	
M_w	Weight Average Molecular Weight	
n	Integer number, Diffusional exponent	

O	Origin of the reciprocal lattice
ODPA	Octadecylphosphonic acid
P	Electrical power, Pressure, Reciprocal point
PBS	Phosphate buffered saline (137 mM NaCl, 2.7 mM KCl, 10 mM Na ₂ HPO ₄ , 2 mM KH ₂ PO ₄ , pH 7.4–7.6)
PLLA	Poly(L)-Lactide
Q	Heat transfer
R	Rotator phases, Molar gas constant
r, r*	Radius, Critical radius
S	Entropy, Spreading parameter, Scattering vector
s ₀ , s	Unit vectors
SEM	Scanning Electron Microscopy
T	Temperature
t	Time
TGA	Thermo Gravimetric Analysis
T _m	Melting temperature
T _p	Pore depth
U	Internal energy
V	Volume
WAXS	Wide Angle X-ray Scattering
XRD	X-ray Diffraction
2D	Two-Dimensional

(hkl) Notation for a single plane

$\{hkl\}$ Set of planes

11.2 Symbols

\AA Angstrom $1 \text{\AA} = 0.1 \text{ nm}$

α, β, γ Unit cell parameters, angles

γ Surface, Interfacial tension, Activity coefficient

θ Contact angle, Bragg/scattering angle

λ Wavelength

μ_B Bohr magneton

ρ Density

ψ Tilting angle

Acknowledgements / Danksagung

Die vorliegende Arbeit entstand von Dezember 2010 bis Oktober 2014 in der Arbeitsgruppe von Prof. Dr. Steinhart am Institut für Chemie neuer Materialien, Abteilung Physikalische Chemie, der Universität Osnabrück.

Bei Herrn Prof. Dr. Martin Steinhart möchte ich mich für die interessante Themenstellung, die gute Betreuung sowie für die Bereitstellung der Arbeitsmittel bedanken.

Mein besonderer Dank gilt Herrn Prof. Dr. Mario Beiner und Frau M. Sc. Nicole Sonnenberger von der Martin-Luther-Universität Halle-Wittenberg sowie Prof. Dr. Dirk Enke und Frau Dipl.-Chem. Nicole Anders von der Universität Leipzig. In vielen Projekttreffen zur *Kristallisation polymorpher Arzneimittel in Nanoporen* kam es zu interessanten Diskussionen, die das schwierige Thema immer ein Stück weiter voran gebracht haben. Herrn Prof. Dr. Mario Beiner danke ich für die Übernahme des Zweitgutachtens.

Ich möchte mich recht herzlich bei allen Mitarbeitern der Arbeitsgruppe Physikalische Chemie bedanken. Insbesondere bei Frau Brigitte Hartmann-Azanza für die Unterstützung bei den Röntgenmessungen sowie bei Frau Claudia Hess für die Aufnahme der REM-Bilder. Für die immer verfügbare benötigte Anzahl von AAO Membranen danke ich Herrn Heinrich Tobergte und Frau Claudia Hess. Ebenso danken möchte ich Frau Barbara Gunkel für die Bearbeitung der Reiseanträge und sonstiger organisatorischer ‚Probleme‘. Frau M. Sc. Wajiha Akram und Frau M. Sc. Anna Volf-Eichler möchte ich für die aufmunterten Bürogespräche danken.

Dank an Frau Kerstin Rücker im Arbeitskreis Anorganische Chemie für die TGA Messungen. Bei Herrn Dr. Johann Klare vom Fachbereich Physik möchte ich mich ebenfalls für die EPR Messungen bedanken.

Der größte Dank gebührt meiner Familie und Freunden. Ohne deren Unterstützung und steten Zuspruch wären mein Studium und diese Arbeit nicht zustande gekommen. Dabei

möchte ich besonders Frau Brit Kockisch hervorheben und mich für das geduldige Zuhören aber auch für das gemeinsame Lachen bedanken.

Herrn Dr. Dietrich Steinmeier und Frau Brigitte Hartmann-Azanza möchte ich herzlichst für das Gegenlesen danken.

Appendix A

AAO Samples for Measurements of Textural Properties

After AAO preparation the aluminum substrate was etched away and the pore bottoms were opened. The sample preparation details are given in Chapter 3.1. Approximately 1 g AAO materials of each AAO pore size were used for the nanopore characterization. The textural properties of AAO membranes were determined by the methods of nitrogen adsorption and mercury intrusion^d. Before measurements the AAO membranes were annealed at 150°C for 12 h.

Table 1: Textural properties of AAO membranes.

AAO Membrane [nm]	25	60
specific surface area ^e [m ² g ⁻¹]	11.4	13.6
specific pore volume [cm ³ g ⁻¹]	0.16	0.22
mean pore diameter (BJH) ^f [nm]	32.2	61.3

^d Universität Leipzig, Institut für Technische Chemie, AK Prof. Enke

^e BET method

^f Barrett-Joyner-Halenda method

Appendix B

Estimation of Acetaminophen in PBS Solution

The sample concentration was adjusted to compensate the dilutions. At each time interval 500 μ L PBS aliquot were withdrawn and 500 μ L fresh PBS was added to the drug release solution. The withdrawn PBS solution was pipetted in a microtube and stored two days at ambient temperature. The PBS aliquots were diluted e.g., 1:20, 25, 50 (v:v) depending on the released amount of acetaminophen at time t . Released acetaminophen was calculated via known standard solutions of 15.1, 7.6, 3.8, 1.9, and 0.95 mg/L acetaminophen in PBS, respectively. The measured UV-Vis absorptions were plotted against the standard concentrations. The data points were fitted to a simple linear regression. The samples concentrations were estimated with the expressed linear function. Details are listed in Table 2 and Table 3.

Table 2: Acetaminophen released from AAO membranes.

release time [min]		concentration [mg]	drug release [%]
	acetaminophen in AAO = $[A]_0$	x	
t_0		$x_0 = 0$	
$t_1 = 2$	concentration at begin	$x_1 = x_0$	
	measured concentration aliquot t_1	x_2	
	additive concentration	$x_1 - x_2 = x_3$	
	released at $t_1 = [A]_t$	$x_1 + x_3 = x_4$	$100 \cdot x_4 / x$
$t_2 = 4$	concentration at begin	$x_3 \cdot 5.5/6 = x_5$	
	measured concentration aliquot t_2	x_6	
	additive concentration	$x_6 - x_5 = x_7$	
	released at t_2	$x_7 + x_4 = x_8$	$100 \cdot x_8 / x$
$t_{21} = 2880$...		

Table 3: Example of the drug release of acetaminophen form I from 60 nm AAO membranes.

release time [min]		concentration [mg]	drug release [%]
acetaminophen form I in 60 nm AAO		3.01	
t_0		0	
$t_1 = 2$	concentration at begin	0	
	measured concentration aliquot t_1	0.65	
	additive concentration	0.65	
	released at t_1	0.65	21.5
$t_2 = 4$	concentration at begin	0.59	
	measured concentration aliquot t_2	1.01	
	additive concentration	0.42	
	released at t_2	1.07	35.4
$t_3 = 6$	concentration at begin	0.93	
	measured concentration aliquot t_3	1.24	
	additive concentration	0.31	
	released at t_3	1.38	45.7
until t_{21}			

Erklärung über die Eigenständigkeit der erbrachten wissenschaftlichen Leistung

Ich erkläre hiermit, dass ich die vorliegende Arbeit ohne unzulässige Hilfe Dritter und ohne Benutzung anderer als der angegebenen Hilfsmittel angefertigt habe. Die aus anderen Quellen direkt oder indirekt übernommenen Daten und Konzepte sind unter Angabe der Quelle gekennzeichnet.

Die Arbeit wurde bisher weder im In- noch im Ausland in gleicher oder ähnlicher Form einer anderen Prüfungsbehörde vorgelegt.

.....
(Ort, Datum) (Unterschrift)